Fall 12-17-2022

ENERGY DISSIPATION IN A SAND DAMPER UNDER CYCLIC LOADING

Ehab Sabi
esabi@smu.edu

ENERGY DISSIPATION IN A SAND DAMPER UNDER CYCLIC LOADING

Approved by:

Dr. Usama El Shamy

Professor

Dr. Nicos Makris

Professor

Dr. Yildirim Hurmuzlu

Professor

Dr.Edmond Richer

Associate Professor

Dr. Brett Story

Associate Professor

ENERGY DISSIPATION IN A SAND DAMPER UNDER CYCLIC LOADING

A Dissertation Presented to the Graduate Faculty of the

Bobby B.Lyle School of Engineering

Southern Methodist University

in

Partial Fulfillment of the Requirements

for the degree of

Doctor of Philosophy

with a

Major in Civil Engineering

by

Ehab Sabi

(B.S., Civil Engineering, Jazan University, KSA)
(M.S., Civil Engineering, Southern Methodist University, USA)

December 17, 2022

ACKNOWLEDGMENTS

This work could not have been accomplished without the help and constant support of my advisor, Dr. Usama El Shamy, who guided my efforts and provided me with a major source of knowledge and expertise in the field. Also, he helped me in choosing the right topic in research, which taught me about so many things which I am really thankful for. His energy and enthusiasm for research motivated me to work as hard as I could. It has been a great learning experience to pursue my PhD under his supervision.

I would like to thank Dr. Nicos Makris, Dr. Yildirim Hurmuzlu, Dr. Edmond Richer, and Dr. Brett Story for providing valuable feedback on my work. I would like to extend special thanks to the Civil and Environmental Engineering Department at SMU for giving me the opportunity to pursue a PhD degree and participate in research.

This research was partially supported the US Army Corps of Engineers Engineer Research and Development Center, grant number W9132V-13-C-0004 and the US National Science Foundation awards number CMMI-1728612 and CMMI-2036131 and the Saudi Arabia Cultural Mission (SACM) in the United States of America. These supports are gratefully acknowledged. Special thanks to my colleagues and friends for their friendship and encouragement. I owe my sincere gratitude to my parents and wife for their endless support and love.

Sabi, Ehab (B.S., Civil Engineering, Jazan University, KSA)
(M.S., Civil Engineering, Southern Methodist University, USA)

Energy Dissipation in a Sand Damper under Cyclic Loading

Advisor: Dr. Usama El Shamy

Doctor of Philosophy degree conferred December 17, 2022
Dissertation completed September 21, 2022

Various seismic and wind engineering designs and retrofit strategies have been in development to meet structures' proper and safe operation during earthquake and wind excitation. One such method is the addition of fluid and particle dampers, such as sand dampers, in an effort to reduce excessive and dangerous displacements of structures. The present study implements the discrete element method (DEM) to assess the performance of a pressurized sand damper (PSD) and characterize the dissipated energy under cyclic loading. The idea of a PSD is to exploit the increase in shearing resistance of sand under external pressure and the associated ability to dissipate energy through interparticle contact sliding. The dissipated energy in the pressurized sand during cyclic motion results in a reduction of excessive displacement. The advantage of using the DEM is that applying a simple linear contact model for the entire contacts assembly and also utilizing the advantage of irregular-shaped particles to mimic the behavior of actual sand grains.

The series of DEM simulations reported herein examine the effects of multiple factors on the magnitude of dissipated energy. These factors include stroke amplitude, grain size

distribution, the magnitude of pressure imposed on the sand, and different configurations of the PSD.

The results reveal that the main energy dissipation mechanism is generated through inter-particle frictional sliding in the sand. Additionally, the magnitude of cumulative dissipated energy increases with the pressure level applied to the sand damper, as well as with the stroke amplitude of the loading. Moreover, operating the piston with multiple spheres leads to a significant increase in the magnitude of dissipated energy. However, the soil exhibits similar behavior to the case of one sphere where a strain hardening behavior was noticed. A noticeable increase in the piston capacity was observed when the sphere size was increased by 10%, and the rest of the response patterns remained unchanged. According to the results, by increasing the sphere friction, the piston capacity remains almost the same. It is also worth mentioning that when a wider range of particle sizes was employed, the capacity of the maximum force considerably increased. A significant increase in the piston capacity was clearly noticed when a boxed-shaped piston configuration was utilized at the origin of the pressurized sand damper instead of a single sphere.

The results of the conducted simulations were quantitatively compared with experimental data obtained from physical modeling of a similar pressurized sand damper which revealed a fairly good agreement. This confirms the ability of the proposed framework to satisfactorily analyze complex geotechnical problems involving soil interaction and large deformations. The proposed sand damper model is shown to be a promising device that mitigates vibrations in structural systems subject to seismic and wind loading.

TABLE OF CONTENTS

LIST OF FIGURES

LIST OF TABLES

Chapter 1

INTRODUCTION

1.1. Objectives and Motivation

Earthquakes are regarded as one of the deadliest natural disasters. They lead to severe economic loss due to infrastructural damage and devastating loss of human life. Mitigation techniques include proper damping devices, which absorb the energy associated with shaking and play a large role in reducing the human and capital costs. Seismic events such as the 1994 Northridge earthquake, the 1995 Kobe earthquake, and the 2008 Sichuan earthquake draw into focus the significance of examining local geologic conditions for insight into the seismic ground response.

Using strong-motion records, these studies achieved major progress in improving structural design and analysis of different types of structures such as dames, bridges, buildings. These studies also yielded results identifying the damage due to seismic displacements. The results of these investigations were the impetus for the design and development of well-engineered structures to study energy dissipation mechanisms in soils and seismic retrofit of civil structures. Concurrently, inclusive retrofit programs, implemented globally, employ emerging response modification technologies (Buckle Ian and Ian, 1995; SEMINAR, 1997; FEMA, 2000; Agency, 2006).

Previous studies, focused on energy dissipation and damping characterizations of soils, developed models that estimate dynamic modulus degradation and damping curves (Hardin and Drnevich, 1972; Seed et al., 1986; Vucetic and Dobry, 1991). Seismic and wind engineering designs and retrofit strategies were developed to satisfy the mandated structural performance during a given seismic event or wind excitation. Along with seismic isolation (Kelly, 1986; Buckle and Mayes, 1990; Makris, 2019), studies found alternative strategies to traditional seismic capacity designs of structures. These include supplemental damping or strength/ductility-oriented designs, such as yielding steel dampers or buckling-restrained braces (Kelly et al., 1972; Skinner et al., 1974; Robinson and Greenbank, 1976; Soong and Dargush, 1997; Constantinou et al., 1998; Black et al., 2002, 2018, 2004; Symans et al., 2008). These devices have been designed specifically for energy dissipation, which has also been utilized to reduce building vibrations under wind loading (e.g (Davenport, 1967; Kareem and Gurley, 1996; McNamara et al., 1997; Kareem et al., 1999))

Many retrofitting methods and equipment can be installed in new or old buildings for comparatively low cost. This can make buildings much more "high performing" by considerably enhancing their structural integrity. The effect of earthquake ground motion transmitted to the buildings is reduced through passive energy dissipation. The base isolation is one form of passive energy dissipation systems. Figure 1.1 shows one location of the base isolated that could be installed in a structure to reduce seismic shaking. Base isolation's limitations are that it cannot be done on every structure. For example, it is not suitable for structures resting on soft soils. It becomes less efficient for high-rise buildings and cannot

be applied partially to the structure. Its Implementation is efficiently complicated and often requires highly skilled labor and engineers. Severe structural damage caused by earthquakes and wind motivated the exploration of pressurized sand dampers for earthquake and wind engineering systems (Makris et al., 2021). Other research explored a device designed to dissipate energy to reduce building vibrations (Davenport, 1967; Kareem and Gurley, 1996; McNamara et al., 1997; Kareem et al., 1999). Another type of device relies on fluid-dampers to limit excessive displacements (Makris et al., 2021). In a building, fluid-dampers can be incorporated within the skeleton of a structure (Miyamoto and Scholl, 1997), at the isolation level of a seismically isolated building (Asher et al., 1996; Constantinou et al., 1998), or in soft stories within a building to control drifts (Kelly and Konstantinidis, 2011; Youssef et al., 1995).

Some bridges are now fully equipped with large-capacity fluid-dampers (Makris et al., 2021), however, a challenge that arises with fluid-dampers is whether they can maintain their long-term integrity when placed in civil structures subjected to a variety of loads, appreciable dynamic displacements, or long-term deformation patterns (Makris et al., 2021). With earthquake loading, large displacements and velocities can be expected, and with prolonged wind loading, the temperature of the fluid-dampers is likely to increase substantially (Makris et al., 2021). Similar to wind loading, traffic loading on bridges induces vibrations of small amplitude, and over time this can fatigue the damper and lead to failure of the devices(Makris et al., 2021; Matier and Ross, 2013). These issues with fluid-dampers can be both disruptive and costly (Makris et al., 2021). Buckling-restrained braces increase the

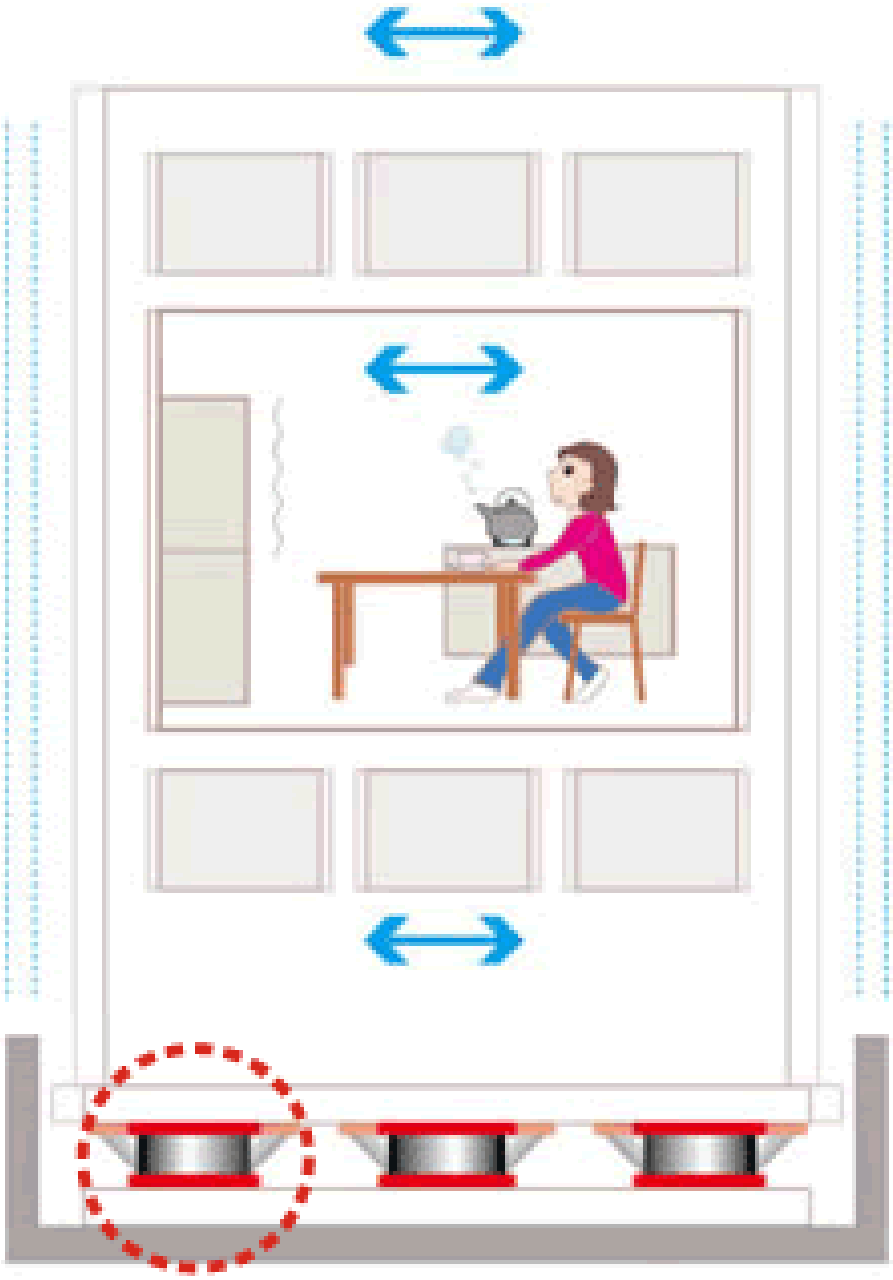

Figure 1.1. Structure with base isolation. Source: BRIDGESTONE Solutions for your journey (BRIDGESTONESolutionsforyourjourney, 2022).

Figure 1.2. Fluid viscous damper. Source: Taylor Devices Inc. (Tay, 2022).

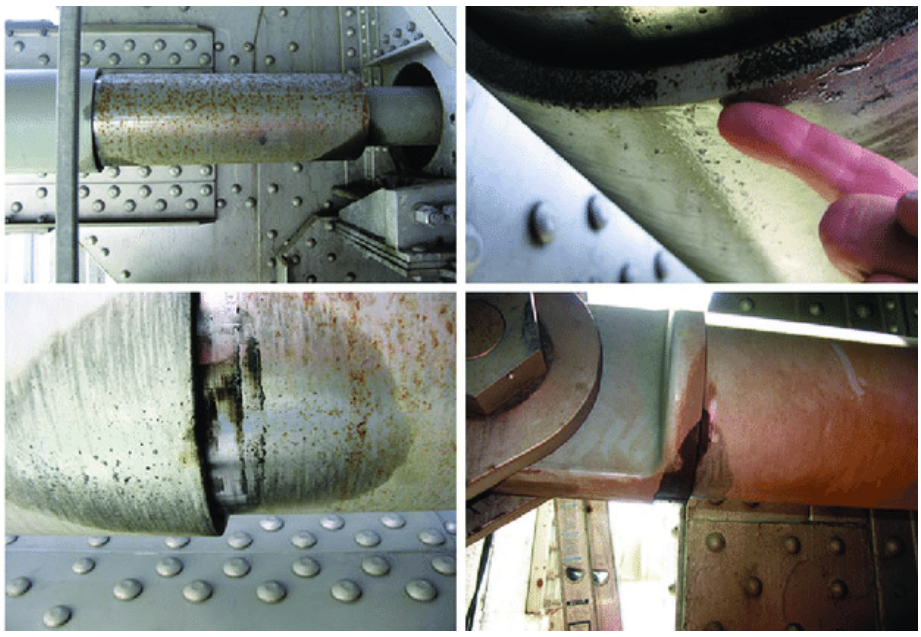

Figure 1.3. Evidence of fluid damper leaking. Source: Dimitrios Konstantinidis *et. al* (Konstantinidis et al., 2015).

strength of a structure while allowing for supplemental hysteretic energy dissipation and are used as an alternative method for the response medication of buildings (Watanabe et al., 1988; Wada et al., 1989; Black et al., 2002, 2018, 2004; Agency, 2006). The distributed yielding leads to a stable hysteretic behavior, resulting in the buckling-restrained braces being accepted worldwide and are now proven to be dependable response modification devices; however, where the displacement demands are small and only up to a few centimeters, buckling-restrained braces are suitable (Makris et al., 2021). The idea for the development of an innovative pressurized sand-damper (PSD) is being proposed due to recent failures of fluid-dampers and the displacement limitations of buckling-restrained braces (Makris et al., 2021).

This device has many advantages, for example, the symmetric force output is nearly velocity-independent due to the friction along the sand-steel interface being temperature-independent. In addition, heat challenges that could cause failure do not affect the performance of the device. This device can be used in harsh environments with extremely high or low temperatures. Strain gauges are utilized to monitor the exerted output force from the sand damper, and they are inexpensive and reliable, while the nominal pressure can easily be adjusted with additional post-tensioning. Furthermore, this system is environmentally friendly and coincides with the current trends for sustainable engineering due to its stability and simplicity in its design (Makris et al., 2021). Sand was selected as the dissipative material because of its dissipative performance that granular materials exhibit within minutes depending on the temperature (Saeki, 2005; Shah et al., 2009; Bannerman et al.,

2011; Heckel et al., 2012; Sack et al., 2013). The pressurized sand damper (PSD) utilizes the pressure-dependent strength of the yielding sand as well as its effect on increasing the dissipated energy during cyclic motion (Makris et al., 2021). Although PSDs serve as the modern philosophy of response modification, it only consists of traditional materials, such as sand and steel, together with the use of post-tensioned steel rods (Makris et al., 2021).

1.2. Outline

This research is focused on energy dissipation in a sand damper under cyclic loading. In this case, the particle dampers consist of discontinuous grains that can be modeled as a collection of discrete particles. Because of this, the discrete element method (DEM) is the computational technique that should be used to model and analyze the proposed sand damper. The history of the energy dissipation mechanism, as well as the concept for the sand damper and its benefits and characterization are highlighted in the literature review in Chapter 2. The computational framework and the microscale energy components are presented, as well as the results of the DEM test simulations that have been conducted. The details of the discrete element modeling analysis are discussed in Chapter 3 and the validation results can be seen in Chapter 4. The results of the conducted tests are presented in Chapter 5. Dissipated energy is calculated based on micromechanical considerations. Next, it's compared to the dissipated energy that is calculated and based on the area of force-displacement hysteresis loops. Analysis on the results from the tests that consist of various sand damper configurations are also included. The mechanical behavior of the energy dissipation and its related energy performances are highlighted in Chapter 5. Finally, the conclusions and future work are presented in Chapter 6.

Chapter 2

LITERATURE REVIEW

The proposed pressurized sand damper is a type of particle dampers. Its resulting energy dissipation is a relatively novel concept being explored and is greatly different than commonly used collision-based particle dampers. Particle-based damping systems provide means to mitigate the response of the structure. This response is assessed by the energy dissipated by a group of particles, which are embedded in the structure or attached enclosures. The damping systems provide the dual advantage of exploiting the properties of solid-like and fluid-like material. In this regard, the solid-like properties allow for temperature to be an independent factor in the system, while the fluid-like properties allow the flow and rearrangement of the particles to facilitate fatigue-free performance (Shah et al., 2009).

Particle damping has been the basis of several research efforts in aerospace and machinery fields. It explores the use of Discrete Element Method (DEM) in simulating a multi-degree-of-freedom structure. They also introduce a simpler model whereby the particles are modeled as a single mass in Finite Element Method (FEM) and explore the benefits of both FEM and DEM. The use of particle damping in civil engineering is at its infant stage. Particle damping technology involves the use of small particles to dampen the impact of vibrations. A combination between the inelastic collisions of the particles and the friction between has a strong impact on damping (Fang et al., 2007; Liu et al., 2005; Wong et al., 2009; Mao et al.,

2004).

Some benefits of particle damping include the ease of its application, its low cost, and durability in both extreme environments and a range of frequencies (Panossian, 1992; Friend and Kinra, 2000; Hollkamp and Gordon, 1998; Fowler et al., 2000; Simonian, 1995). The application of particle damping technology has been used in a wide variety of applications from space shuttle engine turbines (Panossian, 1992; Moore et al., 1995) to medical and dental tools (Heckel et al., 2012). However, the particle damping method is not well understood, due in part to its nonlinear nature (Wong and Rongong, 2009; Sánchez and Carlevaro, 2013). Structurally, particle damping is valuable for reducing earthquake and wind damage. Dampers commonly used in this field include viscous dampers (Halperin et al., 2016), viscoelastic dampers (Tubaldi, 2015), metallic dampers (Foti et al., 2013), friction dampers (Miguel et al., 2014), tuned liquid dampers (Wang et al., 2016; Rozas et al., 2016), and tuned mass dampers (Fadel Miguel et al., 2016; Lu et al., 2017a; Miranda, 2016; Rathi and Chakraborty, 2017). However, current issues with these techniques include the loss of efficacy of seismic isolation techniques under extreme horizontal displacement. Additionally, high temperatures can degrade viscoelastic materials. Friction dampers are limited in that in the case of a change of surface condition, if the interacting objects lose a degree of compactness, the damping method will not be as effective. Tuned liquid dampers are prone to leaking and are not applicable in extreme environments. Lastly, tuned mass dampers are limited to a smaller frequency range than particle dampers.

Particle dampers use large quantity of small particles placed in a vibrating structure to dissipate the energy. The particles can be made from many different materials, and the mechanism of dissipation uses both inelastic collisions and friction between the individual particles as they move within the structure. Additionally, momentum exchange between the particles leads to stored kinetic and strain energy within the particles in the damping process. Two of the primary benefits of this method are that the damper can perform well in extreme environments such as high temperature or over a wide range of different vibration frequencies.

The first particle damping emerged with the use of a single particle to dampen the vibration of turbine blades (Paget, 1937). The next particle damper placed the particle to move between the two walls of a container (Lieber et al., 1945). This study used a variation of a particle damper, the single-particle impact damper, and this method was applied to airplanes for reducing the impact of vibrations. Since then, particle damping has been explored in its various forms, but the method still poses some challenges to modeling (Lieber et al., 1945). Due to the high noise and relative ineffectiveness, such single-particle dampers have now been replaced with numerous, smaller particles.

Two of the main challenges when modeling particle dampers are the nonlinearity of the amplitude in the system and that many different design parameters, such as the shapes and materials of the structure and particles, add complexity to the system. Therefore, the modeling of particle dampers is often simplified to modeling the conglomerate of all the particles as a single particle. Another solution to the complexity issue involves linearizing

the model for the different conditions, but because this varies under the different conditions, it makes the models difficult to apply. Another challenge with particle dampers is that parametric models are too complex to understand and effectively apply. Mostly, these models are understood by extracting the power dissipated and power trapped directly from the vibration data. The Fourier Transform-based power flow method is one way to do this, and this method was used by Yang (Yang, 2003). Limitations of this approach, however, are that the method is time-averaged and that the vibrations on the damper must be periodic.

One key characteristic of particle dampers are the phases the particles endure during damping, including phases where the particles mimic three states of matter. Since particles in some phases of damping have been likened to gasses and liquids, measurements of granular temperature, granular velocity, and mass density have been introduced (Goldhirsch, 2003). As a result of the fluid-like properties, a hydrodynamic model has been developed for the study of particle dampers (Martin et al., 2005; Ohtsuki and Ohsawa, 2003). However, this model is not applicable to the other damping phases of the particles. As a result, three types of constitutive relations have been developed: soil mechanics (Nedderman et al., 1992), Bingham fluid-like visco-plasticity (Jop et al., 2006), and statistical mechanic kinetic theory (Martin et al., 2005). A combination of all three were used in this study. The hydrodynamic model is useful because it is an effective predictor for the particle dampers, but it is limited by some of the assumptions made in the model and the lack of separation between the microscopic and macroscopic properties. Therefore, DEM can be used to study the details of the particle interactions more directly, barring the tradeoff issue between accuracy and

computational efficiency.

Two of the main simulation methods are hard sphere, which reduces the complexity of contact mechanics, and soft sphere, which allows the particles to overlap. By only calculating the collision events in discrete time intervals, the method ignores events between collisions. One benefit of this model is its simplicity, but it experiences the issue of inelastic collapse (Goldhirsch, 2003), reducing the accuracy of the model. Soft sphere models, on the other hand, use springs and sliding friction interfaces to model the particle collisions and the particles have both mass and rotational inertia. While this model may have a higher accuracy, it is more computationally expensive (Goldhirsch, 2003).

Some main types of traditional particle dampers are featured in the Figure 2.1. From left to right, these four types of particle dampers include the impact damper, the multi-unit impact damper, the particle damper, and a multi-unit particle damper. One variation of the impact damper is the bean bag impact damper which wraps the particles in a bag to place in the cavity. This simultaneously decreases the noise and increases the frequency range of effectiveness. Additionally, a piston-based particle damper was developed which allows the system to be dampened effectively at any range of temperatures. In addition to the previously-mentioned solutions to common issues with traditional particle dampers, there is the beam-like impact damper (Chen and Semercigil, 1993) and the linear particle chain impact damper (Gharib and Ghani, 2013). Each of these are useful for eliminating the directional requirements and increasing kinetic energy dissipation, respectively.

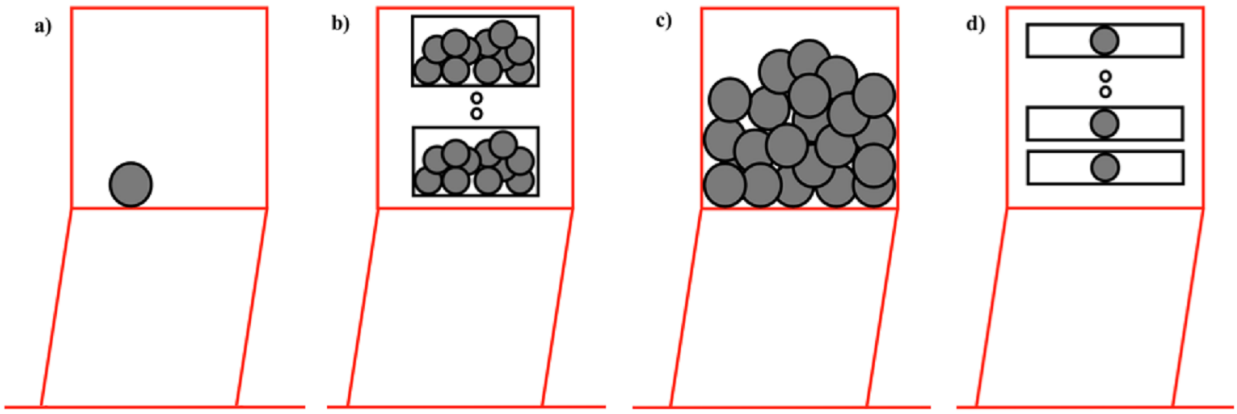

Figure 2.1. Diagrammatic representation of traditional particle dampers: (a) impact damper; (b) multi-unit particle damper; (c) particle damper; and (d) multi-unit impact damper. (modified after Lu et al. (2018)).

Moreover, the flexible restraint particle impact damper, which dates back to the early 1980s, is another name for the bean bag impact damper. When studying the vibration attenuation issue with the boring bar, Popplewell *et. al.* (Popplewell and Semercigil, 1989) utilized this type of dampening technology. As depicted in Figures 2.3 and 2.2, the bean bag impact damper replaces the rigid mass block of the conventional impact damper with a soft bag that has a predetermined elastic resilience and places a specific quantity of metal or nonmetal microparticles inside. Bean bags are better than rigid slugs at damping horizontal, sinusoidal, resonant vibrations. Resonant displacement, acceleration, contact forces, and noise are all reduced. Experience by Bapat and Sankar (1985b) shows that a rigid slug should have the most possible mass and be placed where the speed is highest. These standards attempt to optimize slug momentum. This also applies to beanbags. The bean bag's tight cover adds variable resilience. To account for the tiny clearances, it has been determined that a cover that is only loosely fitted is necessary. When using an empirical approach, it's

possible to start with a small clearance and then shake the bean bag until the lead shot is compacted enough to allow for an increase in the size of the gap. The bean bag impact damper has the advantages of no impulsive noise and a broad frequency range of vibration reduction as compared to the traditional impact damper.

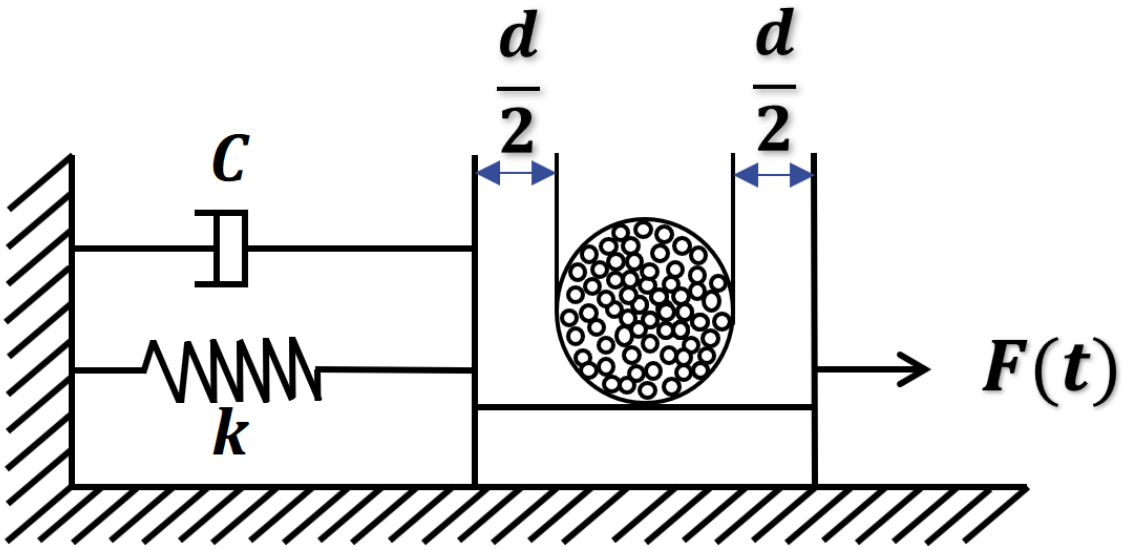

Figure 2.2. Mechanical model of bean bag impact damper.

Figure 2.4 illustrates how the piston-based particle damper introduces a damping pole on the foundation of the nonobstructive particle damper (NOPD). When the primary structure vibrates, the damping pole and the particles collide, press, and rub against one another, transforming mechanical energy into thermal and acoustic energy, which produces the damping effect. By experimentation, Binoy *et. al.* (Shah et al., 2009) discovered that the damping effect of such piston-based particle dampers is totally irrelevant to temperature.

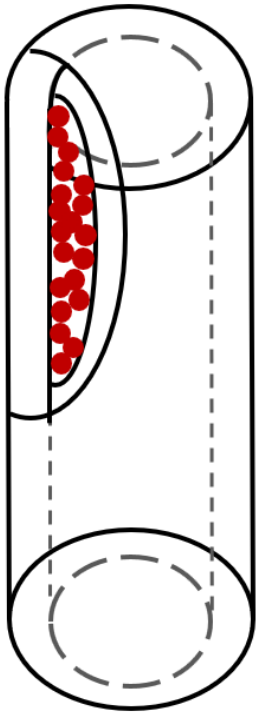

Figure 2.3. Schematic diagram of bean bag impact damper.

Additionally, it can continue to exert damping effects even in the presence of minor external excitation, whereas the impact damper typically loses its effectiveness in such circumstances. Moreover, the displacement decrease is nonlinear, and the damped frequency is bigger than the undamped frequency. Because of these two scenarios, neither a viscous nor a frictional damping model can accurately depict the damping behavior. When designing a damping system, the particle properties and damping device parameters should be appropriately considered because they can affect damping performance by influencing particle flow patterns, packing density, and granular stress. This study (Shah et al., 2009) suggests that because of free-flowing particles, the size, mass, and surface characteristics of particles should be chosen to maximize their flowability. The particle bed has an optimal value for its radius. Below this value, piston jamming occurs, and above it increases the size and mass of the device without providing additional damping. The damping rate is also affected by the starting position of the piston. The starting position of the piston is defined by the immersion depth of the piston and the direction and magnitude of the initial amplitude. When displacements begin above the equilibrium position, greater damping is produced, and the damping rate is unaffected by variations in the initial amplitude.

Later, Shah et al. (2011) proposed to accomplish semi-active control using a magnetic field, as illustrated in Figure 2.5, based on the piston-based particle damper under passive control . The purpose of this research was to look into a semi-active particle-based damping system that uses a dry magnetic particle bed to absorb and dissipate the energy of a vibrating piston. The damping efficiency can be adjusted by adjusting the electric current

used to generate a magnetic field. In the scenario of a magnetic piston, the magnetization of both particles and pistons can improve damping efficiency until the magnetization reaches saturation. If the particles and pistons are both free of magnetic hysteresis, demagnetization can return the damping system to its original unmagnetized state; thus, the entire system is reversible during the magnetization and demagnetization processes. Damping is demonstrated to be temperature independent within a magnetic field over a certain temperature range. Particularly, damping with chrome steel particles is unaffected by temperature variations ranging from 20 to 140 C^o, despite the particles' magnetization declining by less than 20%. Besides that, the magnetization of a single chrome steel particle remains constant when the temperature ranges from 268 to 0 C^o, implying that temperature variation within this range will not affect damping performance. It is determined that in order to accomplish a predictable damping rate, the particles and piston in a semi-active particle-based damping system has to be ferromagnetic and free of magnetic hysteresis. Magnetic materials should always be chosen for applications at high temperatures relying on their melting point and Curie temperatures.

Due to their flexibility, a few particular constructions, including a flexible mechanical arm and a cantilever beam, would cause a noticeable immediate movement if stopped suddenly when moving swiftly. The beam-like impact damper developed by Chen and Semercigil (1993) is a solution to the problem of impulsive instantaneous vibration damaging the structure. In comparison to the conventional impact damper, the beam-like impact damper can eliminate the direction dependency of its damping efficacy. To enhance kinetic energy dissi-

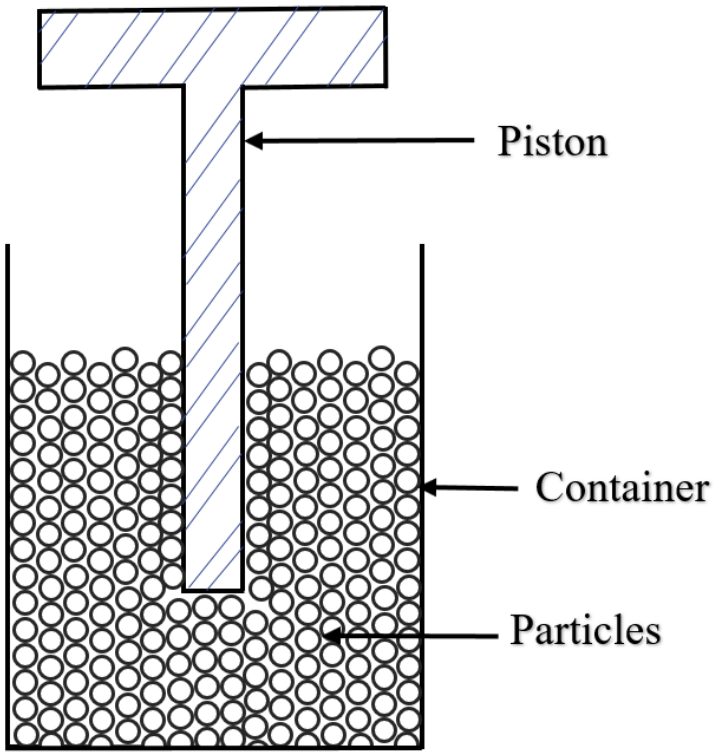

Figure 2.4. Diagrammatic representation of the piston-based particle damper under passive control

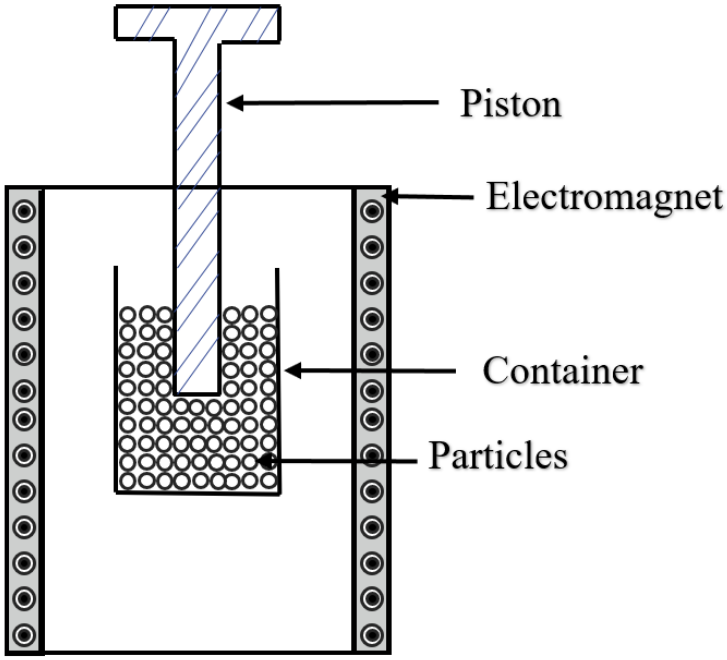

Figure 2.5. Diagrammatic representation of the piston-based particle damper under semi-active magnetic field control

pation during the collision process, Gharib *et. al.* (Gharib and Ghani, 2013) introduced a unique impact damper called as the linear particle chain impact damper. As shown in Figure 2.6, this impact damper was made by sandwiching a small ball between two huge balls. This impact damper offers new tools for designing effective structure damping systems and can be used in a variety of industries. The LPC impact damper is made up of a linear chain of spherical balls that alternate between large and small balls. The new impact damper is based on an innovative energy absorption method that takes advantage of multiple impacts between spherical balls. The energy absorption method performs by sandwiching a small ball between each larger ball in the chain. As a result, when the primary system is activated, the small ball collides with a large number of larger balls. The kinetic energy is dissipated as a consequence of numerous collisions between the small and large balls.

By comparing its responses to those of a conventional single unit impact damper, the LPC impact damper is validated. The numerical results demonstrated that the LPC impact damper reduces vibration significantly more than the conventional impact damper. A parametric study was carried out to determine the effect of the damper clearance, ball gaps, ball mass ratio, and coefficient of restitution. It was discovered that decreasing the damper clearance, increasing the damper mass ratio, and using spherical balls with a low coefficient of restitution improved system response. Nevertheless, in order to select these parameters based on the damper application, a design compromise is required (Gharib and Ghani, 2013).

In addition to the structural developments in particle impact dampers mentioned above, new materials were explored to increase performance and reduce challenges. One study (Li

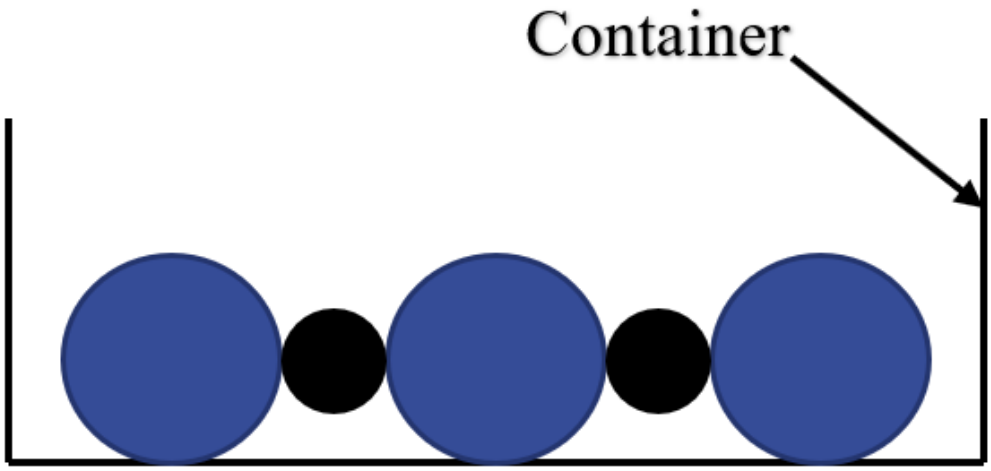

Figure 2.6. Schematic diagram of linear particle chain impact damper.

and Darby, 2008) used rubber to coat the inner wall of the damper. This led to increased performance and reduced the noise. Another material explored was the use of fine particles around steep spheres which helped permanently reduce the vibration of the main structure (Du and Wang, 2010). A similar variation by Darabi and Rongong (2012) used more viscoelastic particle to replace the more rigid particles traditionally used, which resulted in particles reaching a convection region at a high amplitude. Bustamante et al. (2013) took this a step further by replacing the particle material with an elastomer. At the fluidization point, it was found that the particles were able to achieve maximum damping at their optimized excitation level. Another replacement material used was soft, hollow particles (Michon et al., 2013). This method utilized the properties of honeycomb structures, resulting in strong performance at a wide range of frequencies and a reduction in stress on the primary

structure. Lastly, Abbas et al. (2014) used rubber spheres to substitute metal swarfs, and it was found that the metal swarfs can be highly effective at damping over a broad range of both frequencies and amplitudes. The combination type particle dampers are a useful compromise for particle damping technology because they can improve the damping capability relative to other damping technologies, but it sidesteps the congested development of particle damping applications. This sort of version primarily consists of the combination of impact damper and tuned absorber, particle TMD, and tuned liquid particle damper. The first example of this emerged with research by Masri (1972) and involved a combination of the impact damper with a tuned absorber. Masri used a dynamic vibration neutralizer and motion-limiting stops which provided a solution under steady-state conditions and verified the value of such damping systems under various conditions. Next, the tuned particle damper involved the use of a particle damper combined with flexible supports which helped the particle damper be more effective at low vibration acceleration (Yao et al., 2014) as shown in Figures 2.7 and 2.8.

The particle tuned mass damper (PTMD) is another variation which couples particle damping with tuned mass dampers (TMDs) to create a nonlinear energy-consuming system, which increases the performance at a wide range of frequencies and improve robustness. For high-rise building vibration control, PTMD has been introduced to the shaking table tests and wind tunnel testing, during which the PTMD is suspended on the primary structure by four equal-length strands, which are attached to the primary structure. A considerable impact on the reduction of high-rise building vibration caused by wind and earthquake has

been demonstrated by utilizing the PTMD (Lu et al., 2017b, 2016, 2017b). This has been studied in civil engineering applications where it has been shown to help reduce the impact of wind and earthquake vibration on structures. Lu et al. (2018) assessed the physical state of various particle impact dampers. A study conducted by Yan et al. (2014) shows how to create tailored particle dampers for continuous viaducts. A 1/10 scale model bridge was shaken with and without adjustable particle dampers to evaluate system performance and verify analytical method. Using a finite-element model and an analytical energy approach, the damper's behavior was simulated. Experimental and analytical results reveal that the preliminary design method for tuned particle dampers can be used to control the seismic response of bridges. A tailored particle damper reduces a viaduct's seismic reactivity. Excitation intensity affects a tuned particle damper's performance. Tuned particle dampers have a wider control frequency band than tuned mass or liquid dampers. Using a finite-element model, the simplified method simulates the damper's action (Yan et al., 2014).

The two main ways that the particle damping method absorbs energy is through the energy consumption between the particles and the impact between the particles and the surface of the primary fixture. While variations of particle damping have been implemented for hundreds of years, there is still some debate about the primary way that damping is achieved. Lenzi (1985) proposed that the main method for energy consumption was through friction. However, Kerwin Jr (1965) proposed that the primary energy consumption comes from friction as well as nonlinear deformation of the particle contact points and particle material resonance. Another prominent theory by Sun et al. (1986) is that the acoustic

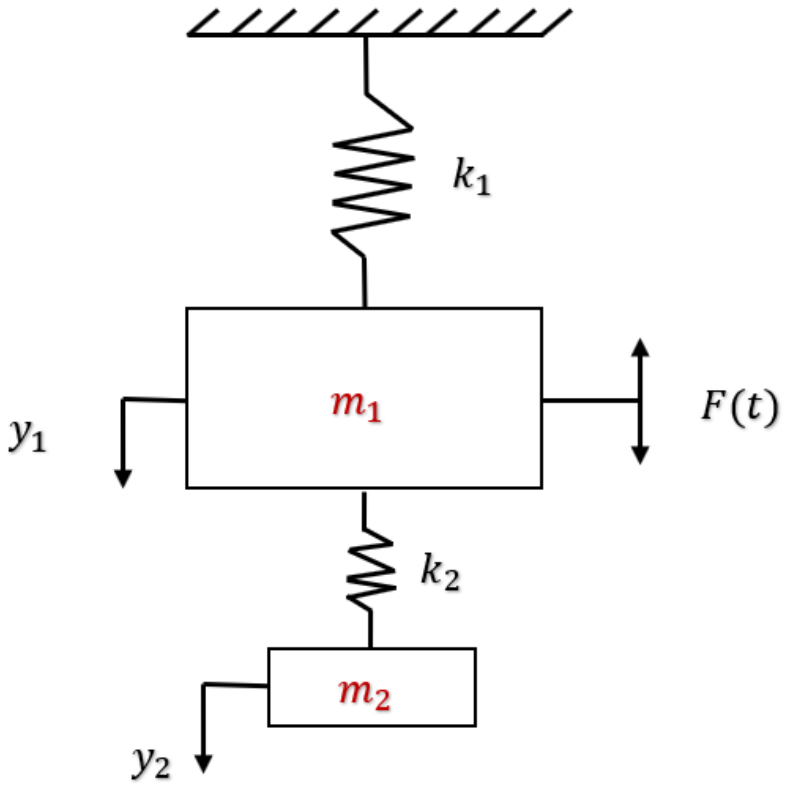

Figure 2.7. Mechanical representation of a classical dynamic vibration absorber.

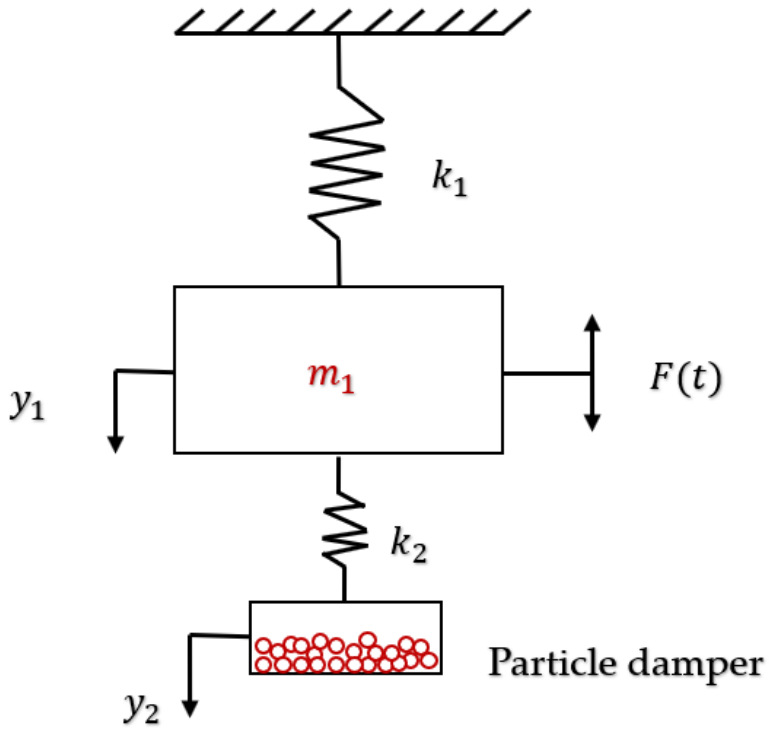

Figure 2.8. Mechanical representation of the tuned particle damper.

energy consumed by the particles results in the damping. All of the theories can be reduced to two main thought processes: that the nonperfect elastic collision results in the energy loss, and that the momentum exchange results in the damping effect. Using DEM, it was discovered that friction is a primary contributor to the damping effect, but that the friction coefficient does not vary much with respect to the amount of energy consumed (Wong et al., 2009). Masmoudi et al. (2016) found that the total mass of the particles and the amplitude of excitation had the highest influence on energy consumption. Lastly, Zhang et al. (2016) found that for the nonobstructive particle damper (NOPDs), the energy was dissipated in the form of both thermal energy and potential energy.

A common explanation for particle damping has yet to be found, despite a great deal of effort by researchers worldwide. Nonlinear energy sinks (NESs) are vibration absorption technologies extensively explored in various industries, including machinery, aerospace, and civil engineering (Gourc et al., 2015; Bergeot et al., 2017; , Lu). TMDs and nonlinear absorbers of this type have some similarities. A substantial displacement should be used to minimize the response time of each of these components by moving the excess mass (as for building structures, it is usually at the top story). The main distinction between TMD and NES is that TMD generates linear resilience, whereas NES generates nonlinear resilience. Since linear oscillators typically have a single inherent frequency, NES differs from them. Vibrational energy affects changing the fundamental frequencies of NES. This means that the fundamental structure of NES can be heard in numerous modes across a wider spectrum of frequencies. In other words, NES is capable of achieving the goal of minimizing vibration

for a wide range of frequencies (Vakakis, 2001; Lee et al., 2008; Roberson, 1952). The pounding TMD was created when Li and Song Zhang et al. (2013); Li et al. (2015); Zhang et al. (2015) applied impact energy dissipation to the classic TMD. The heat created by the impact of pounding between a tuned mass block and a delimiter covered in viscous-elastic material can be used to disperse vibration energy in this system. Because of this, pounding (TMD), a dynamic vibration neutralizer with motion-limiting stops is also considered a type of NES with good resilience. It has also been used to operate subsea jumpers as well as power transmission towers (Heckel et al., 2012; Wong and Rongong, 2009; Zhang et al., 2013). Figures 2.9-2.14 depict the mechanical models of various types of dampers.

In the first study of impact dampers (single-particle) by Lieber et al. (1945), each collision was considered as purely elastic. Later Grubin (1956) added the elastic restitution coefficient to the study of the system, accounting for the lost energy during the collisions. Masri (1970) later added the same concept to symmetric collisions that occurred twice during each cycle. Bapat (1998) added nonlinear control equations to help analyze vibration state for more than two collisions per cycle. Masri (1969, 1970, 1967a) later determined an analytical solution and Bapat and Sankar (1985b,a) studied the impact of Coulomb friction on the system by creating a table that shows the optimum gaps and amplitude reduction when the system undergoes forced vibration. Bapat and Sankar (1985b) Ema and Marui then built on Bapat and Sankar's work by Ema and Marui (1994) showing that the damping effects are a result of the collisions between the impact mass and the primary system. Lastly, Duncan et al. (2005) studied the vertical impact damper.

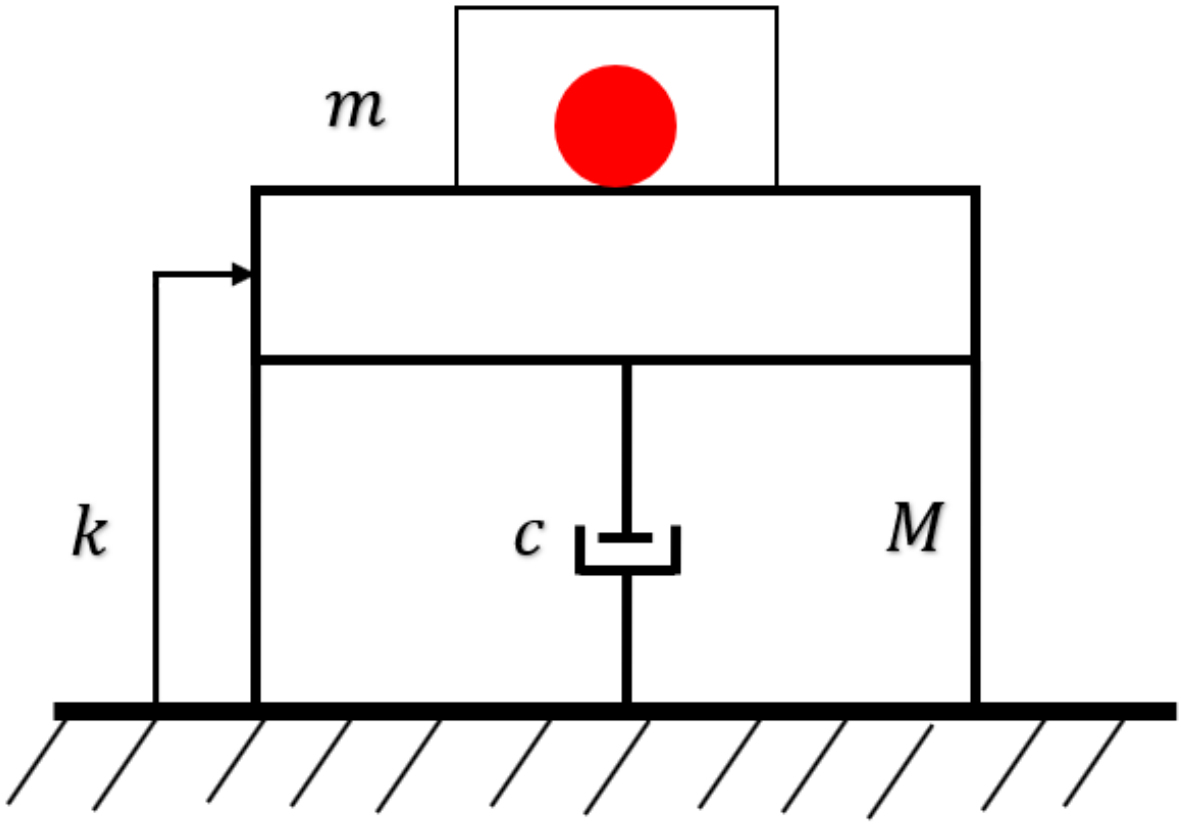

Figure 2.9. Mechanical representation of the impact damper.

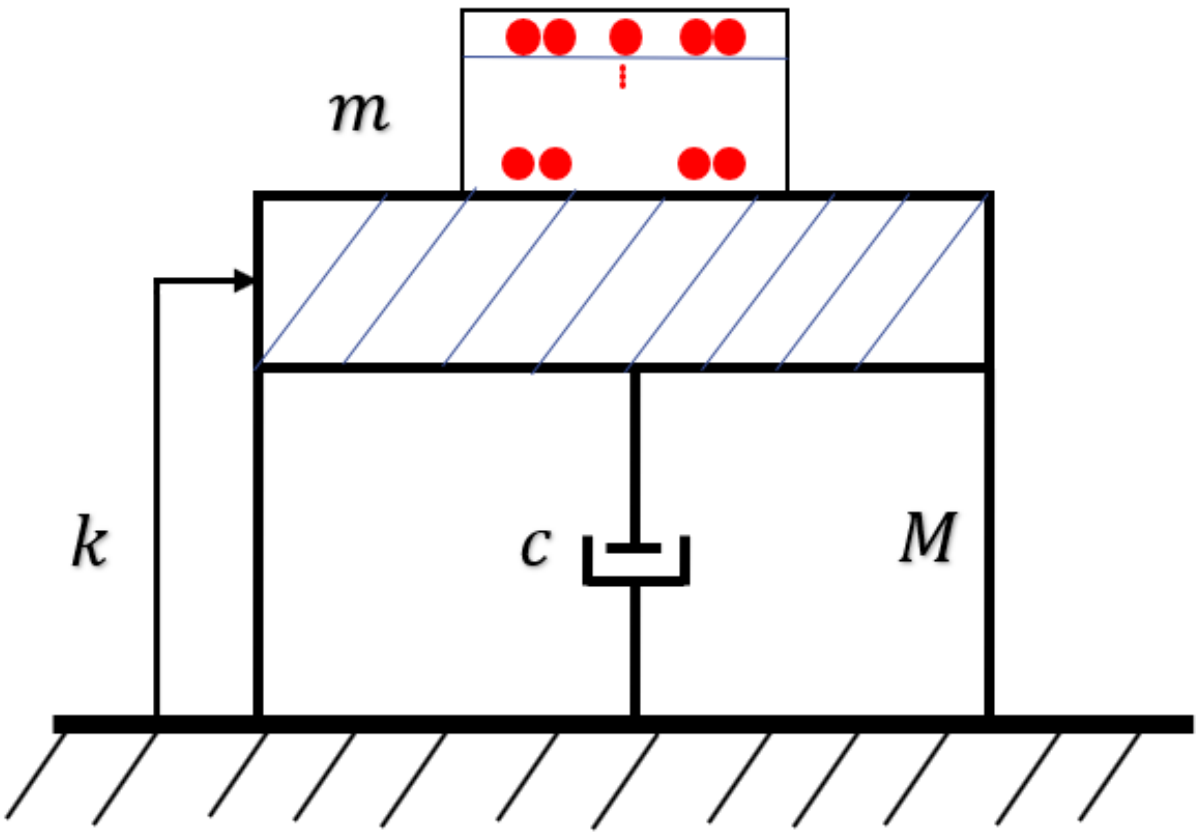

Figure 2.10. Mechanical representation of the particle damper.

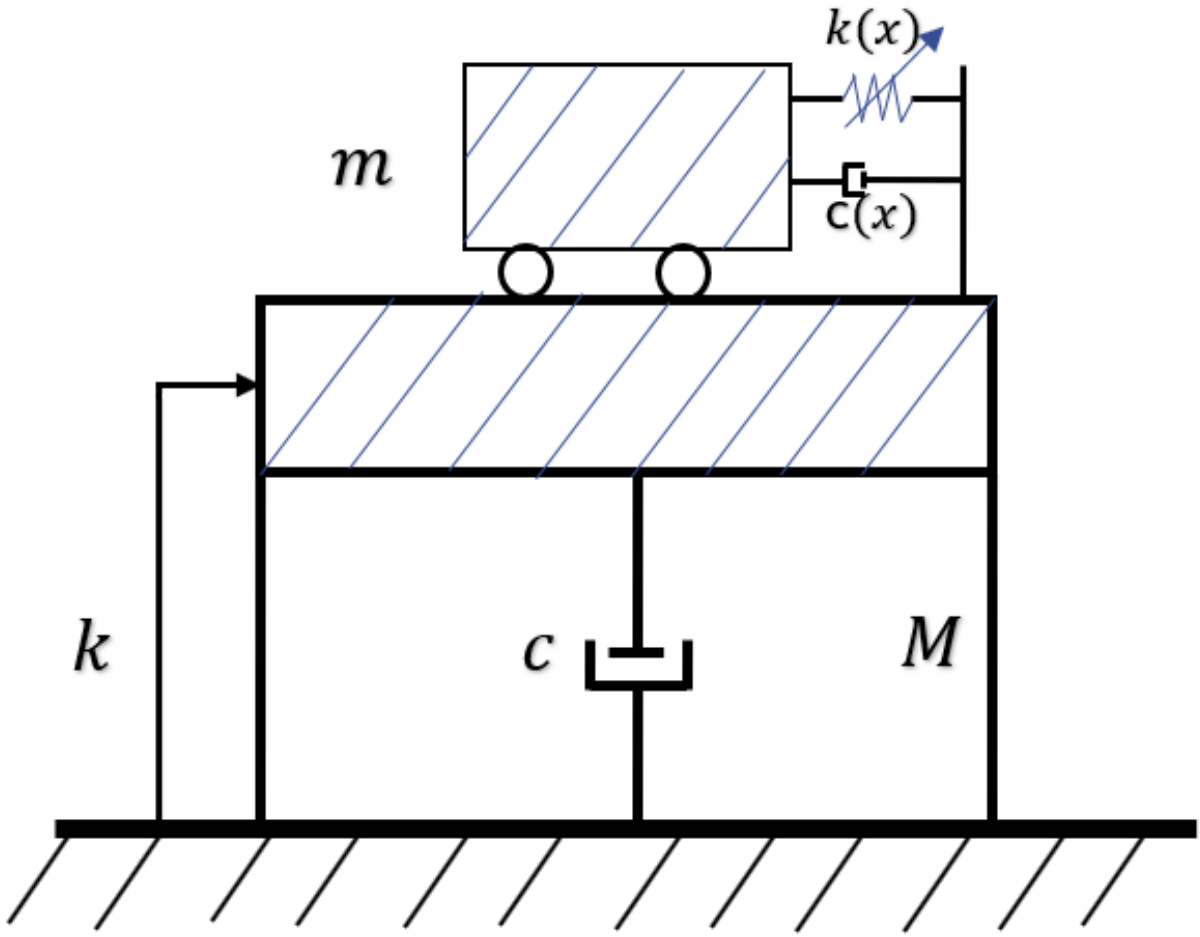

Figure 2.11. Mechanical representation of the nonlinear energy sink.

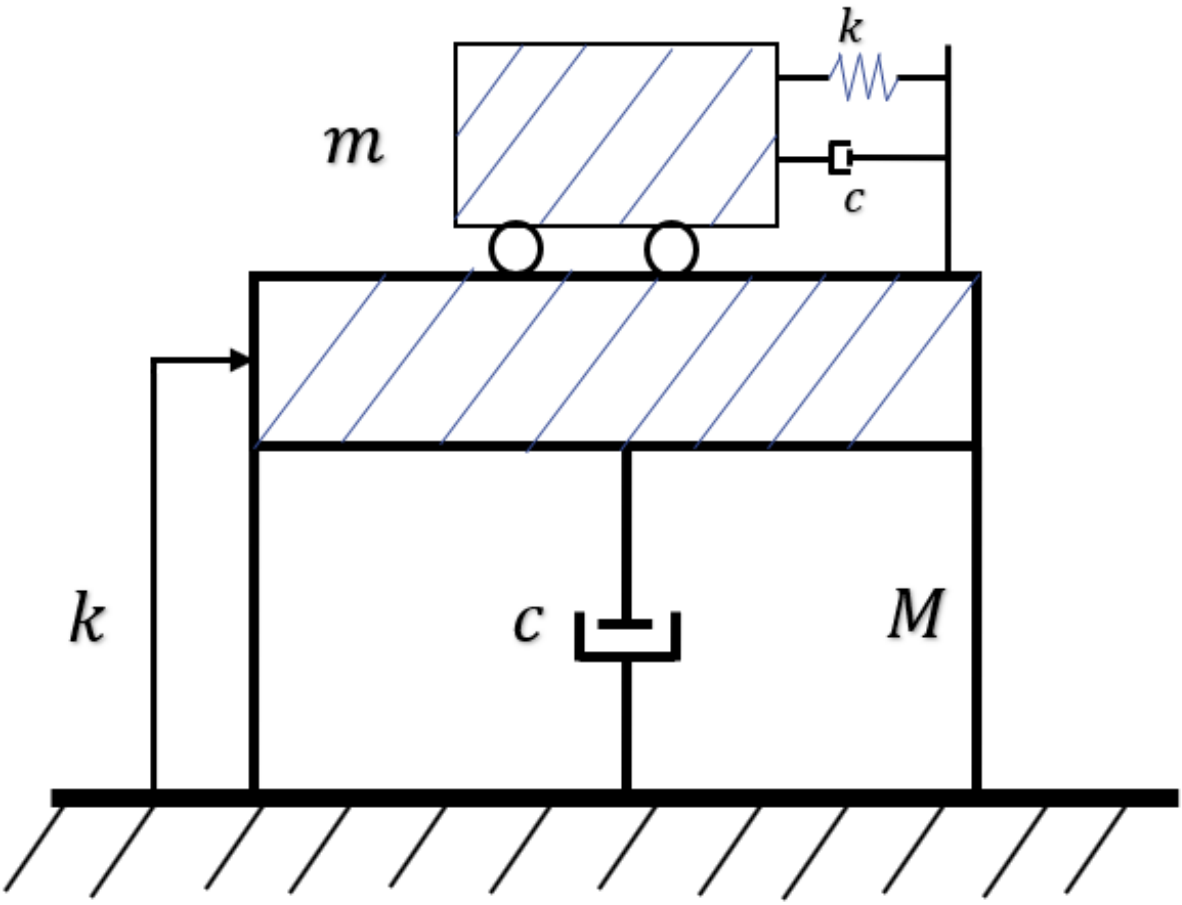

Figure 2.12. Mechanical representation of the tuned mass damper.

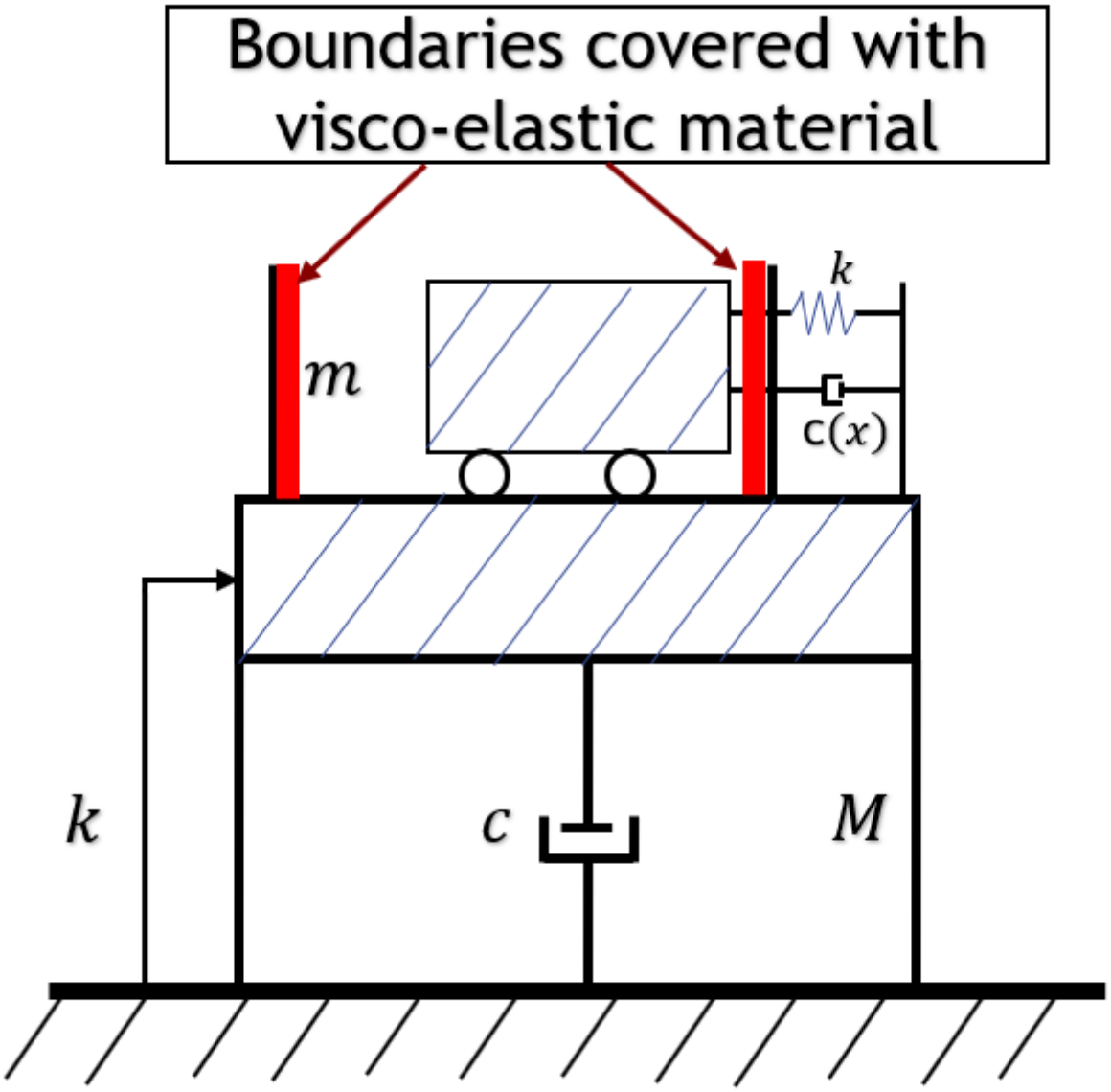

Figure 2.13. Mechanical representation of the pounding tuned mass damper.

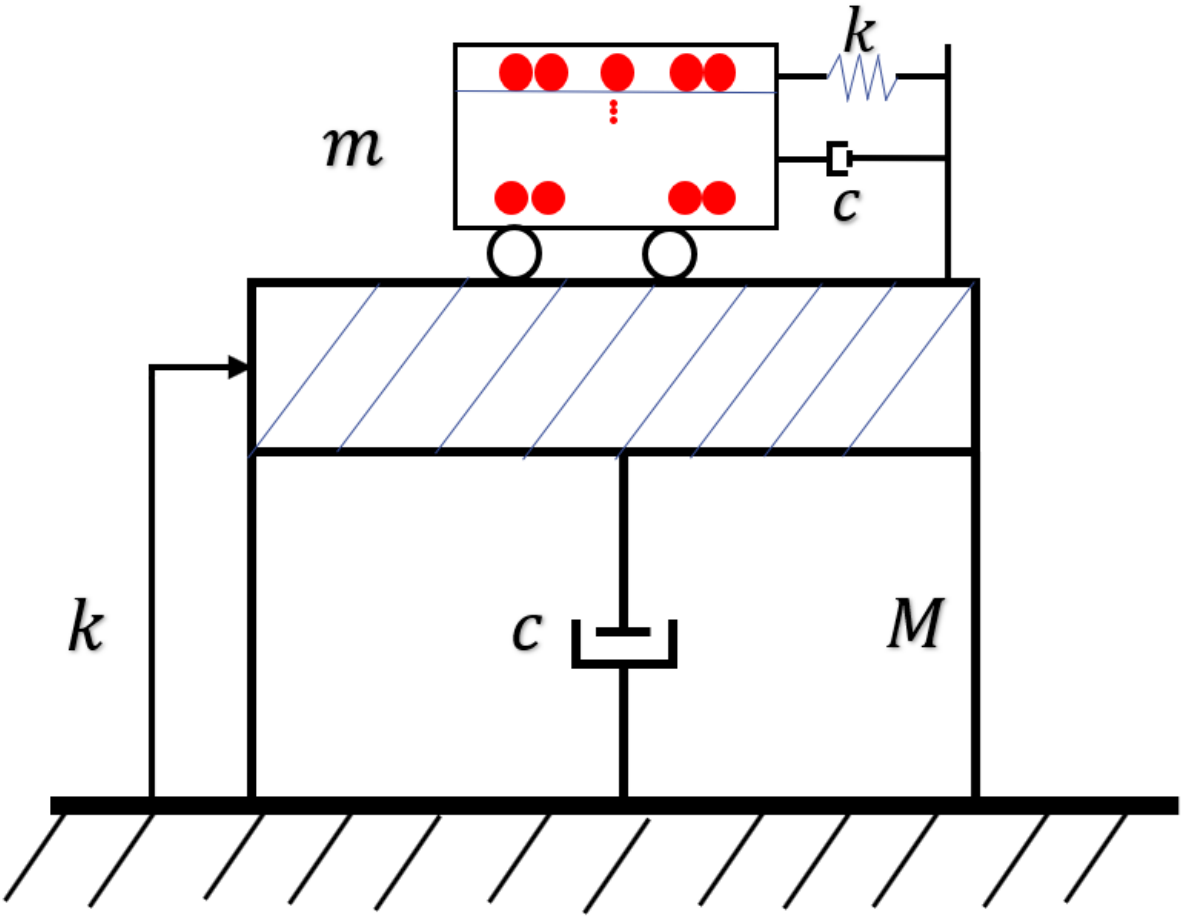

Figure 2.14. Mechanical representation of the particle tuned mass damper.

Analysis of dampers with multiple particles is more complex than that of single-particle dampers. Masri (1967b) was able to develop one example of an analytical solution, but many analyses depend on theoretical and numerical experimentation. Mao et al. (2004) simulated particle damping via DEM to demonstrate that a combination of impact damping and friction damping can generate additional damping over a finite period. Salueña et al. (1999) used molecular dynamic simulations to study energy dissipation of the particles and found that the rate of energy loss can be classified into solid, convective, and gas-like. Sánchez and Carlevaro (2013) explored dynamic particle interaction with DEM and showed that an increase in excitation frequency results in a switch in a particle from periodic motion to chaotic motion. Romdhane et al. (2013) developed a different experimental method to measure the loss factor of NOPDs quantitatively. Lu et al. (2011b,a, 2010) introduced the concept of "effective momentum exchange" which shows the physical properties of the particles' movement and serves as an index for finding the optimal damping performance.

Additional research has been conducted to allow the particle damping system to be studied in a simplified manner numerically. First, the system was studied as a single-unit impact damper by Papalou and Masri (1996a,b, 1998). For such a simulation, it was necessary that the different types of energy dissipation be combined into a single metric. This came to be known as the effective coefficient of restitution, and it was studied by Friend and Kinra (2000). They accomplished this by fitting the data to the results of experimental testing. Using a similar method of fitting numerical data to experimental results, Liu et al. (2005) and Xu et al. (2004) contributed to understanding the nonlinear aspects of particle damping.

Wu et al. (2004) combined multiphase flow theory with the study of particle dampers, Fang and Tang (2006) added to the model by simplifying it and reducing the computation time. One issue with these studies, however, is that many of them can be difficult to extend to other applications.

In recent decades, several developments have been made regarding how to model particle damping. Granular dynamics (GD) are simulations that model discontinuous grains as discrete particles. Two approach groups are used for this type of analysis: soft and hard contact. The discrete element method is the soft contact approach used for most GD models. The discrete element method (DEM) was first introduced by Cundall (1971) and is nearly a Lagrangian technique because individual particle is treated separately and it allows for large strain deformation. It allows researchers to include both the inter-particle interactions and the interactions between the particles and the wall. Inter-particle contact forces are determined using models like springs, dashpots, and frictional sliders. This method works such that each of the particles are modeled as discrete entities and it allows each of these elements and their movements to all be studied in relation to each other. The numerical integration of Newton's equations of motion is used to determine the particles' motion. Any assumptions about the solid's rheology can be disregarded. Dry cohesionless soils are typically assessed using discrete element modeling (Ng, 2004; Wang et al., 2008; Jiang et al., 2006; Iwashita and Oda, 1998; Bathurst and Rothenburg, 1988; Kuhn and Mitchell, 1992; Thornton, 2000; O'Sullivan and Bray, 2003; Bolton et al., 2008; Evans and Frost, 2010)

Granular particle dampers serve inhibit the effect of vibrations on a primary structure through passive vibration control and the subsequent absorption and dissipation of energy among the particles (Friend and Kinra, 2000; Mao et al., 2004). Some benefits of particle damping are that it is easy and inexpensive to retrofit, it is effective in harsh environments and over a wide frequency range (Saeki, 2005), and it dissipates energy without a significant impact to the weight or stiffness of the primary structure (Friend and Kinra, 2000; Saeki, 2002, 2005). While particle damping has many benefits, it has been difficult to model due to the various types of interparticle collisions, particle-wall collisions, and friction (Mao et al., 2004), and the nonlinear nature of the collisions (Fowler et al., 2000). Previously, this has been studied effectively and applied using DEM (Cundall and Strack, 1979; Tijskens et al., 2003; Chen et al., 2001), a numerical simulation which applies Newton's equations to mimic the interparticle interactions of small-step collisions over a longer time period. This allows the system to capture small collisions between particles before they spread into collisions with other particles (Cundall and Strack, 1979). However, in order for the simulation to be accurate, the force-displacement model must adequately govern the movement of the particles, and there must be an efficient way to determine which particles are in contact with each other (Tijskens et al., 2003; Grest et al., 1989; Vemuri et al., 1998). While there are currently algorithms to identify the contacts (Saeki, 2002, 2005), they are still computationally expensive. Part of the reason for this is that motion of the particles depends on the motion of the primary structure, so positions change quickly with time, making them more difficult to detect. Additionally, due to the nonlinear nature of the motion, it must be studied over long

periods of time, further adding to the computational expense, especially at low frequencies. Therefore, it is important to improve the computational efficiency of the DEM simulations to better understand the damping mechanisms and optimal application of particle dampers.

Research on the use of DEM in geomechanics has been conducted by O'Sullivan (2011). Walton and others have also researched DEM and analyzed its ability to model granular shear flow (Walton and Braun, 1986; Vemuri et al., 1998; Vu-Quoc et al., 2000; Hanes and Walton, 2000). DEM has also been used recently to analyze particle dampers (Salueña et al., 1999; Fowler et al., 2000; Chen et al., 2001; Mao et al., 2004; Fang et al., 2007; Wong et al., 2009). The hard contact is used by the second group of GD models. This approach assumes the interaction forces are impulsive, meaning the transfer of particle momentum can only occur when they collide, which are instantaneous and processed one at a time. The time steps on the same order of magnitude as the length of the intervals between collisions, which are typically larger than what is required. This approach, which uses a two-dimensional model to simulate granular shear flows, has previously been studied by Campbell and Brennen (1985). The analysis of the collision-based GD approach in geomechanics has also been researched in many studies (Pytlos et al., 2015b,a; Izadi and Bezuijen, 2015, 2018; Lee and Hashash, 2015).

In harsh conditions, granular damping could reduce vibration. DEM is utilized in granular damping analyses involving a large number of grains. While the discrete element method, which is based on direct numerical integration of Newton's equations, has been widely used to investigate granular motion, granular damping presents unique difficulties. Grain movements

are tightly related to the host structure in granular damping analysis, and grains collide often. The energy dissipation mechanism is highly nonlinear and necessitates a lengthy simulation time, particularly for low-frequency structures. Using the discrete element method, a new computational scheme for analyzing granular damping was created by Fang et al. (2007). This study investigated the effectiveness of contact detection, which is an approach combining an improved LC method with an adaptively updated Verlet table. In addition, the effect of time step in simulation and provide a method for optimizing the selection of time step based on the contact duration of given granules was investigated. Collectively, these enhancements resulted in a highly efficient discrete element approach that can multiply the computing efficiency of granular damper analysis compared to the current state of the art. This new approach is ideally suited for large-scale granular damping analysis. This method was validated by connecting numerical and experimental benchmark findings. On the basis of the novel algorithm, case studies on a large number of granules were conducted to demonstrate the parametric analysis of granular damping mechanisms and the enhancement of damping performance (Fang et al., 2007).

Fang et al. (2007) addresses the optimization of particle damping performance based on varying the different parameters under harmonic force excitation. The particles move according to Newton's motion equations, and involve both translocation and rotation, and at each contact point the forces are calculated according to a force-displacement law. Using the radius of the particles, a contact is detected when the centers of two particles are sufficiently close. These contact forces are then modeled using a spring, dashpot, and slider (Tsuji

et al., 1992, 1993). In contrast to previous studies with linear modeling (Zhang and Whiten, 1996; Mishra and Murty, 2001), this study uses a nonlinear contact model based on Hertzian contact theory. It was shown that particle damping resulted in an 81.3% reduction in peak amplitude, and it was effective over a wide frequency range. Additionally, it was found that under certain conditions, the damping effectiveness can be increased by changing the number of particles while keeping the total mass constant. For this setup, the optimal number of particles was 490. More particles result in more collisions, resulting in a higher damping effect. However, the damping effect also depends on the amount of energy dissipated in each collision, which changes with the size of the particles. For that reason, optimal performance of the particle damper finds an optimal value which does not simply maximize the number of particles. However, this can be further improved by including non-homogenous particle sizes in the damper. This study developed an improved method for the DEM simulation of particle dampers. The model used by Fang et al. (2007) shows that the utilization of both the LC method and a Verlet table to reduce the number of contact points that must be calculated, thus improving the computational efficiency of the model. Not only was this found to be an accurate and efficient method, but it was further tested to understand optimal performance measures for a particle damper. From this, it was found that granules of mixed sized improved the effectiveness of the particle damper (Fang et al., 2007).

Tong and Wang (2015) study observed the impact of particle size on shear modulus G and damping ratio D through shear tests conducted using DEM. The researchers used a nonlinear contact model and clumped particles to provide a more realistic simulation. The results

showed an inverse relationship between shear modulus and particle size, but they showed a direct relationship between damping ration and particle size. The two methods used to calculate G and D were by the traced energy and the hysteresis loop. Additionally, when the particle size became sufficiently small, differences in the shear modulus and damping ratio became negligible. Decreasing the sphericity of the particles resulted in increased G and decreased D. Lastly, the researchers explored the effect of aging on G and D and found that age increased the shear modulus and decreased the damping ratio.

As mentioned earlier, this use of particle dampers was first explored in 1945 by Lieber et al. (1945). The study used a variation of a particle damper, the single-particle impact damper, and this method was applied to airplanes for reducing the impact of vibrations. Since then, particle damping has been explored in its various forms, but the method still poses some challenges to modeling. Wong et al. (2009) study used the DEM approach to mechanism of energy dissipation for particle dampers as well as determine an appropriate way to model the complex nonlinear collision process. Of the energy dissipation mechanisms, the contact conditions in particular are explored using small particles of <3mm diameter and the measurements were collected for both the coefficient of restitution and the interface friction. Additionally, the complex interactions between the particles pose a computational challenge whereby a balance must be established between model accuracy and computation time.

The simplified analytical method studies all the particles involved as a single unit, and this method was proposed by Lu et al. (2017b). While this method has been accurate enough

to support practical applications, it neglects the particle-to-particle interactions. Sánchez et al. (2012) has addressed this concern by demonstrating that the particles behave like a single mass when there is a sufficient number of particles and therefore the effect of the particle-to-particle collisions is negligible. In addition to supporting the simplified analytical method, this shows why particle dampers are effective in extreme conditions and it helps to simplify the modeling of particle dampers.

The primary current applications of particle dampers include securing structures under wind and earthquake conditions. Other passive control technologies have been implemented to structures and this has been well studied in civil engineering. However, the applications of particle damping mechanisms are still developing. Two examples of particle damping applications include its use as a damper for the pylon of a bridge in Japan (Ogawa et al., 1997) and on the 21st floor of a building in Santiago, Chile (Naeim et al., 2011). Both have performed well. For studying the practical applications of particle dampers in civil engineering, researchers first looked at their impact on smaller components of a structure such as cantilever beams. The results of these studies can then be applied on a larger scale to evaluate their performance on it. Masri (1973); Masri and Kahyai (1974) explored the use of the particle impact dampers on continuous beams. Once the application of particle dampers was explored at the smaller scale, studies looked to examine their use on entire buildings and other structures. In the application of particle dampers for civil engineering, the following four advantages have been found: they are effective over a wide frequency band, they are not as susceptible to temperature and degradation, they are versatile for application, and

they are cost effective relative to other commonly used damping technologies.

One of the disadvantages to applying particle damping methods is that they have not been studied as extensively as other methods. Most of the studies have only included SDOF systems, meaning that there is a lack of analysis of particle damping in MDOF systems. Additionally, this lack of research means that a standardized consensus on design has not been reached. Recent research has shown that particle damping might not be as effective under weak excitation. Other differences include the scale of application – civil engineering structures are often much larger, and the arrangement of the particle dampers may be different. Therefore, more research is necessary on the application of particle damping in civil engineering. Though much research has been conducted on particle damping, there are still many gaps in understanding and a lack of research on applications for civil engineering. While the underlying energy dissipation mechanism is not universally agreed upon, DEM allows a more detailed simulation. However, simpler models may still be preferred for applications. Of the various types of studies, researchers have explored using different materials for the particles and for the container. Additionally, studying particle dampers can be difficult due to their nonlinear nature. Simulations must find a balance which maximizes accuracy while minimizing the computational expense. Particle dampers have been applied in aerospace and mechanical fields, but differences in the application for civil engineering still needs to be explored. Additionally, using DEM techniques could be useful for studying the primary structure and the particle dampers in unison.

In order to mitigate large displacements, one alternative idea is the usage of fluid-dampers. Originally used in military applications as a shock isolation of hardware, fluid-dampers have developed and are used to terminate vibrations caused by earthquakes and wind in structures. For example, in buildings, fluid-dampers are installed in soft stories of structures to reduce the amount of building story drift. In addition, many bridges utilize fluid-dampers to absorb wind, seismic, and pedestrian energies, for example the Bay Bridge connecting San Francisco and Oakland. One challenge experienced with fluid-dampers is their ability to be sustainable in the long-term when faced with different loads, deformations, and displacements. Research by Makris et al. (2021) has shown that traffic loading on bridges creates small amplitude vibrations with long durations, which can lead to the damper failing due to fatigue. Another issue with fluid-dampers is that lengthy wind loading will increase the temperature of fluid-dampers, which can lead to device failure. The use of buckling-restrained braces is another strategy to increase the structure's strength. These braces distribute their yielding, due to the yielding of the inner core which limits displacement to the inelastic elongation of the inner steel core. This allows for the structure to experience more stiffness and have great response devices for applications in which there is minimal displacement. Due to many failures of fluid-dampers and the displacement restrictions of buckling-restrained braces, a pressurized sand-damper, PSD, was created (Makris et al., 2021).

Makris et al. (2021) explored the application of pressurized sand dampers for earth quake and wind engineering systems. This device has many advantages, for example, its symmetric

force output is nearly velocity-independent due to the friction along the sand-steel interface being temperature-independent. The schematic of a pressurized sand damper (PSD) is shown in Figure 2.15. In addition, heat challenges that could cause failure do not affect the

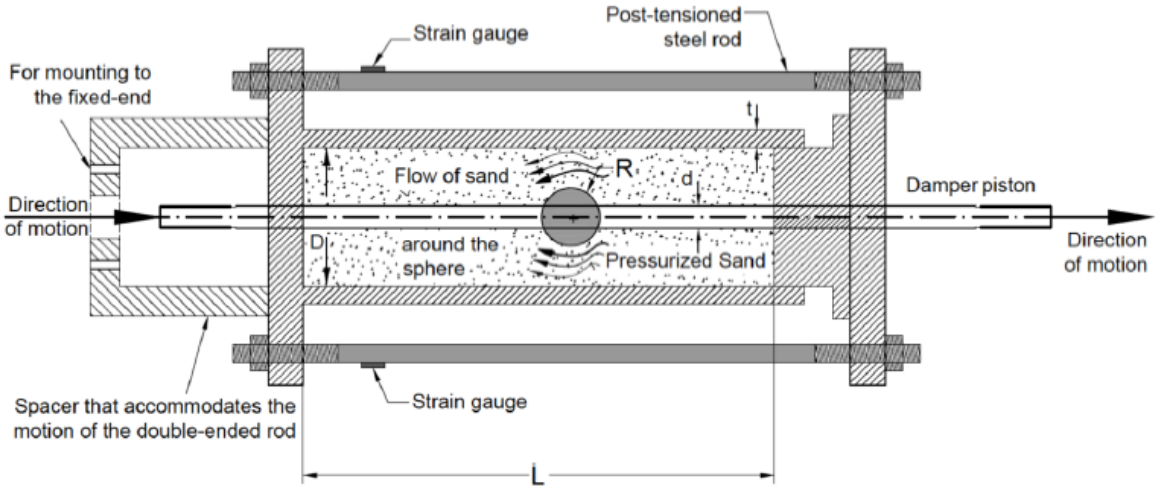

Figure 2.15. Schematic of a pressurized sand-damper. (Makris et al., 2021).

performance of the device. This device can be used in harsh environments with extremely high or low temperatures. Strain gauges are utilized to monitor the exerted output force from the sand damper, and they are inexpensive and reliable, while the nominal pressure can easily be adjusted with additional post-tensioning. Furthermore, this system is environmentally friendly and coincides with the current trends for sustainable engineering due to its stability and simplicity in its design (Makris et al., 2021). The pressurized sand damper (PSD) makes use of the pressure-dependent of the yielding sand strength and its effect on improving energy dissipation during cyclic motion. The PSD uses post-tensioned steel rod in addition to standard materials like sand and steel, serving as the modern philosophy of response modification (Makris et al., 2021).

The pressurized sand-damper was developed using dimensional analysis (Makris et al., 2021; Langhaar, 1962; Barenblatt et al., 1996; Makris and Black, 2003, 2004; Hardin and Drnevich, 1972). The velocity-independent shearing forces acting on the sphere moving over the sand that flows over the surface overpower the inertia forces of the sand grains when a pressurized sand-damper has finite dimensions (Makris et al., 2021). Velocity-independence indicates that there are friction (hysteretic) stresses present (Hardin and Drnevich, 1972). Thus, the resisting force on the moving sphere is the result of the projection along the direction of motion of the shearing strength. This strength is mobilized along the sand-steel interface as well as the passive normal stresses on the front of the moving sphere (Makris et al., 2021). Makris et al. (2021) describes the drag force on the moving sphere as being proportional to the pressure that is exerted and quadratic on the radius of the sphere. Experimentation can confirm by the dimensional analysis the quadratic dependence (Albert et al., 2001). Albert et al. (2001) states that the drag force is the result of jamming the grains. Jamming can be referred to as the formation of force chains along the compression direction of granular particles. The solid structure of the particles comes directly from loads being applied. When the force chains are formed, the shear stress will be supported indefinitely (Makris et al., 2021; Cates et al., 1998; Gates et al., 1999; Liu and Nagel, 1998). Cates et al. (1998) explains that when compression is along the force chain, jamming can sustain a static load (Makris et al., 2021). One example is when a structure is loaded any way other than the initial direction and the load-bearing capacity vanishes due to the collapse of the force chains, thus new ones are recreated along the new loading orientation for jamming to be

able to occur again (Makris et al., 2021).

The inelastic, fragile materials behave like a fixed principal axes (FPA) model (Cates et al., 1998; Gates et al., 1999). The pressurized sand-damper is not a fragile material in the model being designed because of the hydrostatic stress tensor that results from appreciable externally applied pressure (Makris et al., 2021). This can be described using the idealization of a yielding continuum. This is when the normal, or passive, and shear stresses along the sand-steel interface create drag on the moving sphere (Makris et al., 2021). Makris et al. (2021) analyzes the drag force on the sphere, which moves along the axis of the cylindrical damper housing. In this research, only single sphere-shaped was equipped in the pressurized sand-damper configurations are simulated, so it is unnecessary to analyze the dependence of the damper force on the ratio of the diameter of the pressurized sand damper cylinder to the radius of the sphere (D/R) in the Equation 4.2. The pressurized sand damper studied in this research affects energy dissipation due to the shear forces in the pressurized sand, which use the stress level-dependency of sand shear-strength, while also considering how the increase in dissipated energy impacts the system during cyclic motion.

This research project aims at examining a damping instrument that could be installed on members of structures to absorb shaking energy. The purpose of this work is to enhance high-performance structures using response modification devices. These devices display stable cyclic performance under extreme temperature conditions, are low-cost, capable of long-stroke demands, and use materials, like steel and sand, all while the force output can be monitored. The proposed pressurized sand-damper (PSD) meets all the above-mentioned

criteria and is also capable of being used as response modification for flexible buildings or the isolation systems of buildings with the isolation bearings. It also accompanies the buckling restrained braces for long-stroke demands as a sustainable response modification device with the use of materials like steel and sand. The discrete particulate nature of soils require discrete element method simulations to capture the micromechanics of soil behavior. The discrete element method (DEM) is useful for simulating and modeling movement of granular materials through the process of observing individual particle interactions and can be used to characterize energy dissipation mechanisms in cyclically loaded soils. The conducted DEM simulations employed the linear contact model and irregular-shaped particles. Being able to model the irregular particle shapes with a linear contact helped make the simulation more realistic. Therefore, the first objective of the research was to explore using irregular particles and linear contact to model pressurized sand damper under cyclic loads. Tracing energy components in the simulations is one advantage of utilizing Discrete Element Method.

In the performed series of DEM simulations, the effects of stroke amplitude and the magnitude of pressure imposed on the sand on the magnitude of cumulative dissipated energy were studied, in addition to different configurations of the pressurized sand damper that include differing sphere sizes, replacing the sphere with a box, changes in surface roughness of the sphere, and grain size. This research aimed to create a validated model that produces results in agreement with the experimentally measured behavior of the physical damper. The validation process included comparisons between DEM numerical experiments in a direct shear testing environment with physical direct shear testing on the same sand utilized in the

damper to ensure that the selected microscale properties in the simulations yield meaningful outcomes at the macroscale. A large number of simulations were performed that strategically identified the effect of the parameters that were considered in these work studies. Operating the sand damper with an enlarged sphere size, the force capacity of the pressured sand damper was increased. It was found that increasing the friction of the sphere had an insignificant impact on the piston capacity. When the range of grain sizes was increased from 2-4 mm to 1-5 mm in radius, the overall dissipated energy increased. In addition, the simulations went beyond those parameters mentioned above and investigated design configurations without the need to manufacture and test dampers of different scales. In this regard, the simulations present a cost-effective method compared to the manufacturing process. For instance, the configurations shown in Figure 3.7 and 3.8 were tested numerically for potentially improved performance over the basic system shown in 2.15. These configurations yielded in more efficient energy dissipation levels due to higher friction surface areas. The results presented in this work using DEM complement the experimental work by monitoring energy as well as stress tensors, and strain rate over time. In this study, DEM allows for the variation of parameters of interest without necessitating a new simulation model, demonstrating its vast capabilities as a tool to solve complex configurations.

Chapter 3

NUMERICAL SETUP AND METHODOLOGY

3.1. Introduction

Energy dissipation at the macroscopic level is the combination of individual mechanisms at the microscopic level. Research on these individual mechanisms highlight how frictional losses are the resulting factor of energy dissipation (Dobry and NG, 1992; Lai, 1998; Thevanayagam et al., 2003). Soil that is subjected to large seismic loads use these mechanisms, but they are not fully understood because of their complexity. Energy loss mechanisms can be grouped together and represented by damping mechanisms.

Microscale computational modeling assesses macroscale response mechanisms, like those involved in energy dissipation during cyclic loading of soils. The discrete element method (DEM) is an effective technique to model granular soils in the sand damper and there has been extensive engineering research conducted in the last few decades to confirm (Dobry and NG, 1992; Tsuji et al., 1993; Rajamani et al., 2000; El Shamy and Zeghal, 2005; El Shamy and Aydin, 2008). DEM is capable of testing theoretical hypotheses and response mechanisms for qualitative analysis and its simulations provide data on the microscale and macroscale levels, enabling a comprehensive assessment of the results. Simulations like this are capable of testing samples under various strain and frequency amplitudes with the same initial con-

ditions. In this research, DEM is used to investigate energy dissipation in the sand damper under cyclic loading.

3.1.1. Computational modeling

DEM offers users the ability to explore hypotheses about particle interactions and their macroscale response by implementing contact constitutive models to describe their interactions (O'Sullivan, 2011). At the macroscopic level, soil skeleton deformations reveal particles movements and show their complex material behavior. The movement of the particles as they slide, spin, and in the process form and break connections with surrounding particles is reflected in the deformations of the soil skeleton. This behavior exhibits pressure-dependency, permanent deformations, anisotropy, and localized instabilities. Discrete particles can capture the behavior of actual materials using simple assumptions and less input parameters at the micro-scale level (particle density, elastic modulus, Poisson's ratio, coefficient of friction, and coefficient of restitution) compared to the finite element method (FEM). The material becomes an unexpected property of the assembly due to the complexity of its behavior (Cundall, 2001). Previous 3-D DEM studies determined that particles were spherical, however, recent studies show how they actually have an irregular particle shape and how that impacts the soil behavior (Lim and Andrade, 2014; Vlahinić et al., 2017; Kawamoto et al., 2018).

This research has shown that DEM is the best technique for modeling the proposed sand damper where the particle dampers consist of an assemblage of discontinuous grains which can be modeled effectively as a collection of discrete particles. The DEM model is displayed in Figure 3.3 and it shows the configuration of the PSD, which can be found in Figure 3.6.

Particles of equal grain size distribution within the sand and the grain shapes resembling actual granular materials are used in the computational setup of this simulation. Figure 3.3, which contains approximately 70,000 particles, is modeled using PFC3D Version 6.0. This version is capable of parallel computing and can also generate the irregular shaped particles, as shown in Figure 3.3. The discrete element method is a mesh-free numerical technique (Cundall and Strack, 1979) which involves the motion of every particle in the simulation, while gravity is not taken into consideration in the partial motion. In this research, DEM has been used to model soil deposits. It is used to idealize the soil grains as rigid spherical bodies. If the grains are modeled as rigid spherical bodies, the computational cost and the complexities are reduced compared to modeling as irregular shaped particles. However, it must be considered that this simplification may produce a higher inaccuracy of the rotational inertia. When there is significant rotational inertia, it has been proven that there are major impacts that occur on the energy dissipation during the rotational movements and micromechanical behavior (Iwashita and Oda, 1998; Misra and Jiang, 1997; Bardet and Huang, 1992). Thus, irregularly-shaped blocks are the best representation of a soil deposit. Rigid blocks are being used to create non-spherical particles (Itasca, 2018).

3.1.1.1. Soil Grain as Irregular shape 3D Rigid Blocks

A rigid block is a closed, convex-shaped body composed of multiple triangular facets (polyhedra in 3-D). A rigid block assembly can exist in a domain. Inside the domain, rigid blocks can interact with other particles such as balls, clumps, walls, zones, and structural elements in 3-D. Each one of the rigid blocks is treated as a single body (unlike bodies that can exist of one or more pieces or clumps) which means there can only be one contact point between two rigid blocks or between a rigid block and a wall. The reduction of contact points is useful for performance and reduction of the simulation time. A rigid block is created from vertices. The irregular shape (non-sphericity) of these particles has advantage of eliminating the need for application of rolling friction, and therefore, the linear elastic contact model suffices to describe their interaction. The information of facet connectivity is kept to assist with contact detection and resolution. The process to determine if pieces collide is called contact detection, while the process to define the contact normal, gap and position is called contact resolution (Itasca, 2018). However, the contacts detection between rigid blocks is done using the Gilbert-Johnson-Keerthi (GJK) algorithm (Ong and Gilbert, 1997), which is an iterative scheme that uses Minkowski difference to find the overlapping particles. If two closed, convex bodies are in contact, the origin is located inside the constructed Minkowski difference between the two bodies. In order to determine the location of the contact for the rigid block, the contact location must be placed at the centroid of the overlapped volume in 3-D. For contacts between wall facets and rigid blocks, a point at the center of the facet is added to the collection of points used in the GJK algorithm. After detecting the overlaps, the

contact point located at the centroid of the overlap volume must be determined to compute the associated contact forces using the method presented by Shamos and Hoey (1976).

3.1.2. Mathematical Formulation and Constitutive Models

Particle motion can be specified by the transnational and rotational motion and determined by the resultant force and moment vectors acting on it. Position $\boldsymbol{X}$, velocity $\dot{\boldsymbol{X}}$, and acceleration $\ddot{\boldsymbol{X}}$ are the three expressions to describe the motion of the center of mass of the particle while angular velocity $\boldsymbol{\omega}$ and angular acceleration $\dot{\boldsymbol{\omega}}$ present the rotational motion of the particle.

The transnational equation of motion can be expressed in vector form as

$$\boldsymbol{F} = \boldsymbol{m}(\ddot{\boldsymbol{X}} - \boldsymbol{g}) \tag{3.1}$$

where:

$\boldsymbol{F}$ = denotes the resultant force,

m = denotes the particle mass,

$\ddot{\boldsymbol{X}}$ = represents the acceleration,

$\boldsymbol{g}$ = is the gravitational loading (e.g. the body force acceleration vector) .

This equation is solved using second order Velocity Verlet algorithem (Verlet, 1967). For example, if the previous cycle solved Equation 3.1 at time t and that the timestep resolved for the present cycle is $\boldsymbol{\Delta t}$. The 1/2 step velocity, $\dot{\boldsymbol{X}}^{(t+\Delta t/2)}$ can be calculated as

$$\dot{\boldsymbol{X}}^{(t+\Delta t/2)} = \dot{\boldsymbol{X}}^{(t)} + \frac{1}{2}\left[\frac{\boldsymbol{F}^{(t)}}{m} + \boldsymbol{g}\right]\boldsymbol{\Delta t} \tag{3.2}$$

The 1/2 step velocity is used in order to update the position at time $\boldsymbol{t+\Delta t}$ using the equation below:

$$\boldsymbol{X}^{(t+\Delta t/2)} = \boldsymbol{X}^{(t)} + \dot{\boldsymbol{X}}^{(t+\Delta t/2)}\boldsymbol{\Delta t} \tag{3.3}$$

The forces can be updated during the force displacement cycle point and this event leads to the updated acceleration $\ddot{\boldsymbol{X}}^{(t+\Delta t)}$. Thus, the updated velocity can be as

$$\dot{\boldsymbol{X}}^{(t+\Delta t/2)} = \dot{\boldsymbol{X}}^{(t+\Delta t/2)} + \frac{1}{2}\left[\frac{\boldsymbol{F}^{(t+\Delta t)}}{m} + \boldsymbol{g}\right]\boldsymbol{\Delta t} \tag{3.4}$$

The rigid body fundamental rotation equation is as shown below:

$$\boldsymbol{L}=\boldsymbol{I}\boldsymbol{\omega} \tag{3.5}$$

where:

$\boldsymbol{L}$ = is the angular momentum,

$\boldsymbol{I}$ = denotes the inertia tensor,

$\boldsymbol{\omega}$ = represents the angular velocity.

Equation 3.5 can be used to obtain the Euler's equation by taking the time derivative shown below:

$$\boldsymbol{M}=\dot{\boldsymbol{L}}=\boldsymbol{I}\dot{\boldsymbol{\omega}}+\boldsymbol{\omega}\times\boldsymbol{L} \tag{3.6}$$

$\boldsymbol{M}$ is the resultant moment acting on the rigid body. The relation refers to a local coordinate system that is attached to the center line of the body.

The 3D rotational motion for a rigid body has a full inertia tensor in the global coordinate system. It is a fourth-dimensional vector. Quaternions are the commonly utilized to describe the 3D rotations and orientations (Shoemake, 1985). Quaternions cannot affect the loss of a degree of freedom under certain conflagrations and its equation is shown as:

$$q = q_0 + q_i i + q_j j + q_k k = q_0 + \boldsymbol{q} \tag{3.7}$$

where:

$q_0 =$ denoted the scalar part,

$\boldsymbol{q} =$ the vector part,

$i, j, k =$ represents the basis elements.

$$i^2 = j^2 = k^2 = ijk = -1 \tag{3.8}$$

$$ij = k$$

$$jk = i$$

$$ki = j$$

Note that the product of two quaternions denote the Hamilton product which can be found using the distributive law the identities showed above. The vector notation can be as:

$$qp = p_0 q_0 - \boldsymbol{p}.\boldsymbol{q} + p_0\boldsymbol{q} + q_0\boldsymbol{p} + \boldsymbol{p} \times \boldsymbol{q} \tag{3.9}$$

The product of two quaternions is not commutative $qp \neq pq$ and this is because of the cross product. A pure vector quaternion with 0 scalar part (e.g. $\nu = \mathbf{0}+\boldsymbol{V}$) is created and performing the multiplication in Equation 3.9 occurs when the performing of the product of the vector V and a quaternion. The conjugate of the quaternion is describe in Equation 3.10 and the quaternion length is shown in Equation 3.11.

$$q^* = q_0 - \boldsymbol{q} \tag{3.10}$$

$$||q|| = q_0^2 + q_i^2 + q_j^2 + q_k^2 = qq^* = q^*q \tag{3.11}$$

A converted unit quaternion ($||q|| = 1$) can form as shown below in Equation 3.12 to a pure rotation matrix.

$$\nu^{'} = q\nu q^* \tag{3.12}$$

where:

$\nu^{'}$ = is the rotated vector,

q = the vector part,

i, j, k = represents the basis elements.

The sequential rotation q followed be the rotation p is given by the quaternion product pq, meaning that any number of rotations can by composed into a single quaternion and applied at once, provided they are unit quaternions. Properties of unity quaternions q and $-q$ represent the same rotation, the inverse rotation of q is the conjugate q^*, and the null rotation is q=1 where the vector part is $\mathbf{0}$.

Another algorithm was proposed in 2000 by Buss (2000) . These algorithms represent a different order to solve the rotational equations of motion described above. The proposed algorithms were all based on the Taylor-series expansion of angular velocity. This is a great procedure to supply more accurate estimates of the average angular velocity during timestep. Using the modified form of Equation 3.5 leads to calculating the angular velocity at time, t, see the equation below:

$$\boldsymbol{\omega}^{(t)} = \boldsymbol{I}^{(t)-1}\boldsymbol{L}^{(t)} \tag{3.13}$$

When rotating the principle moments of inertia by the rigid body orientation that is denoted with q_c, the inertia tensor (in the global coordinate axis) can be calculated 3.14.

$$\boldsymbol{I} = q_c \boldsymbol{J} q_c^* \tag{3.14}$$

$$\boldsymbol{I}^{-1} = q_c \boldsymbol{J}^{-1} q_c^*$$

By using Equation 3.7 and 3.14 the angular acceleration at time t can be

$$\dot{\boldsymbol{\omega}} = q_c^{(t)} \boldsymbol{J}^{(-1)} q_c^{(t)*} (\boldsymbol{M}^{(t)} - \omega^{(t)} \times \boldsymbol{L}^{(t)}) \tag{3.15}$$

The estimated average angular velocity over timestep is as follow

$$\bar{\boldsymbol{\omega}} = \boldsymbol{\omega}^{(t)} + \dot{\boldsymbol{\omega}}^{(t)} \frac{\boldsymbol{\Delta t}}{2} (\dot{\boldsymbol{\omega}}^{(t)} \times \boldsymbol{\omega}^{(t)}) \frac{\boldsymbol{\Delta t}^2}{12} \tag{3.16}$$

Equation 3.16 is utilized to update the orientation of rigid body $q_c^{(t+\Delta t^2)}$ by using the angular displacement, $\Theta = \bar{\boldsymbol{\omega}} \boldsymbol{\Delta t}$. and also converting the angular displacement to a unit quaternion and rotating q_c^t by this unit quaternion (Itasca, 2018).

$$q_c^{(t+\Delta t)} = \left(cos\left(\frac{\Theta}{2}\right) + sin\left(\frac{\Theta}{2}\right) \frac{\bar{\boldsymbol{\omega}}}{||\bar{\boldsymbol{\omega}}||} \right) q_c^{(t)} \tag{3.17}$$

After the rigid body orientation got updated, the new angular velocity $wt + \Delta t$ can be as follow:

$$\boldsymbol{\omega}^{(t+\Delta t)} = q_c^{(t+\Delta t)} \boldsymbol{J}^{(-1)} q_c^{(t+\Delta t)*} \boldsymbol{L}^t \tag{3.18}$$

The fourth-order solution shows that the time derivative of the quaternion as given in Equation 3.19

$$\dot{q_c} = \frac{1}{2}\varpi q_c \tag{3.19}$$

Where ϖ here is the pure vector component with vector component ω. By substituting Equations 3.13 and 3.14 into 3.19, Equation 3.20 form as:

$$\dot{q_c} = \frac{1}{2}(q_c \boldsymbol{J}^{(-1)} q_c^* \boldsymbol{L}^{(t)}) q_c \tag{3.20}$$

When applying the standard fourth-order Runge-Kutta method in Equation 3.20 , the orientation at time $t + \Delta t$ can be as shown in Equation 3.21 below (Itasca, 2018):

$$q_c^{(t+\Delta t)} = q_c^{(t)} + \frac{\Delta t}{6}(k_1 + 2k_2 + 2k_3 + k_4) \tag{3.21}$$

The quaternion k_1 is as given:

$$k_1 = \frac{1}{2}(q_c^{(t)} J^{(-1)} q_c^{(t)*} L^{(t)}) q_c^{(t)} \tag{3.22}$$

In order to come up the value of k_2 3.24, an intermediate step should be performed as shown in Equation 3.23.

$$q_{c1} = q_c^{(t)} + k_1 \frac{\Delta t}{2} \tag{3.23}$$

$$k_2 = \frac{1}{2}(q_{c1} \boldsymbol{J}^{(-1)} q_{c1}^* \boldsymbol{L}^{(t)}) q_{c1} \tag{3.24}$$

The following intermediate value of the orientation quaternion q_{c2} 3.25 can be obtained after the finding of k_3 3.26 and the final value of the orientation quaternion q_{c3} 3.27 is found after calculating the quaternion k_4 3.28. Finally, Equation 3.18 is utilized when the 3D rigid body got updated as well as the angular velocity to time $\boldsymbol{t+\Delta t}$. This mode is the same as the one presented in 2008 by Johnson et al. (2008)

$$q_{c2} = q_c^{(t)} + k_2 \frac{\Delta t}{2} \tag{3.25}$$

$$k_3 = \frac{1}{2}(q_{c2}\boldsymbol{J}^{(-1)}q_{c2}^{*}\boldsymbol{L}^{(t)})q_{c2} \tag{3.26}$$

$$q_{c3} = q_c^{(t)} + k_3 \Delta t \tag{3.27}$$

$$k_4 = \frac{1}{2}(q_{c3}\boldsymbol{J}^{(-1)}q_{c3}^{*}\boldsymbol{L}^{(t)})q_{c3} \tag{3.28}$$

Particle motion can be specified by the translational and rotational motion. The motion of a particle, p, can be expressed by the momentum equations:

$$m_p \ddot{\mathbf{u}}_p = \sum_{c=1}^{N_c} \mathbf{f}_c \tag{3.29}$$

$$I_p \ddot{\boldsymbol{\theta}}_p = \sum_{c=1}^{N_c} \mathbf{r}_c \times \mathbf{f}_c \tag{3.30}$$

where $\ddot{\mathbf{u}}_p$ and $\ddot{\boldsymbol{\theta}}_p$ are translational and rotational acceleration vectors, m_p is particle mass, I_p is particle moment of inertia, N_c is the total number of contacts, f_c refers to inter-particle force at contact c, and r_c is vector connecting the center of the particle to the location of the contact, c.

In DEM, particles are assumed to be rigid but can overlap. The amount of this overlap is dictated by a contact force model. A contact force, $\mathbf{f}_c$, between two particles consists of normal, $\mathbf{f}_{cn}$, and shear, $\mathbf{f}_{cs}$, components (Itasca, 2018). The normal component was idealized using a linear spring model connected in parallel with a viscous dashpot that is shown in Figure 3.1:

The contact normal force is described by:

$$\mathbf{f}_{cn} = \mathbf{f}_n + \mathbf{f}_{dn} \tag{3.31}$$

in which $\mathbf{f}_n$ is the vector of normal spring contact forces and $\mathbf{f}_{dn}$ is the vector of damping forces given by:

$$\mathbf{f}_n = k_n u_n \mathbf{n} \tag{3.32}$$

$$\mathbf{f}_{dn} = c_n v_n \mathbf{n} \tag{3.33}$$

where u_n and v_n are, respectively, relative displacement and velocity at the contact along the line connecting the particle centers, $\mathbf{n}$ is unit normal vector at the contact, k_n is normal

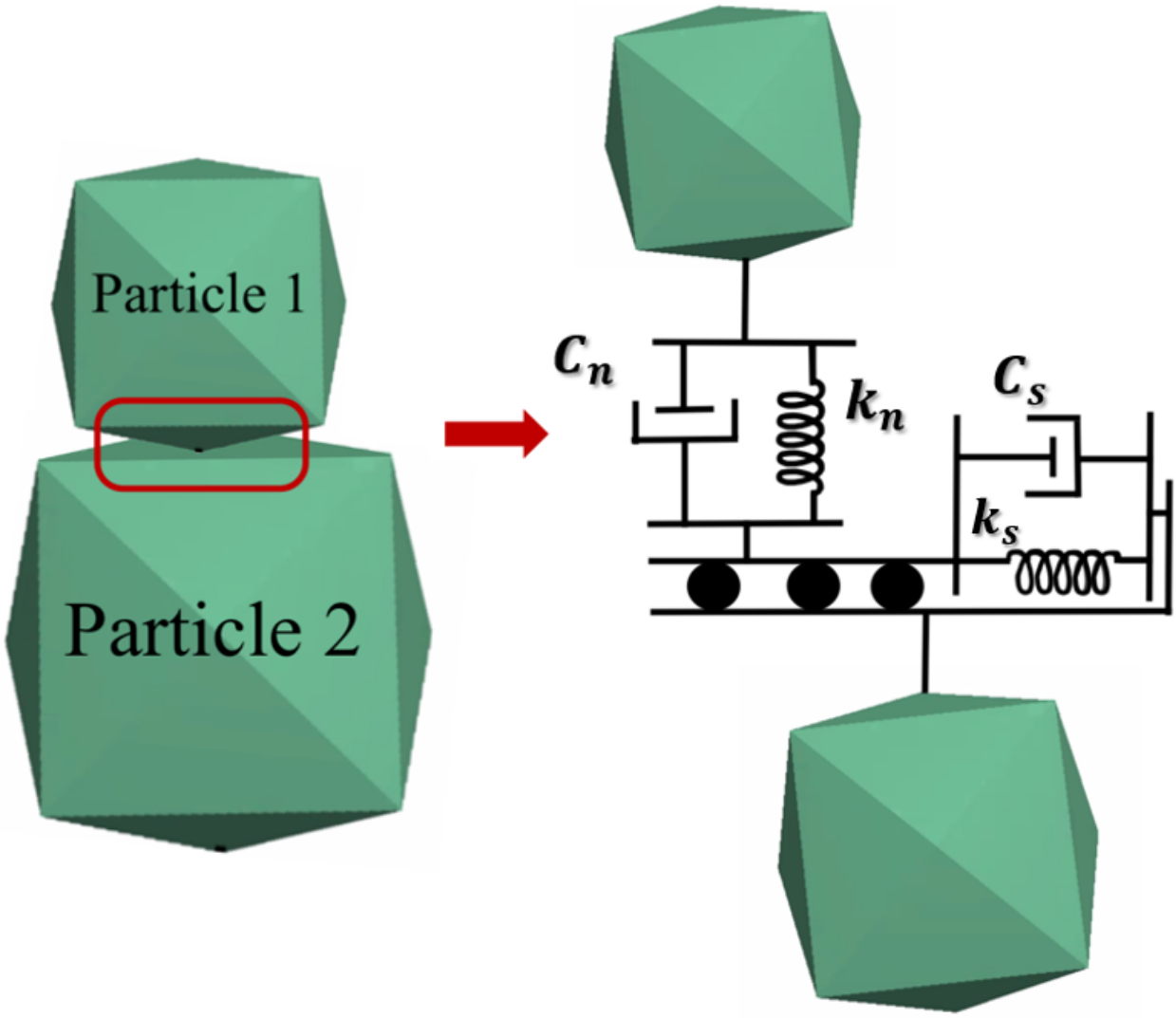

Figure 3.1. Schematic of the constitutive law of normal and shear contact forces between two particles.

contact stiffness, and c_n is the normal viscous damping coefficient. The incremental shear contact force, $d\mathbf{f}_{cs}$, was modeled using an elastic spring in series with a frictional slider:

$$d\mathbf{f}_{cs} = d\mathbf{f}_s + d\mathbf{f}_{ds} \tag{3.34}$$

in which $d\mathbf{f}_s$ is vector of incremental shear spring contact forces and $d\mathbf{f}_{ds}$ is vector of damping forces in the shear direction given by:

$$d\mathbf{f}_s = k_s d\mathbf{u}_s \tag{3.35}$$

$$d\mathbf{f}_{ds} = c_s d\mathbf{v}_s \tag{3.36}$$

where $d\mathbf{u}_s$ and $d\mathbf{v}_s$ are incremental shear displacement and velocity vectors at the contact, c_s is shear viscous damping coefficient, and k_s is shear contact stiffness. A slip Coulomb model (Itasca, 2018) is used to connect the shear and normal forces, such that $F_s \leq \mu F_n$. F_s and F_n are the resultant shear and normal forces at the contact, respectively. The Coulomb friction coefficient is denoted as the Greek letter (μ). Once the total shear force in the spring and dashpot exceeds the limiting value, the frictional slider assumes control of the response in the shear direction, as shown in Figure 3.1.

Each particle's motion is estimated using an explicit time integration approach that assumes that the change in velocities and accelerations during an incremental time step is small enough that they can be presumed constant within that time step. The interaction

between particles is tracked during a calculation cycle, and the contact forces are modified depending on the contact laws. To acquire new particle positions, the particle equations of motion are then integrated. As a result, new contacts are established in each time step, while existing contacts are removed as applicable.

3.2. Energy Calculation

The discrete element method was utilized to characterize energy dissipation mechanisms in cyclically loaded soils (sand) based on micromechanical considerations. Computational simulations are carried out to investigate the energy dissipation mechanism on the sand damper and reveal that monitoring the particle energy components has a powerful benefit in describing the dissipated energy. This is one advantage of the DEM approach. The different components of microscale energies were monitored during the course of the simulations and characterized into input and dissipated energies. Monitoring the particle energies enhanced the understanding of the particle interaction at the microscale level where it can supply the means to understand the response mechanism. One advantage of monitoring an individual energy component is that it informs energy conservation and determines the contribution of each energy term to the total dissipated energy. The energies that are considered in this work include friction, kinetic, boundary, strain, and viscous damping energies.

The total accumulated work E_w refers to the boundary work (e.g. wall work). The work done by all walls in the assembly is as follow:

$$E_w = \sum_{t=0}^{t} \sum_{w=1}^{N_w} \mathbf{f}_w^T d\mathbf{u}_w + \mathbf{m}_w^T d\boldsymbol{\theta}_w \tag{3.37}$$

where N_w is the number of walls, $\mathbf{f}_w$ is the resultant force acting on the wall, du_w denotes to the incremental translational displacement vector of the wall, $\mathbf{m}_w$ refers to the resultant moment acting on the wall, and $d\boldsymbol{\theta}_w$ denotes the incremental rotational displacement vector of the wall.

The total kinetic energy E_k accounts for both translational and rotational motion of all particles and can be written as:

$$E_k = \frac{1}{2} \sum_{t=0}^{t} \sum_{p=1}^{N_p} m_p \dot{\mathbf{u}}_p^2 + I_p \dot{\boldsymbol{\theta}}_p^2 \tag{3.38}$$

where $\dot{\mathbf{u}}_p$ and $\dot{\boldsymbol{\theta}}_p$ are the translational and rotational velocity vectors, and I_p is particle moment of inertia.

Strain energy is related to the deformation of the particles. When deformation occurs, the particle tends to revert back to its original shape. The total strain energy E_s, stored at all contacts of the entire assembly can be described as follows:

$$E_s = \frac{1}{2} \sum_{c=1}^{N_c} \frac{\mathbf{f}_n^2}{k_n} + \frac{\mathbf{f}_s^2}{k_s} \tag{3.39}$$

where N_c is the number of contacts at contact c, $\mathbf{f}_n$, $\mathbf{f}_s$, and k_n, k_s are the vector of normal spring contact force, the vector of shear spring contact force, normal contact stiffness, and shear contact stiffness, respectively.

The total fictional work, donated by E_f, is the dissipated energy by fictional sliding at all contacts:

$$E_f = \sum_{t=0}^{t} \sum_{c=1}^{N_c} \mathbf{f}_s^T d\mathbf{u}_{slip} \tag{3.40}$$

where N_c is the number of contacts at time, t, and $\mathbf{f}_s^T$ and $\mathbf{d}u_{slip}$, are the average shear force and the increment of slip displacement, respectively, at the contact force of the current

timestep.

The total viscous damping energy, E_d, due to particle-to-particle and particle-to-wall impacts at all contacts:

$$\boldsymbol{E_d = \sum_{t=0}^{t} \sum_{c=1}^{N_c} \mathbf{f}_d.(\dot{\delta} \Delta t)} \tag{3.41}$$

Where $\mathbf{f}_d$ is the total dashpot forces in normal and shear, $\mathbf{f}_d$=($\mathbf{f}_{dn}$ + $\mathbf{f}_{ds}$), and $\dot{\delta}$ is the relative translational velocity, $\dot{\delta} = \dot{\delta}_n + \dot{\delta}_s$, $\dot{\delta}_n$ and $\dot{\delta}_s$, are the relative translational velocities normal and tangential, respectively, to the contact plane, and the subscripts n and s correspond with normal and shear action, respectively.

The DEM-based commercial software PFC3D version 6.00.29 was used for all simulations in this work (Itasca). Within PFC3D, the energy given by Equations 3.37 to 3.41 were monitored.

3.3. Modeling of Energy Dissipation in PSD Using Discrete Element Method

3.3.1. 3-D Discrete Element Model Features

In the presented studies, all the analyses were conducted utilizing the software PFC3D (Itasca, 2018), which is a discrete element simulation environment software. This software uses a high performance computing technique. In this research, there were several model configurations performed and studied by considering sensitivity analyses with respect to different base-case model simulations of energy dissipation in the sand damper equipped with

a single sphere, double sphere, a single enlarged sphere, and a roughened surface sphere. Prototypes of the sand damper are shown in Figures 3.6, 3.7, 3.8, and 3.9. The applied particles are irregular shapes of rigid bodies and all models were user controlled (e.g. the contact model, calculation cycle order, and timestep magnitude). The dry sand was represented by irregular shape sizes ranging from 2 mm to 4 mm and 1 mm to 5 mm. These irregular particle shapes were utilized to simulate energy dissipation mechanics of the sand damper in the 3-D simulation. The particles and facet (i.e. wall) frictions are set to be 0.5 and 0.15, respectively. Linear contact is established between rigid blocks as well as between the rigid block and a facet. The shear and normal stiffnesses are 1e7 N/m for the particle and 1e8 N/m for the wall. The piston velocity is represented by:

$$v(t) = \omega \; u_0 \; cos(\omega \; t) \tag{3.42}$$

where ω is the loading frequency given by

$$\omega = 2 \; \pi \; f_0 \tag{3.43}$$

The frequency $f_0 = 20 \; Hz$, and the amplitude u_0 has values of 4 and 6 cm. The pressure level p has values of 1.0, 2.0, 3.0, 4.0 and 5.0 MPa. The sand solid density is 2660 kg/m^3. Figures 3.3, 3.4, and 3.5 describe the features of a typical model utilized in the study, which is equipped with different sphere configurations and focuses on the pressurized sand. In all conducted cases, the sand damper was simulated with a linear entity in which the sphere

can move freely in in one direction (i.e. y-direction) to accomplish the desired amplitude at the required pressure levels (p= 1.0, 2.0, 3.0, 4.0 and 5.0 MPa) during the simulation time.

In the first model, the sphere is placed in the center of the metal rod and at distance of ± 120 mm to the rod center in the second model. In the remaining models, the sphere is established in the origin of the metal rod (the origin is located at the center of the rod). The recorded piston force (i.e. when the sphere is passing through the origin and at its the peak velocity during its harmonic motion) is proof that the force increases as the displacement increases at each assigned pressure level. Kinetic, boundary, friction, dashpot, strain, and slip energy are monitored throughout the simulation. The duration of the considered studies ranged between 20 and 25 days and were computed with a high tower workstation which has dual Intl(R) Xeon(R) CPU E5-2687W v3 @ 3.10 GHz processors and 128 GB of memory rams.

3.3.2. The Simulated Configurations

The dimensions of the sand damper and the characteristics of the utilized sand assembly considered in this study are selected to mimic the behavior of energy dissipation in the experimental cyclic loading configuration. The DEM models of the sand damper utilized in this research are shown in Figures 3.3, 3.4, 3.5. The particle shape can be shown in Figure 3.2. The grain size distribution varies in range from 2 mm to 4 mm, and 1 mm to 5 mm.

In this research, various sand damper configurations and parametric studies investigated the behavior of the pressurized sand damper by evaluating the energy dissipation in the sand damper. These configurations include a single, double, triple, and enlarged spheres in

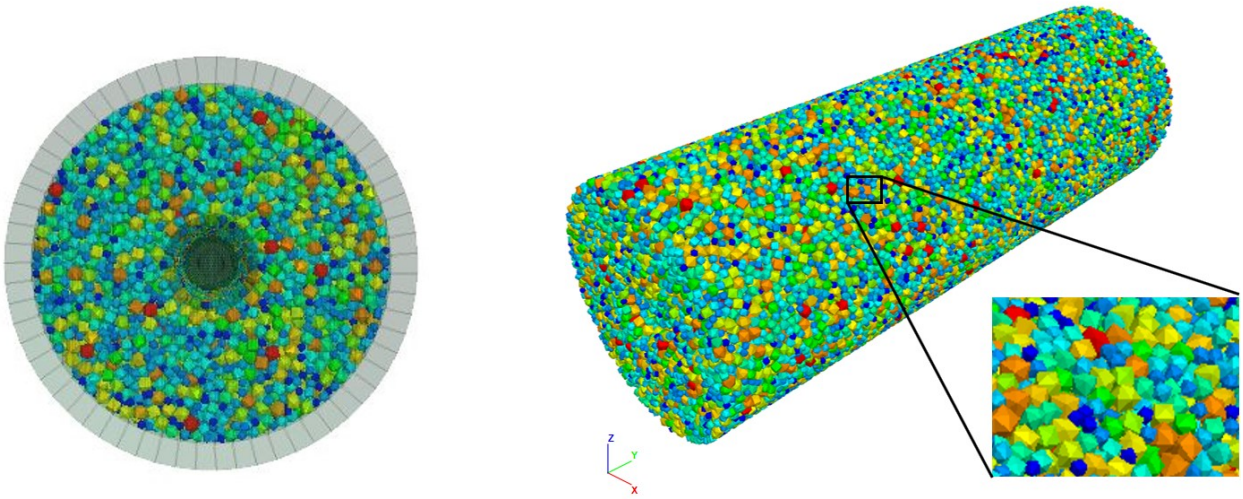

Figure 3.2. Particle shape characterizing the PSD.

the sand damper. For instance, the first PSD model considered in this paper was equipped only with a single sphere piston configuration. Figure 3.3 shows the proposed configuration of the pressurized sand damper that was tested numerically in DEM simulations while the second model has two spheres (see Figure 3.4). The third model consists of three spheres inside the pressurized sand damper. These spheres have the same diameter of 6 cm. Its simulated configuration can be seen in Figure 3.5. These three proposed models all have the same sphere diameter of 6 cm. The fourth model increases the sand damper sphere radius. The ratio of the diameter to the cylinder radius is D/R= 5.696 for the fourth model (see Figure 3.9). Another DEM model was conducted numerically by considering an increase in the friction of the metal sphere. In this case, the friction coefficient was increased from 0.15 to 0.9 to study the effect of surface roughness of the sphere. This case is conducted when the sand damper is equipped with a single sphere with the sphere size shown in Figure 3.6.

3.3.3. Simulated Geometry

Figure 3.6 shows the simulated geometry for the pressurized sand damper with a single sphere. The length and the diameter of the PSD are 62 cm and 18.9 cm, respectively. The rod on which the sphere is attached has a length of 165 cm, and its diameter is 4 cm. The sphere radius in this case is 3 cm. Figures 3.7 and 3.8 show the schematic configurations of the PSD utilizing the same dimensions as mentioned in Figure 3.6. Another geometric design case can be seen in Figure 3.9 where the sphere is attached at the center of the rod with a different size. The attached sphere has a radius which is 33.18 cm.

3.3.4. Material Properties

The considered properties of the utilized pressurized sand damper in these studies for each case at varying pressure levels, displacement amplitudes, and piston configurations can be found in Table 4.1 listed below. For example, the deposit porosity n, density ρ, the pressure p, and shear stiffness of the soil deposit and walls k_s, normal stiffness of the soil deposit and walls k_n, and friction coefficient μ are shown. Their values are also summarized in following Tables 4.1, 3.2, and 3.3.

3.4. Simulations

The numerical model can be seen in Figure 3.2. Following the generation of the sample, a servo-mechanism was applied iteratively to isotropically consolidate the specimen to the desired confining stress. The servo-mechanism uses the feedback of the stresses on the walls

Table 3.1. DEM simulation parameters for trials 1,2, and 3.

	Simulation (1)	Simulation (2)	Simulation (3)
Amplitude	40 (mm)	60 (mm)	40 (mm)
Frequency (f)	20 HZ	20 HZ	20 HZ
Pressure magnitude	1 MPa	1 MPa	2 MPa
Configuration	one sphere	one sphere	one sphere
porosity	0.40	0.40	0.40
Particle solid density	2660 kg/m^3	2660 kg/m^3	2660 kg/m^3
Particle size (Radius)	(2-4) mm	(2-4) mm	(2-4) mm
Number of particle	70,000	70,000	70,000
Wall normal stiffness	1e8 N/m	1e8 N/m	1e8 N/m
Wall shear stiffness	1e8 N/m	1e8 N/m	1e8 N/m
Particle normal stiffness	1e7 N/m	1e7 N/m	1e7 N/m
Particle shear stiffness	1e7 N/m	1e7 N/m	1e7 N/m
Wall coefficient friction	0.15	0.15	0.15
Particle coefficient friction	0.5	0.5	0.5
Normal viscous damping ratio	0.1	0.1	0.1
Shear viscous damping ratio	0.1	0.1	0.1

Table 3.2. DEM simulation parameters for trials 4,5, and 6.

	Simulation (4)	Simulation (5)	Simulation (6)
Amplitude	60 (mm)	40 (mm)	40 (mm)
Frequency (f)	20 HZ	20 HZ	20 HZ
Pressure magnitude	2 MPa	3 MPa	4 MPa
Configuration	one sphere	one sphere	one sphere
porosity	0.40	0.40	0.40
Particle solid density	2660 kg/m^3	2660 kg/m^3	2660 kg/m^3
Particle size (Radius)	(2-4) mm	(2-4) mm	(2-4) mm
Number of particle	70,000	70,000	70,000
Wall normal stiffness	1e8 N/m	1e8 N/m	1e8 N/m
Wall shear stiffness	1e8 N/m	1e8 N/m	1e8 N/m
Particle normal stiffness	1e7 N/m	1e7 N/m	1e7 N/m
Particle shear stiffness	1e7 N/m	1e7 N/m	1e7 N/m
Wall coefficient friction	0.15	0.15	0.15
Particle coefficient friction	0.5	0.5	0.5
Normal viscous damping ratio	0.1	0.1	0.1
Shear viscous damping ratio	0.1	0.1	0.1

Table 3.3. DEM simulation parameters for trials 7,8, and 9.

	Simulation (7)	Simulation (8)	Simulation (9)
Amplitude	60 (mm)	40 (mm)	60 (mm)
Frequency (f)	20 HZ	20 HZ	20 HZ
Pressure magnitude	4 MPa	5 MPa	5 MPa
Configuration	one sphere	one sphere	one sphere
porosity	0.40	0.40	0.40
Particle solid density	2660 kg/m^3	2660 kg/m^3	2660 kg/m^3
Particle size (Radius)	(2-4) mm	(2-4) mm	(2-4) mm
Number of particle	70,000	70,000	70,000
Wall normal stiffness	1e8 N/m	1e8 N/m	1e8 N/m
Wall shear stiffness	1e8 N/m	1e8 N/m	1e8 N/m
Particle normal stiffness	1e7 N/m	1e7 N/m	1e7 N/m
Particle shear stiffness	1e7 N/m	1e7 N/m	1e7 N/m
Wall coefficient friction	0.15	0.15	0.15
Particle coefficient friction	0.5	0.5	0.5
Normal viscous damping ratio	0.1	0.1	0.1
Shear viscous damping ratio	0.1	0.1	0.1

The above Tables [4.1, 3.2, 3.3] present the simulation parameters for the trials from 1 to 9. However, this tables herein manifest different parameters utilized for the sand damper equipped with a single piston configuration.

to determine if the isotropic stress is more or less than the desired value and adjusts the wall positions accordingly (Itasca, 2018). During this stage, a specific prescribed pressure is reached by adjusting the wall position of the sand damper. In this study, the results of samples packed at initial porosity of 40%. The particle properties that were considered in these simulations can be seen in the Table 4.1. The final step of the simulation that followed the servo-mechanism is the piston loading with varying stroke amplitudes and frequencies. A sinusoidal motion is applied for loading the damper. In contrast to the laboratory testing, the numerical simulations make it easy to repeat a test on the exact same sample, changing one parameter at a time without changing the initial conditions of the sample. The measurement sphere is created with radius of 35.5 mm at a distance of 150 mm in the y-direction and at varying positions in x-direction stress and strain components developed in the sand inside the damper were monitored using averaging volumes (spheres) positioned at different locations in the damper. and z-direction from the center of the rod. Figure 3.10 shows the location of the measurements sphere that were employed inside the sand damper where its main purpose is to measure porosity, and components of the stress tensor throughout the simulation (Itasca, 2018). The horizontal stresses computed inside the measurement spheres were almost identical to those computed from the walls. A code was developed to monitor energy components during the course of the simulation for the entire sample.

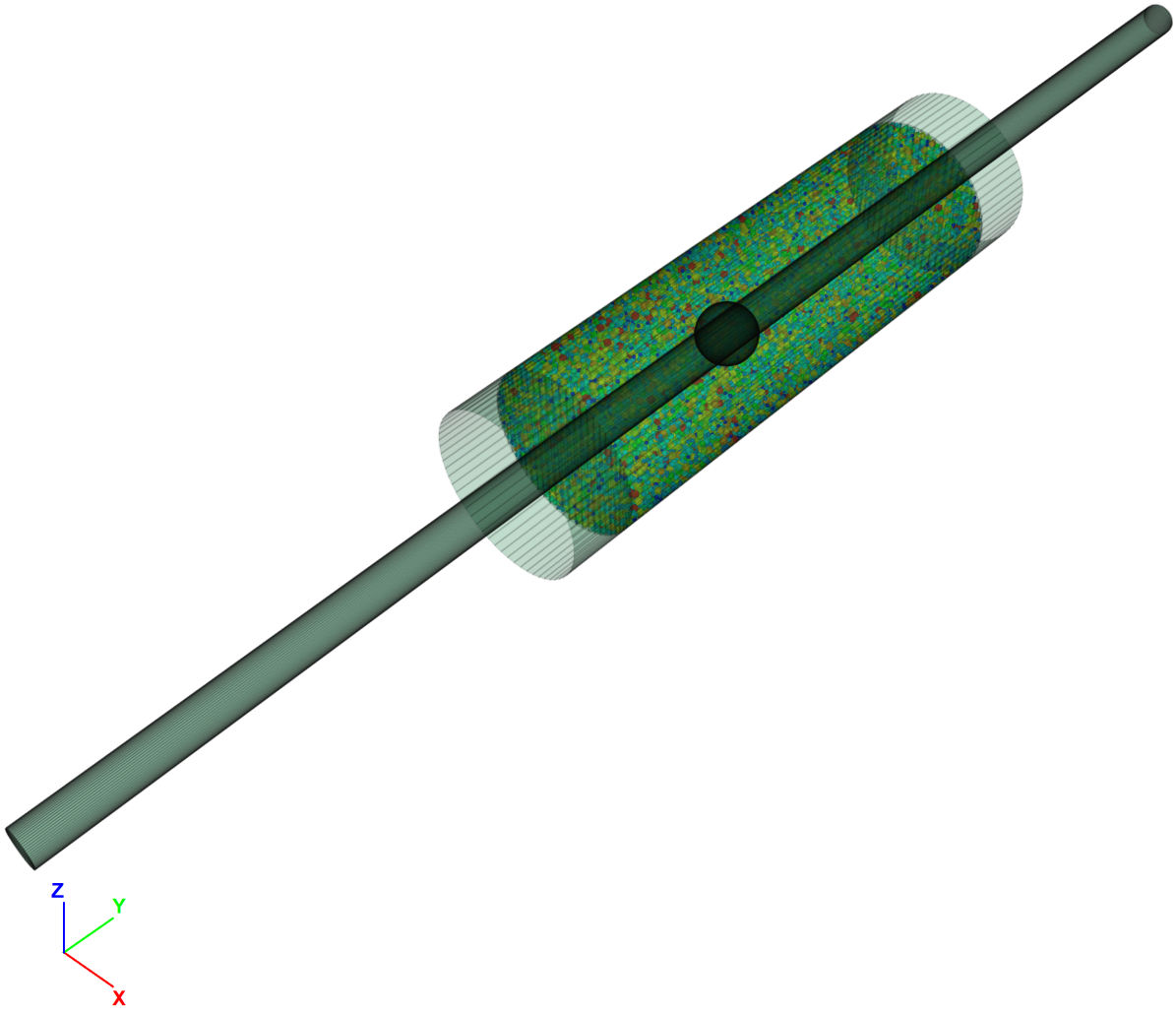

Figure 3.3. Generated DEM model of the proposed pressurized sand damper equipped with a single sphere at the center of the rod.

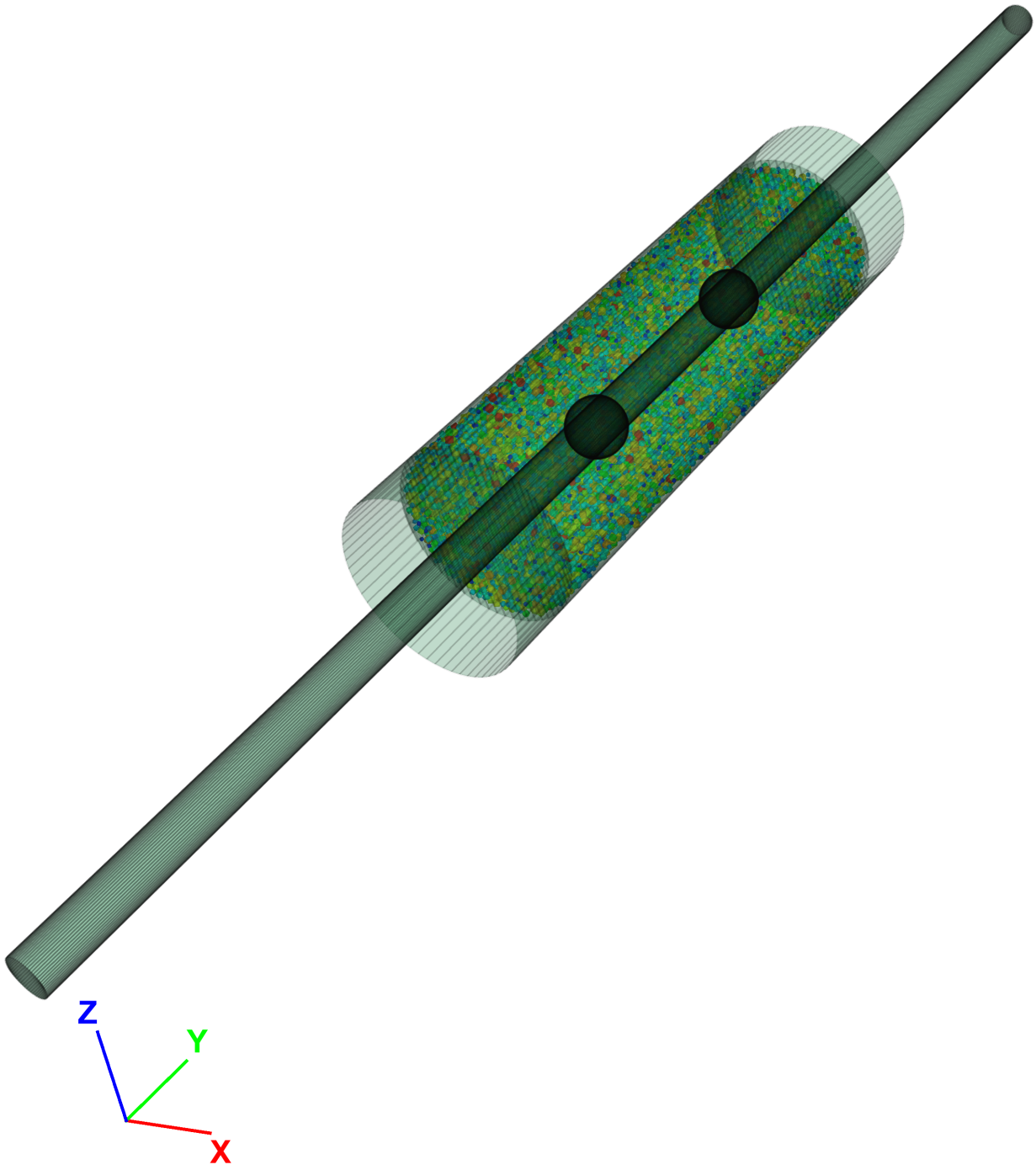

Figure 3.4. The DEM model for the pressurized sand damper which is equipped with two metal spheres appended on the piston rod.

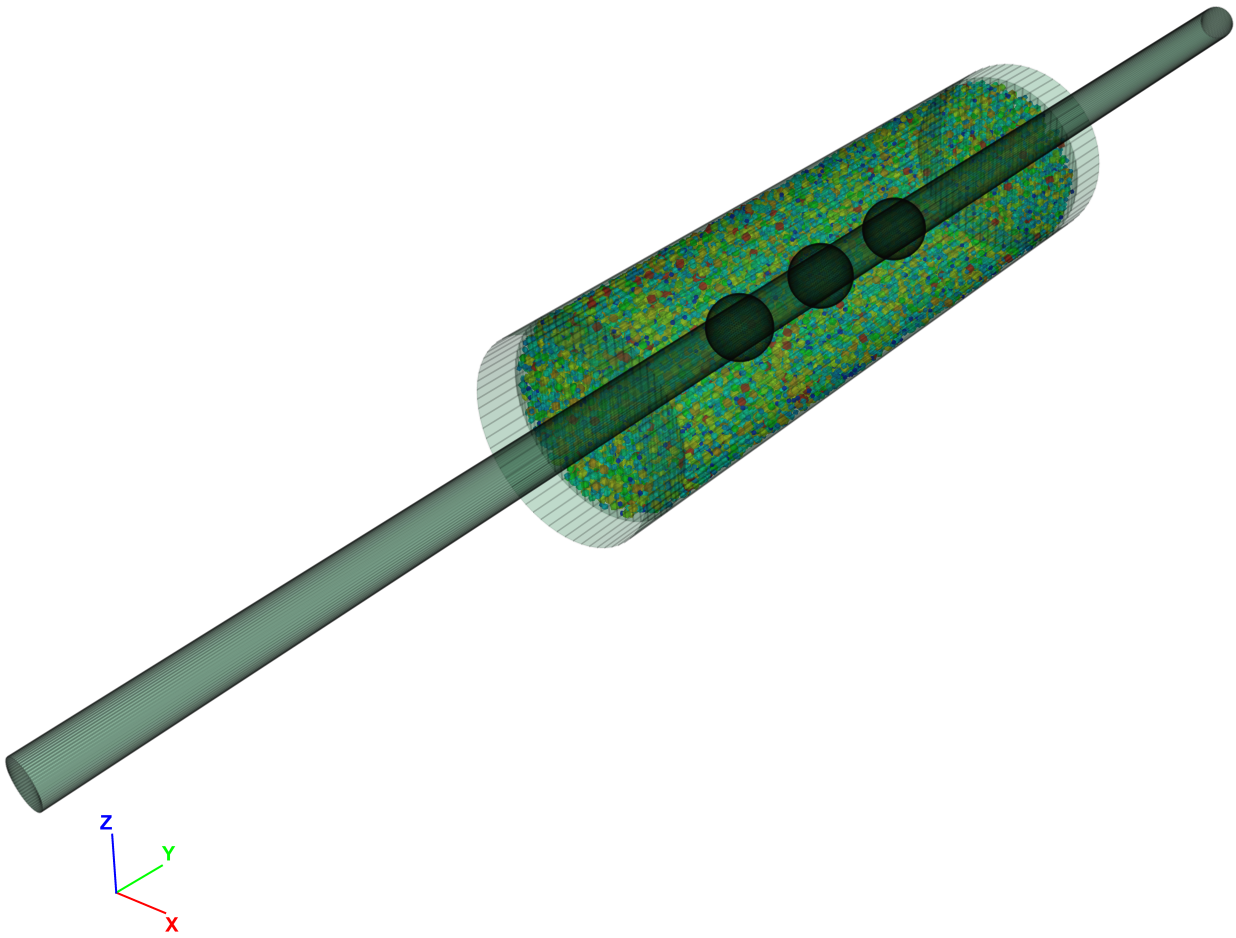

Figure 3.5. Generated DEM model of the proposed pressurized sand damper equipped with three metal spheres.

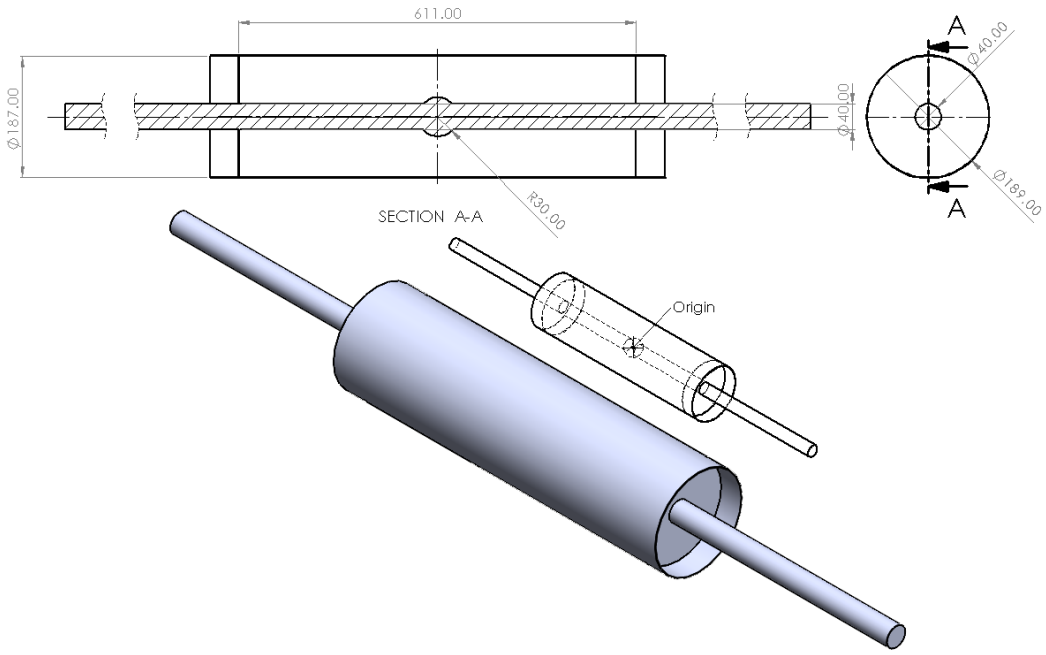

Figure 3.6. The simulated geometry of the pressurized sand damper model equipped with one sphere at the center of the metal rod.

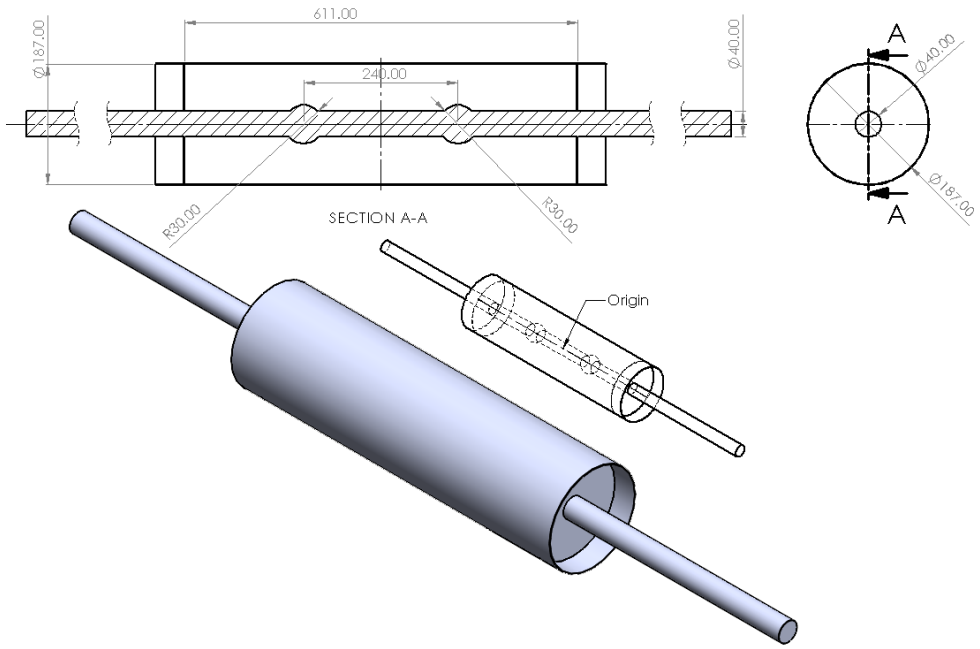

Figure 3.7. Schematic design of sand damper model equipped with two spheres.

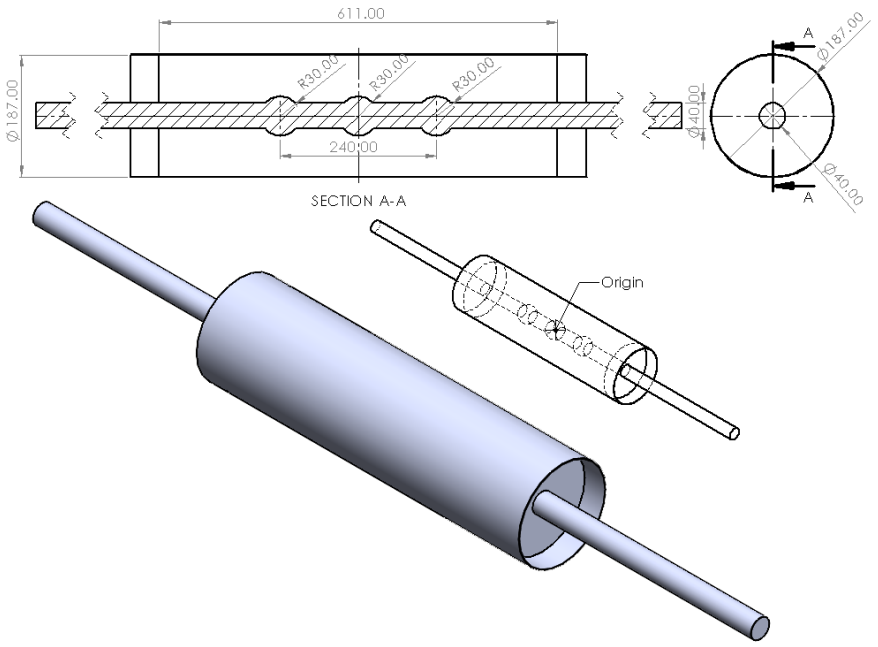

Figure 3.8. Schematic design of sand damper model equipped with three spheres.

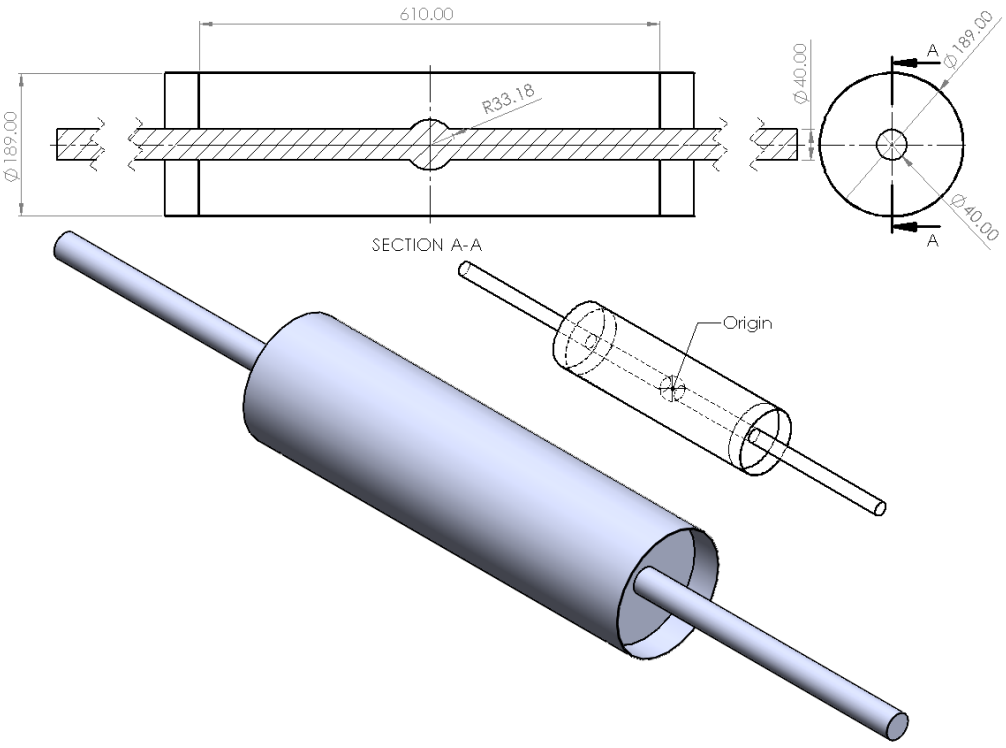

Figure 3.9. Schematic of sand damper model equipped with an enlarged single sphere of radius 33.18 mm.

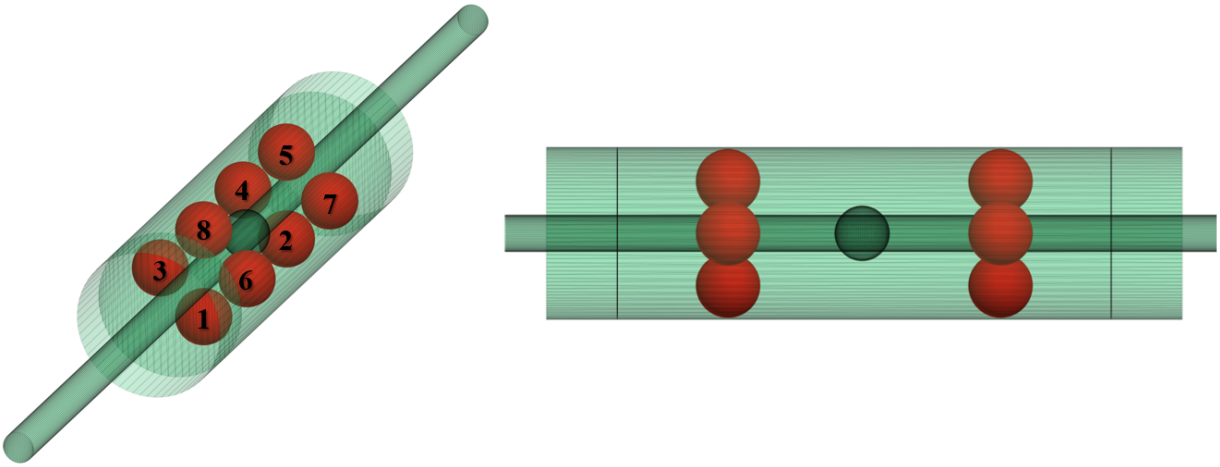

Figure 3.10. The measurements spheres inside the sand damper model equipped with one sphere.

Chapter 4

VALIDATION RESULTS

4.1. Experimental Study of Sand Damper Energy Dissipation to Validate the Numerical Studies

The study conducted by Makris et al. (2021) in 2020 approximated the nonlinear hysteretic behavior of the proposed pressurized sand damper of the Structures Laboratory in the University of Patras, Greece (Makris et al., 2021). This study used dimensional analysis, a mathematical tool which expands on the general forms of the relation that was developed by (Langhaar, 1962; Barenblatt et al., 1996; Makris and Black, 2003, 2004). The schematic model of the sand damper is shown in Figure 2.15.

To develop a quantitative illustration of the energy dissipation mechanism in the pressurized sand damper under the mechanical loads, the following assumptions were made (Makris et al., 2021):

- The experimental test uses a steel sphere of radius, R.
- The sphere moves with a constant velocity, v.
- The gravity loading is neglected in the tests.
- A sufficiently large enclosed sand medium is pressurized with a pressure p at the end gates of the cylinder over the direction of sphere motion.

- The surface contact of sphere while moving in the direction of the harmonic motion and sand grain flowing around its surface causes the shearing force.
- The density of the sand is not related to the resistance (drag) exerted on the moving sphere.
- The exerted shear stresses by the sand grains on the steel sphere are nearly velocity-independent, i.e. they are friction (hysteretic) stresses. The developed shearing strength on the front of the moving sphere in the direction of motion is called the resisting force, which acts along the sand-steel interface and the passive normal stresses.

Equation 4.1 shows the drag mechanism as a function of the exerted pressure, p, along the direction of motion and the radius of the sphere, R.

$$F_s = f(p, R) = \Pi_s p R^2 \tag{4.1}$$

Where R is the radius of the sphere, p is the exerted pressure, and Π_s denotes a dimensionless coefficient. Π_s accounts for the spherical geometry, the Poisson effect that controls the level on normal stresses along the direction that the pressure p is exerted (against the direction of motion), and the developed mobilized normal and shear stresses from the projections on the sand-sphere interface along the direction of motion of the sphere. According to Equation 4.1, F_s is proportional to the exerted pressure p and is quadratically related to the radius of the sphere, R. Dimensional analysis was employed for the quadratic dependence of the drag force, F_s, on the radius of the sphere, R, which, was proven in an experimental study by Albert et al. (2001).

According the study were conducted by Albert et al. (2001), drag force on the sphere is the

result of jamming of the grains. Jamming is recognized as the figuration of force chain in the literature of physics (Cates et al., 1998; Gates et al., 1999; Liu and Nagel, 1998) throughout the granular particles compression direction whose unsettled solid structure stems directly from the applied loading. When creating a single array of the force chains, a shear stress will be supported indefinitely. Other studies carried out in 1998 and 1999 by Cates et al. (1998) and Gates et al. (1999) found that as long as the compression is sustained on the direction of the force chain, jamming may sustain a static load.

When jamming occurs for a structure that is loaded at a certain direction, the jammed structure load-bearing capacity will vanish due to the collapse of the force chain. Thus, another new jammed structure should be initiated for the new loading direction for the loose materials. The materials used in this study are not elastic materials due to their ability to transmit elastic waves (i.e. being described with an elastic shear modulus, G, and a Poisson ratio, ν) and the inability to elastically support some infinitesimal load along any direction other than the direction of the force chains. This kind of material is made (coined) by stamping metal "fragile materials". According to Cates et al (Cates et al., 1998; Gates et al., 1999), their behavior can be characterized with a "fixed principal axes" (FPA) model (Makris et al., 2021). The configuration (Makris et al., 2021) of the pressurized sand damper is shown in Figure 2.15. The sand damper is characterized by a single sphere with radius R = 3 cm attached to the piston rod with radius of 2 cm and is moving within the finite domain of the cylindrical damper housing with diameter D = 18.9 cm and length L = 62 cm. The resisting force on the sphere also depends on the displacement of the sphere (stroke of

the damper), u and on the gap (clearance) between the sphere and the cylindrical housing, $D-2R$. Following a similar reasoning, the resisting (drag) force on the sphere moving along the axis of the cylindrical damper housing of diameter D is expressed as:

$$F_d = f(p, R, u, D) = \Pi_s p R^2 \Phi \left(\frac{u}{R}, \frac{D}{R} \right) \tag{4.2}$$

where $p = 4F/(\Pi D^2)$ is the pressure along the direction of motion of the piston rod that is exerted by the post-tensioning of four external steel rods (each post-tensioned rod exerts a force F), Π_s is a dimensionless coefficient, and $\Phi(\frac{u}{R}, \frac{D}{R})$ is a dimensionless function. Φ depends on the normalized stroke u/R and the normalized clearance of the moving sphere from the damper housing D/R, where R is the sphere radius that moves within a damper housing and is equal to 3 cm, and D is the diameter of the damper housing and is equal to 18.9 cm Makris et al. (2021). An ad-hoc assumption was made that

$$\Phi \left(\frac{u}{R}, \frac{D}{R} \right) \quad = \quad \Phi_u \left(\frac{u}{R} \right) \quad \cdot \quad \Phi_D \left(\frac{D}{R} \right) \tag{4.3}$$

Thus, the new form of Equation 4.2 follows as

$$F_d \quad = \quad \Pi_{SD} p R^2 \Phi_u \left(\frac{u}{R} \right) \quad = \quad Q \Phi_u \left(\frac{u}{R} \right) \tag{4.4}$$

Where Π_{SD} is a new dimensionless coefficient associated with the specific damper configuration (D/R = 6.3). $Q = \Pi_{SD} p R^2$ is the strength of the pressurized sand-damper (Makris et al., 2021).

4.1.1. Numerical Modeling of PSD

The generated DEM model and particle shape used to characterize the PSD is shown in Figure 3.2. The dry sand was represented by irregular shape sizes ranging from 2 mm to 4 mm in radius. The particles and facet (i.e. wall) frictions are set to be 0.5 and 0.15, respectively. Linear contact is established between rigid blocks as well as between the rigid block and a facet.

The frequency f_0= 20 Hz, and the amplitude u_0 has values of 4 and 6 cm. The pressure level p has values of 1.0, and 2.0 MPa . The sand solid density is 2660 kg/m^3. The dimensions of the sand damper and the characteristics of the utilized sand assembly considered in this study are selected to mimic the behavior of energy dissipation in the experimental cyclic loading configuration. The sphere is placed at the center of the rod. The length and the diameter of the PSD are 62 cm and 18.9 cm, respectively. The rod on which the sphere is attached has a length of 165 cm, and its diameter is 4 cm. The sphere radius in this case is 3 cm. The piston force was recorded during the course of the simulation.

The considered properties of the utilized pressurized sand damper in these studies for each case at varying pressure levels, displacement amplitudes, and piston configurations can be found in Table 4.1 listed below. For example, the porosity, particle solid density ρ, the pressure p, and shear stiffness of the particles and walls k_s, and normal stiffness of the particles and walls k_n, and friction coefficient μ are shown.

Table 4.1. DEM simulation parameters.

Amplitude	40, 60 mm
Frequency (f)	20 Hz
Pressure magnitude	1, 2, 3, 4, 5 MPa
Porosity	0.40
Particle solid density	2660 kg/m^3
Particle size range (Radius)	2-4, 1-5 mm
Number of particles	70,000
Wall normal stiffness	1e8 N/m
Wall shear stiffness	1e8 N/m
Wall friction coefficient	0.15
Normal viscous damping coefficient	0.1
Shear viscous damping coefficient	0.1
Particle normal stiffness	1e7 N/m
Particle shear stiffness	1e7 N/m
Particle friction coefficient	0.5

4.1.2. Validation Results

The obtained results were superimposed over the experimental results of same sand damper configuration in order to validate the DEM model in Figures 4.1-4.2. The applied pressure in these cases is p= 1, 2 MPa, the amplitude u_o= 40, 60 mm, and frequency of the cyclic tests is f_o= 20 Hz. Note that the loading frequency of 20 Hz is substantially higher than that used in the experiments to save simulation time. Makris et al. (2021) showed that there is no significant impact of loading frequency on the performance of the PSD. Figure 4.1 shows a comparison between obtained DEM and published experimental results for the force plotted against displacement of the PSD equipped with a single sphere-shaped configuration: (a) the applied pressure is p 1 MPa, the amplitude u_o= 40 mm, and (b) the applied pressure

is p 1 MPa, the amplitude u_o= 60 mm. Figure 4.1 shows the fairly good agreement between the DEM and experimental results.

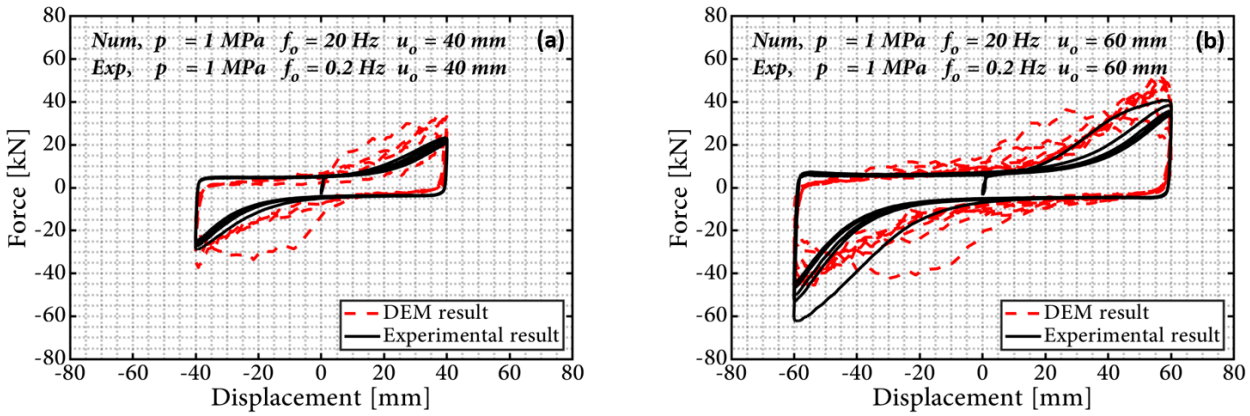

Figure 4.1. Comparison between obtained DEM and experimental published results for the force versus displacement of PSD equipped with a single sphere-shaped configuration: (a) The applied pressure is p= 1 MPa, the amplitude u_o= 40 mm, and (b) The applied pressure is p= 1 MPa, the amplitude u_o= 60 mm.

Both results exhibit similar cyclic force and displacement magnitude. For case (a), the maximum cyclic force magnitude obtained from the numerical simulation and the lab experimental test was around 30 kN. For case (b), the maximum cyclic force for both DEM and experimental result was approximately 60 kN. This was expected because of the longer stroke amplitude in case (b) recorded at u_o= 60 mm. A strain hardening behavior can also be detected in both cases when the piston reaches its maximum displacement amplitude in each direction, seen by steeper slope of the force displacement curves. This indicates soil dilative behavior during cycling motion. As can be seen from both DEM and experimental results in both cases (a) and (b), the first cyclic loop demonstrates a higher peak which gradually decreases in the following cycles in both the experimental and the DEM results.

Further DEM simulations were conducted that show a good agreement with the experimental lab test. Figure 4.2 shows similar cyclic loops for the force and displacement during cycling loading. Both the DEM and experimental results exhibit the same pattern in the first cycle. The first cyclic loop has a higher peak which gradually decreases in the following cycles. The applied pressure here in both cases are 2 MPa and the stroke amplitude in case (a) is u_o= 40 mm and in case (b) is u_o= 60 mm. As seen from the plots in case (a) and (b), the maximum forces are around 80 kN and 100 kN. The soil experiences similar behavior as in Figure 4.1 where a strain hardening behavior is exhibited in both cases when the piston reaches its maximum displacement in the direction of motion. As previously mentioned, this is seen in the steeper slope of the force displacement curves that indicate the soil dilative behavior during cycling motion.

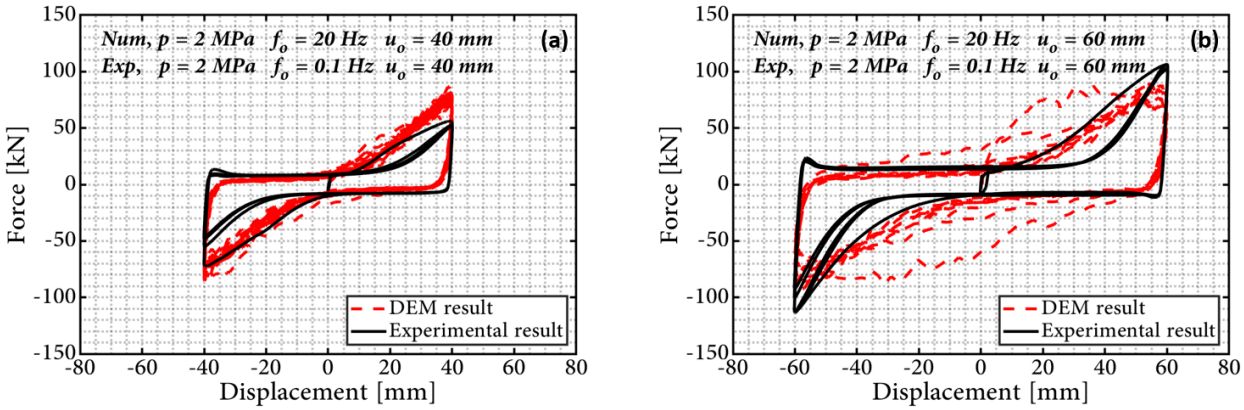

Figure 4.2. Comparison between obtained DEM and experimental published results for the force versus displacement of PSD equipped with a single sphere-shaped configuration: (a) The applied pressure is p= 2 MPa, the amplitude u_o= 40 mm, and (b) the applied pressure is p= 2 MPa, the amplitude u_o= 60 mm.

As previously discussed, the DEM simulations and experimental lab tests manifest a

similar pattern in all pressurized sand damper behavior for the force and displacement loops induced by the sphere movement and the harmonic excitation in the direction of motion. The harmonic velocity is

$$v_o = \omega u_o cos(\omega t) \tag{4.5}$$

which was recorded along the direction of motion of the pressurized sand damper. The motion of the sphere starts exactly at the origin of the rod. These findings are consistent with the above-mentioned data because the sand damper configuration that led to the above results agree. Furthermore, all of the DEM simulations and the experimental test results exhibit a strain hardening behavior. This occurs when the sphere reaches its maximum stroke amplitude in each direction, and is marked by a steeper slope in the force-displacement curves. This behavior indicates soil dilative behavior during cycling motion.

Chapter 5

RESULTS AND DISCUSSIONS

5.1. Mechanical Behavior of the PSD in Response with Different Technical Configurations and Particle Sizes

Energy dissipation is an important concept to help better understand the relationship between soils and structures. The discrete element method (DEM) is useful for simulating and modeling movement of granular materials through the process of observing individual particle interactions. The DEM can be used to characterize energy dissipation mechanisms in cyclically loaded soils. DEM simulations can also provide information at the microscopic and macroscopic levels. Energy monitoring is a useful means of understanding the interaction of particles at the microscopic level, which enhances understanding of the response mechanisms at the macroscale level. Seismic activity has prompted the investigation of the energy dissipation that occurs in soils to gain a better understanding of soil-structure interactions.

In this section, parametric study results will be presented. The findings of the considered utilization techniques of different numerical analyses were performed on various sand damper configurations. The scope of work considers a single, double, and triple spheres of pressurized sand damper configuration, conducted through 3-D transient discrete element simulations that occurred over 25 days. This research contained two approaches to cyclical loading in

DEM: the utilization of irregular, rather than spherical, particles and the use of the linear contact model to dictate the particle interactions. These adjustments to DEM simulations of cyclical loading allow the process to be reflected more accurately, and the results of the simulations were analogous to other studies which mutually confirmed their results. The force-displacement loops in the following figures in this chapter corresponded to the energy dissipation. This study showed that the experiments produced results that agreed with the DEM results regarding the impact of particle size and shape on the energy dissipation of the pressurized sand damper.

—

5.1.1. The Results of PSD with A single sphere-shaped under Varying Stroke Amplitude and Exerted Pressure

The energy dissipation mechanism was investigated in a pressurized sand damper equipped with a single sphere-shaped configuration. For instant, the effect of the exerted pressure p on the performance of the pressurized sand damper was examed. The obtained DEM results for the force-displacement hysteresis loop for varying pressure level and stroke amplitudes of u_o= 40, 60 mm can be seen in Figures 5.1-5.9. The applied pressure p in these cases varies from 1, 2, 3,4 ,5 MPa and loading frequency of the cyclic motion is f_o= 20 Hz. These figures manifest that as the exerted pressure increases the force capacity of the pressurized sand increases. It worth mentioning that, when the piston reaches its maximum displacement amplitude in each direction of loading (Y direction), the force displacement curves have a steeper slope, indicating strain hardening. This demonstrates soil dilative behavior while

cycling. As seen in all DEM results in all cases, the first cyclic loop has a higher peak that gradually decreases in subsequent cycles. This behavior was also evident in all of the experimental results. It is due to the expansion of particles during cyclic shearing. Figures 5.10 and 5.11 show the magnitude of the dissipated energy of the pressurized sand damper for the simulation conducted at applied pressure of p= 1.0 ,2.0 ,3.0 , and 4.0 MPa, and amplitude displacement of u_o= 40,60 mm. This figure confirm that the increase of the dissipated energy as the sand damper operates at high pressure magnitudes.

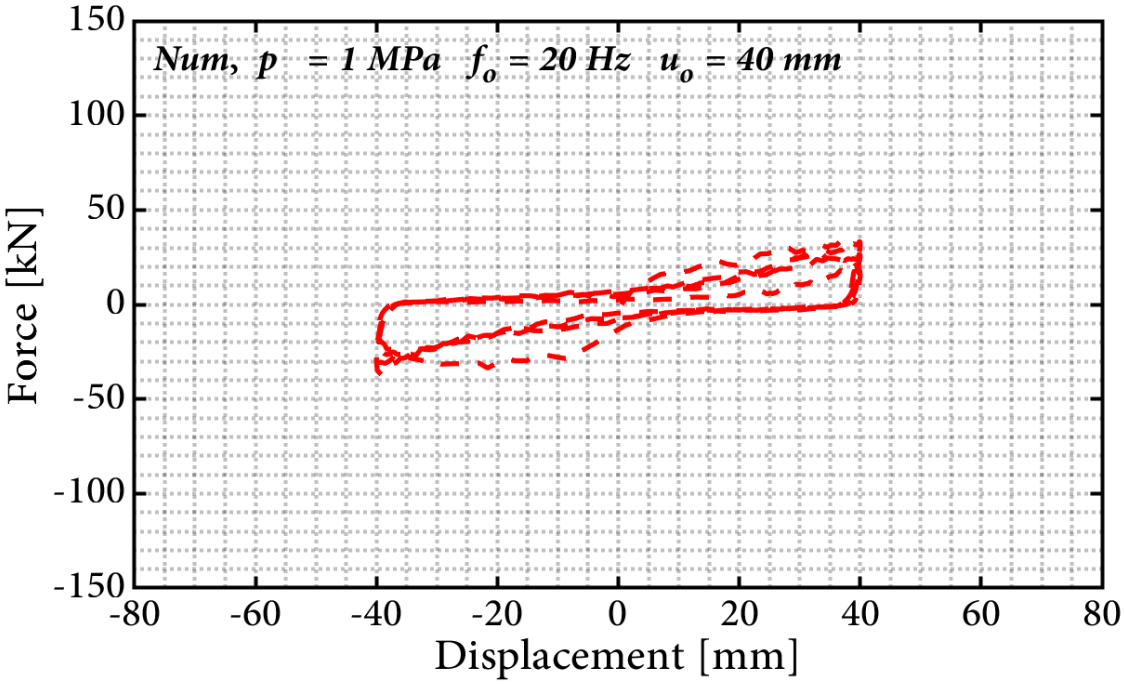

Figure 5.1. The obtained DEM result for the force versus displacement of PSD equipped with a single sphere-shaped configuration. The applied pressure is p= 1 MPa; the displacement amplitude is u_o= 40 mm; and frequency of the cyclic loading f_o= 20 Hz.

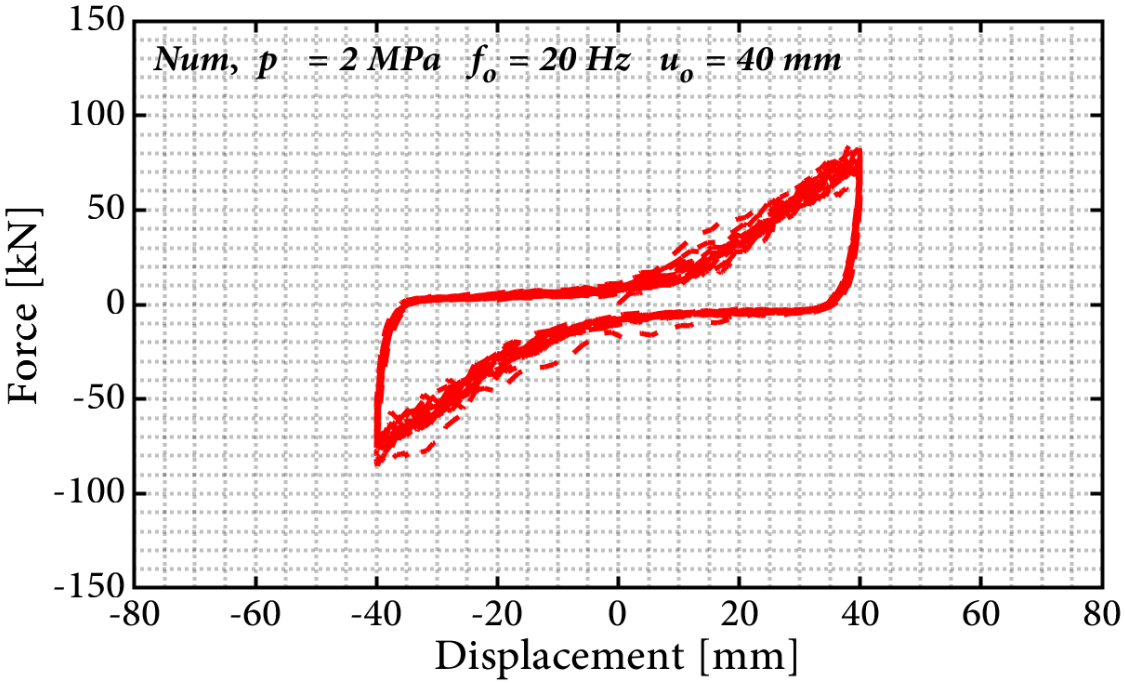

Figure 5.2. The obtained DEM result for the force-displacement loops of PSD equipped with a single sphere-shaped configuration. The applied pressure is p= 2 MPa; the displacement amplitude is u_o= 40 mm; and frequency of the cyclic loading f_o= 20 Hz.

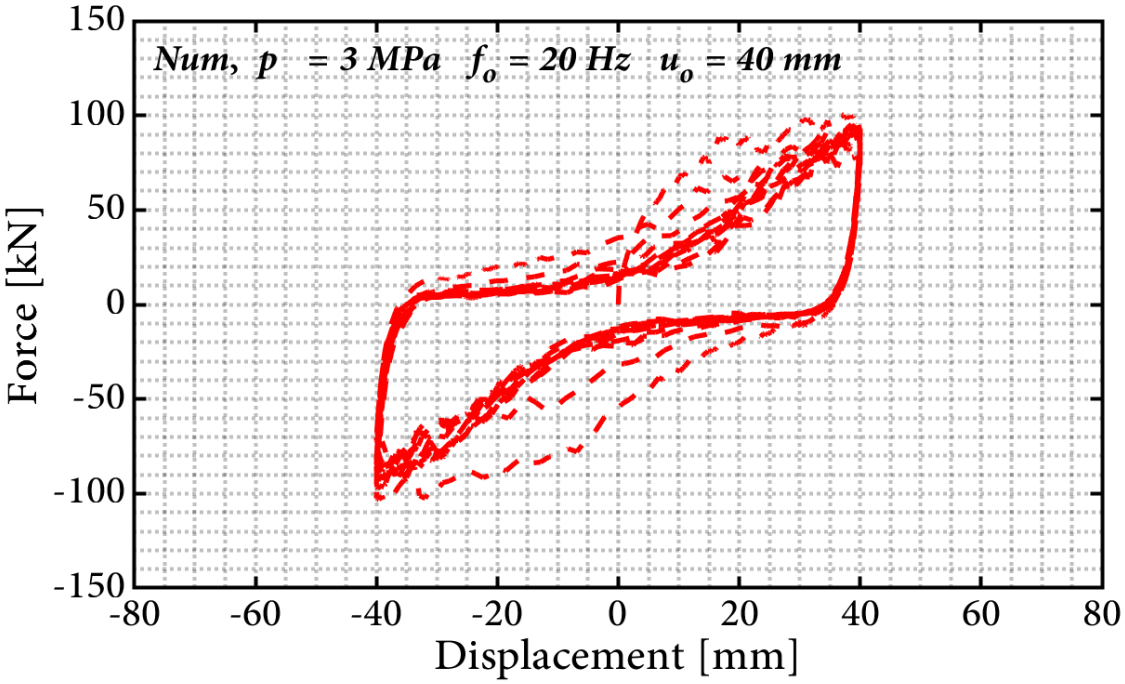

Figure 5.3. The obtained DEM result for the force-displacement loops of PSD equipped with a single sphere-shaped configuration. The applied pressure is p= 3 MPa; the displacement amplitude is u_o= 40 mm; and frequency of the cyclic loading f_o= 20 Hz.

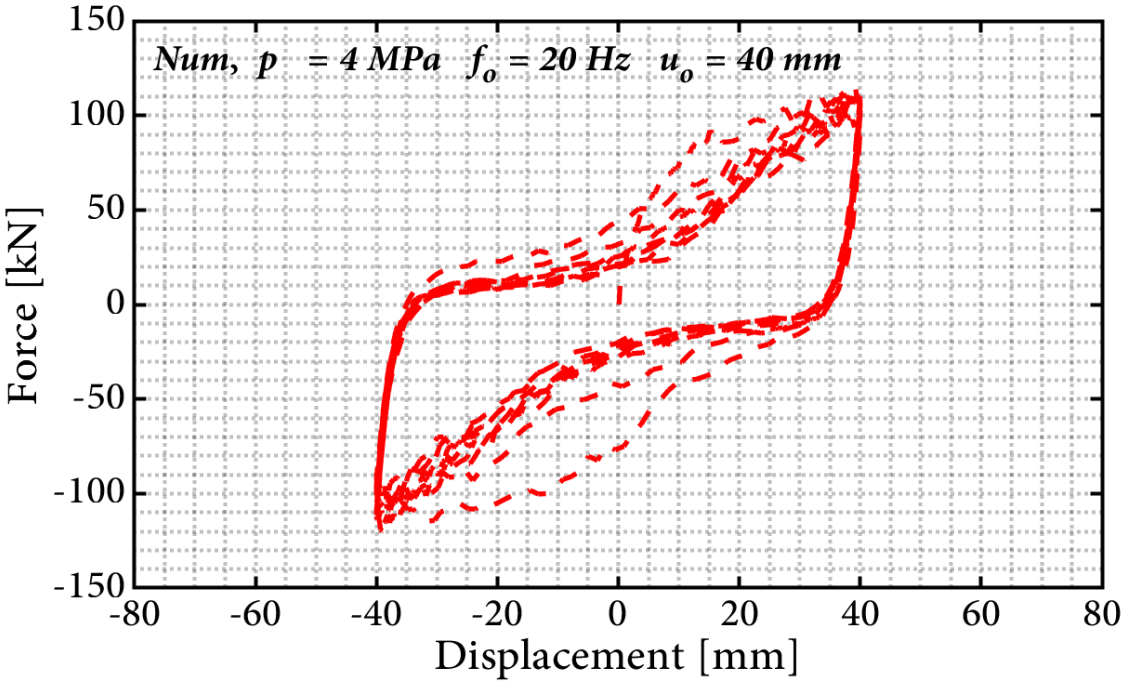

Figure 5.4. The obtained DEM result for the force-displacement loops of PSD equipped with a single sphere-shaped configuration. The applied pressure is p= 4 MPa; the displacement amplitude is u_o= 40 mm; and frequency of the cyclic loading f_o= 20 Hz.

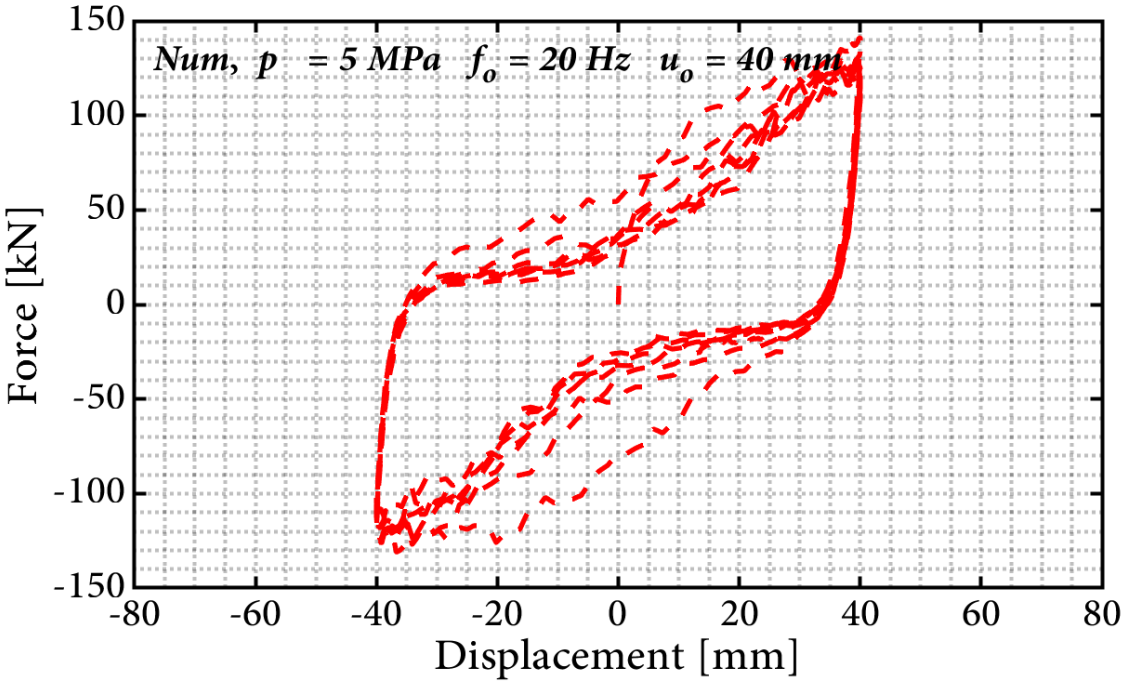

Figure 5.5. The obtained DEM result for the force-displacement loops of PSD equipped with a single sphere-shaped configuration. The applied pressure is p= 5 MPa; the displacement amplitude is u_o= 40 mm; and frequency of the cyclic loading f_o= 20 Hz.

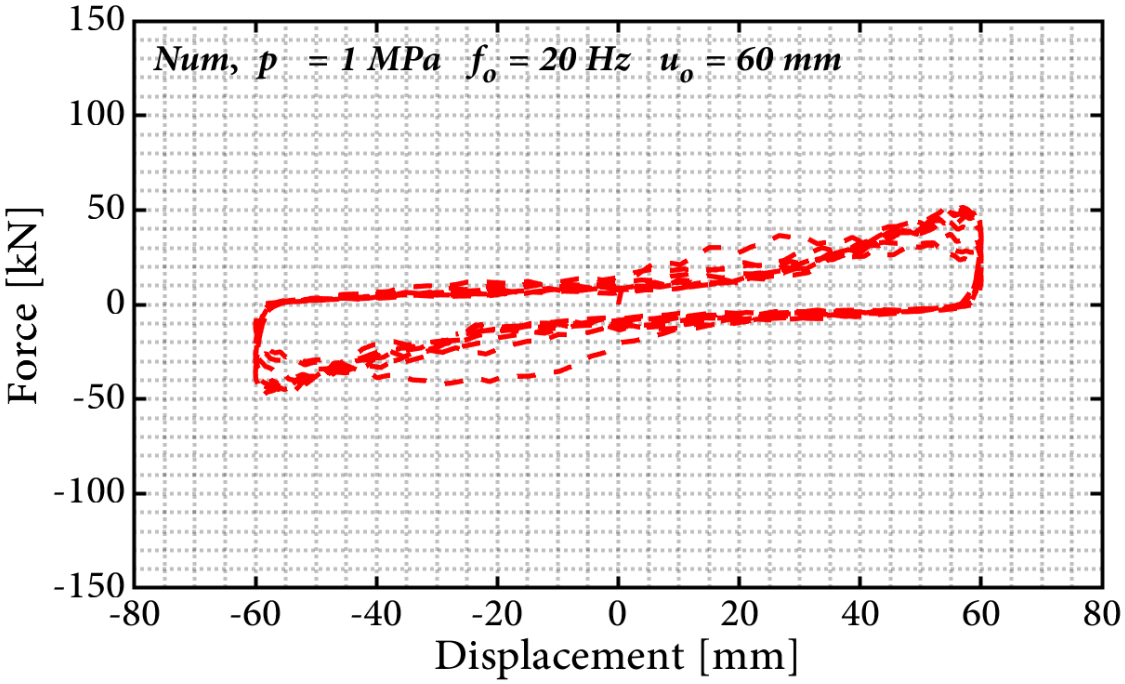

Figure 5.6. The obtained DEM result for the force-displacement loops of PSD equipped with a single sphere-shaped configuration. The applied pressure is p= 1 MPa; the displacement amplitude is u_o= 60 mm; and frequency of the cyclic loading f_o= 20 Hz.

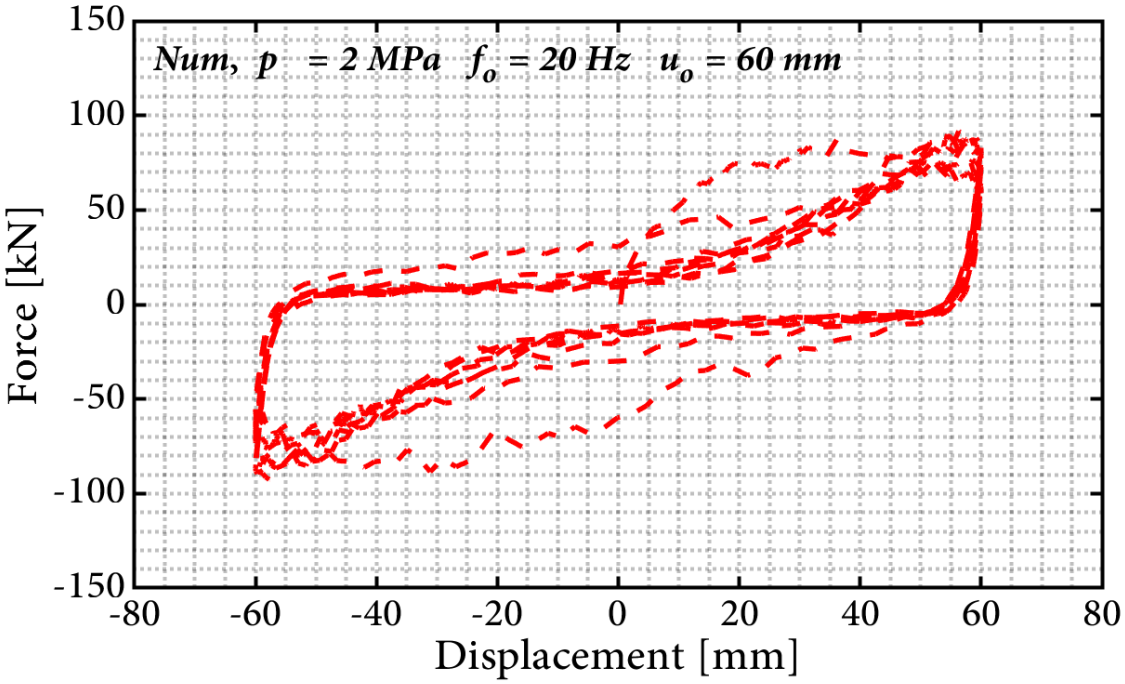

Figure 5.7. The obtained DEM result for the force-displacement loops of PSD equipped with a single sphere-shaped configuration. The applied pressure is p= 2 MPa; the displacement amplitude is u_o= 60 mm; and frequency of the cyclic loading f_o= 20 Hz.

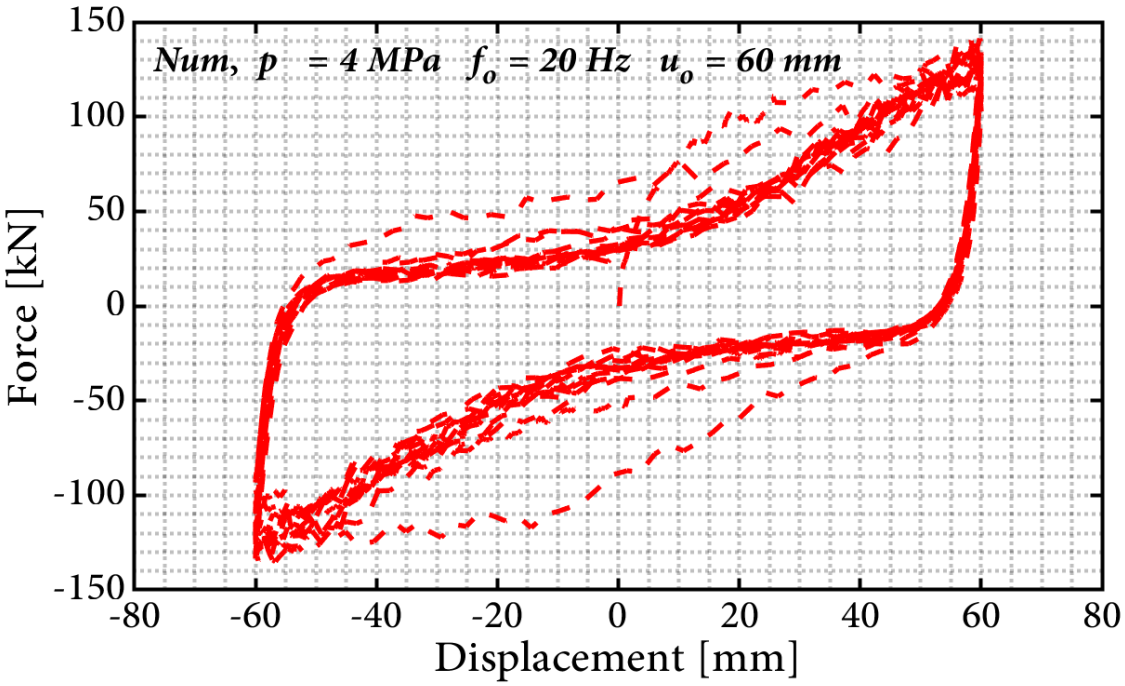

Figure 5.8. The obtained DEM result for the force-displacement loops of PSD equipped with a single sphere-shaped configuration. The applied pressure is $p = 4$ MPa; the displacement amplitude is u_o= 60 mm; and frequency of the cyclic loading f_o= 20 Hz.

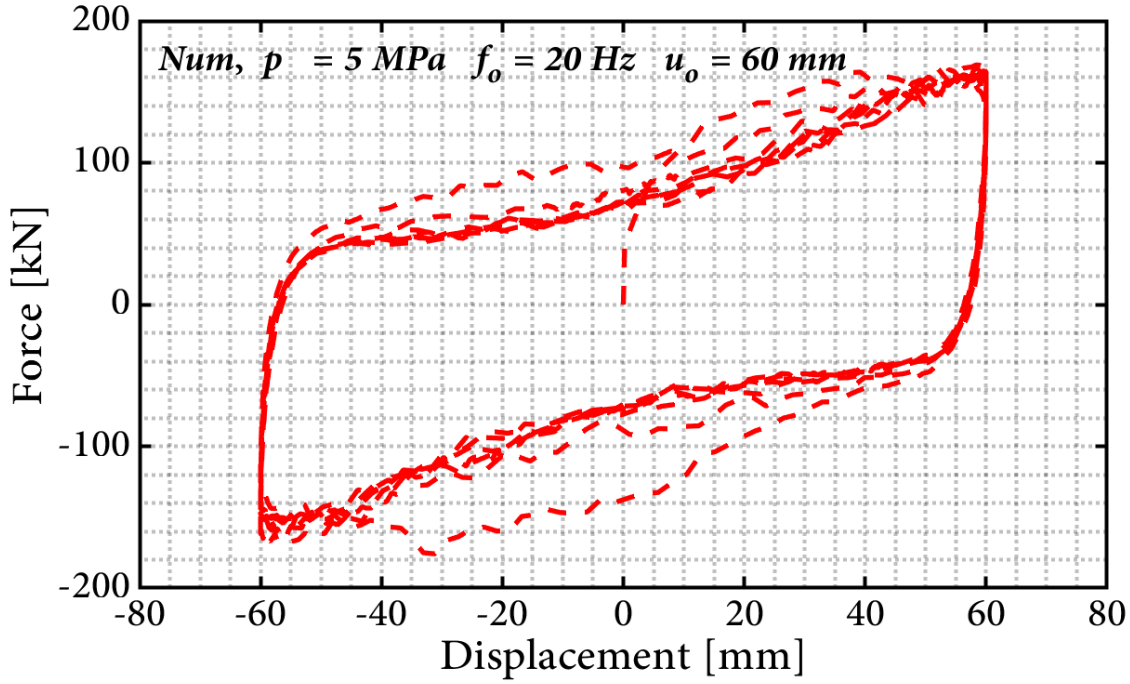

Figure 5.9. The obtained DEM result for the force-displacement loops of PSD equipped with a single sphere-shaped configuration. The applied pressure is $p = 5$ MPa; the displacement amplitude is u_o= 60 mm; and frequency of the cyclic loading f_o= 20 Hz.

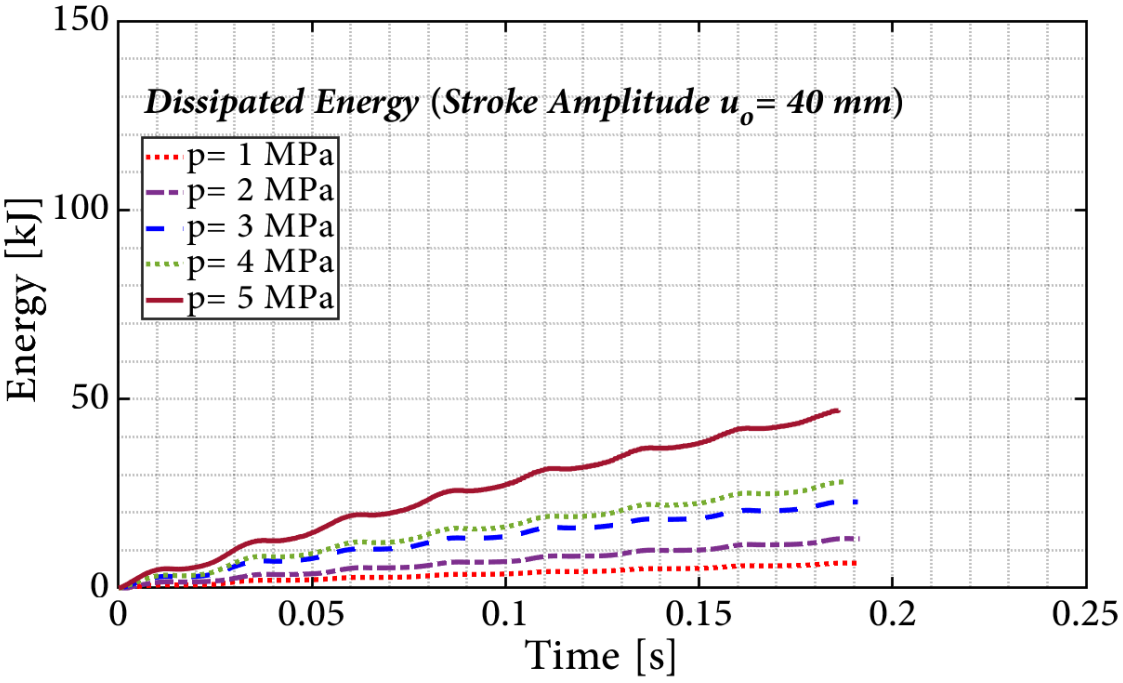

Figure 5.10. Time-history of dissipated energy for the numerical results at varying pressure levels and stroke amplitudes of u_o= 40 mm. The PSD is equipped with a single sphere-shaped configuration.

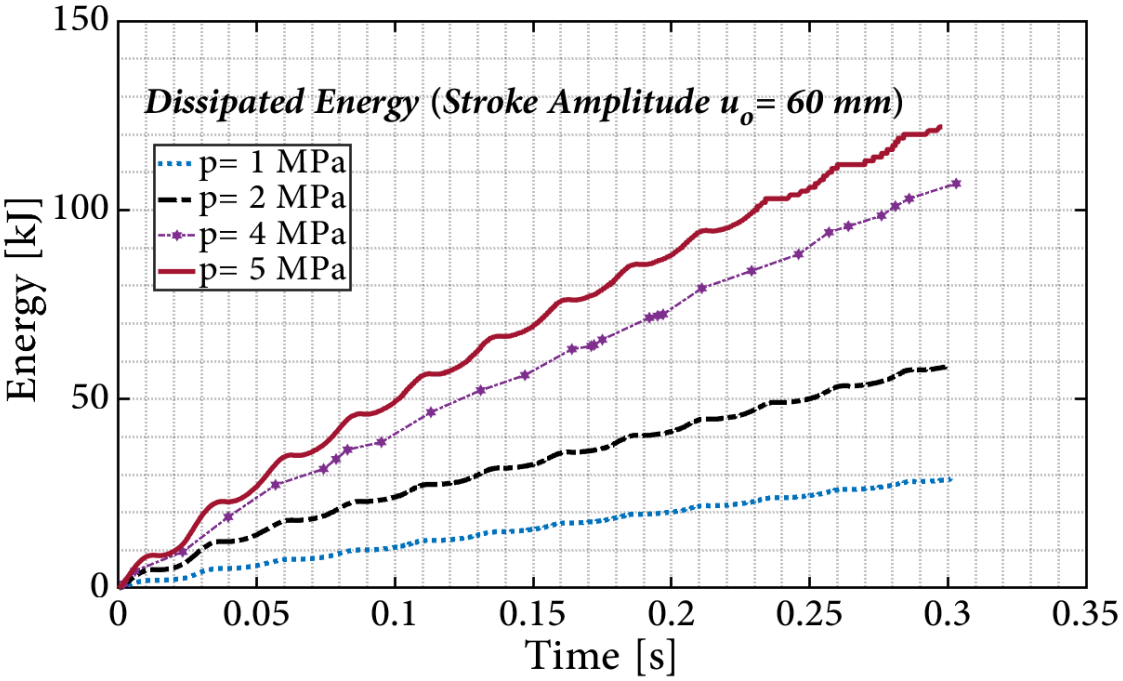

Figure 5.11. Time-history of dissipated energy for the numerical results at varying pressure levels and stroke amplitudes of u_o= 60 mm. The PSD is equipped with a single sphere-shaped configuration.

Figure 5.12 shows the dissipated energy of several DEM simulation cases with different pressure levels and stroke amplitudes. The magnitude of cumulative dissipated energy increased with the pressure level applied to the sand damper, as well as increasing the stroke amplitude of the loading.

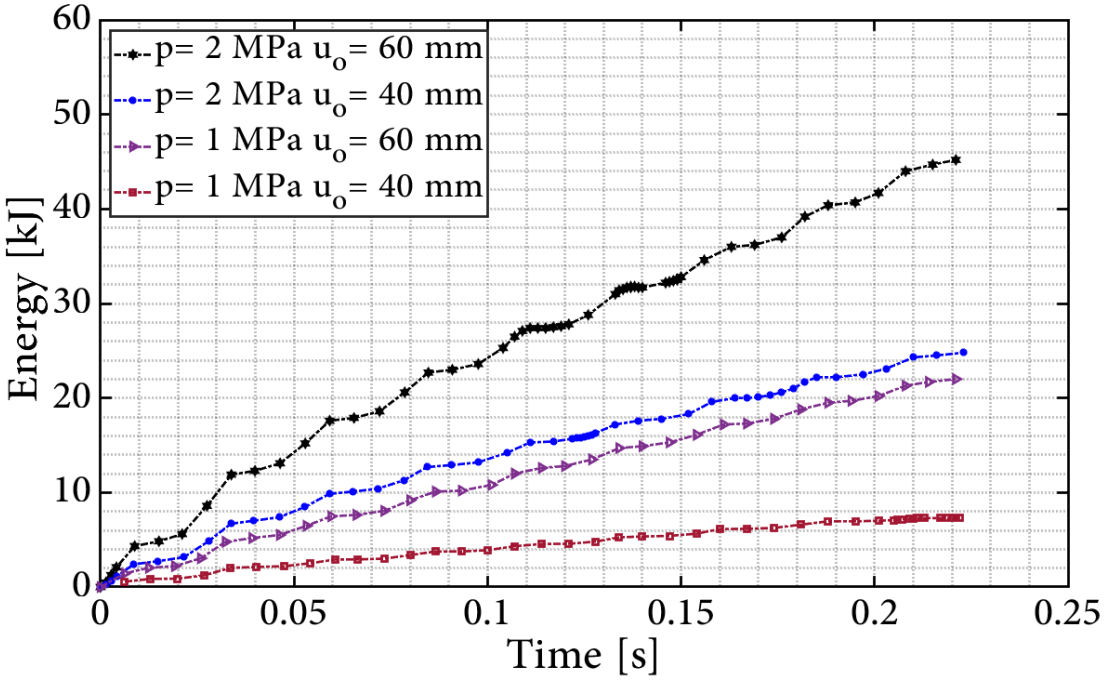

Figure 5.12. Time-history of dissipated energy for the numerical results at varying pressure levels and stroke amplitudes. The PSD is equipped with a single sphere-shaped configuration.

In all the conducted simulations, the energy components were traced. The use of the DEM allows tracking energies such as the input (boundary) energy, the strain energy, the frictional work, and the kinetic energy and viscous damping energy. Figures 5.13 and 5.14 display energy components that were traced during the simulation. The applied pressure in both cases are p= 5 MPa and the stroke amplitude in Figures 5.13 is u_o= 40 mm and in Figure 5.14 is u_o= 60 mm. The loading frequency in both cases is f_o= 20 Hz.

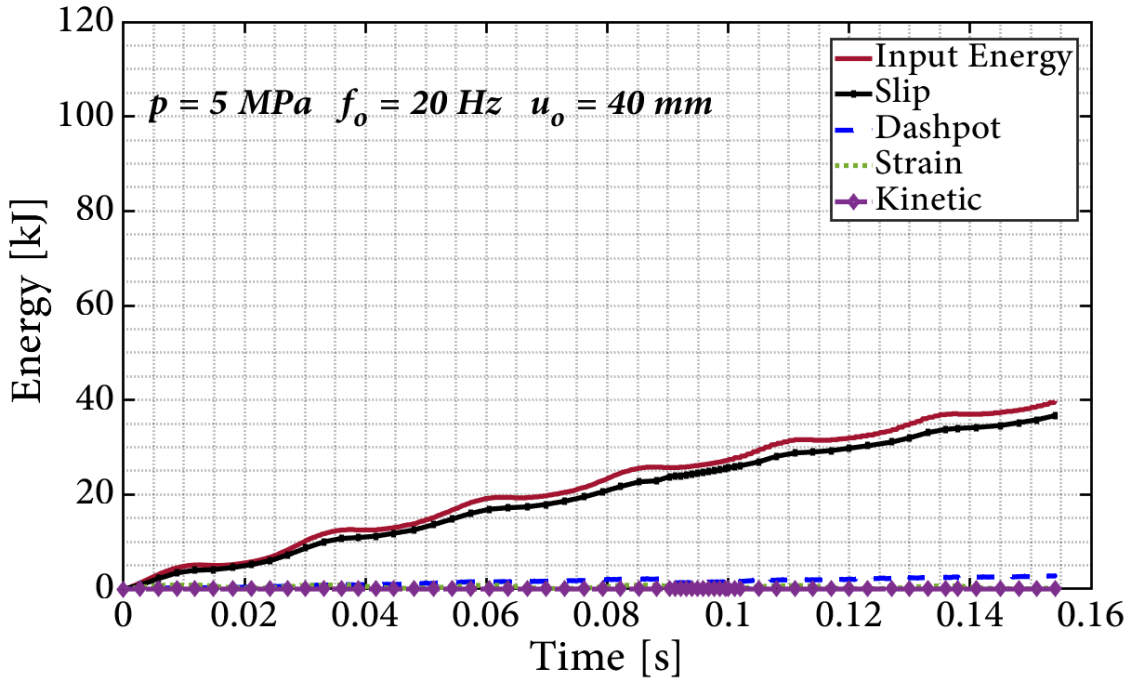

Figure 5.13. Time-history of input, kinetic, dashpot, strain, and slip energies for the obtained results by applying pressure level of p= 5 MPa, stroke amplitude of u_o= 40 mm, and frequency of the cyclic loading f_o= 20 Hz. The sand damper is equipped with a single sphere configuration.

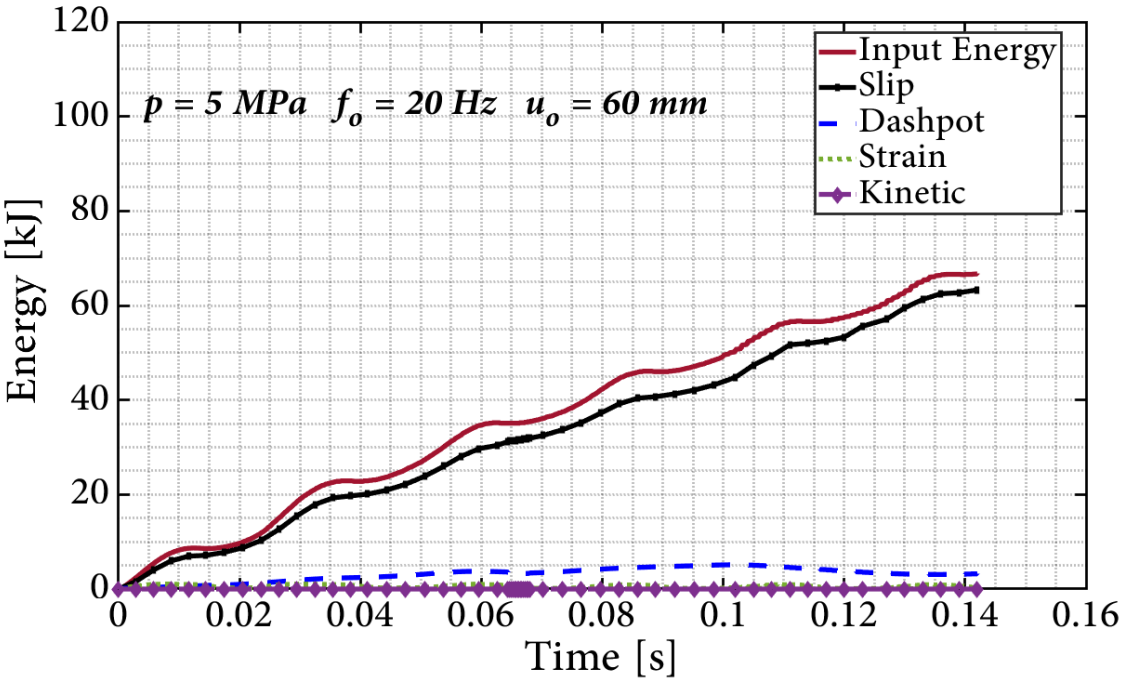

Figure 5.14. Time-history of input, kinetic, dashpot, strain, and slip energies for the obtained results by applying pressure level of p= 5 MPa, stroke amplitude of u_o= 60 mm; and frequency of the cyclic loading f_o= 20 Hz. The sand damper is equipped with a single sphere-shaped configuration.

Figure 5.15 shows the time-history of the energy balance for the input and dissipated energies during cyclic loading for the different cases. As it can be seen in the figure, the dissipated energy increases as the stroke amplitude increases. The input energy and the dissipated energy for each case overlaps as expected from the energy balance. The input

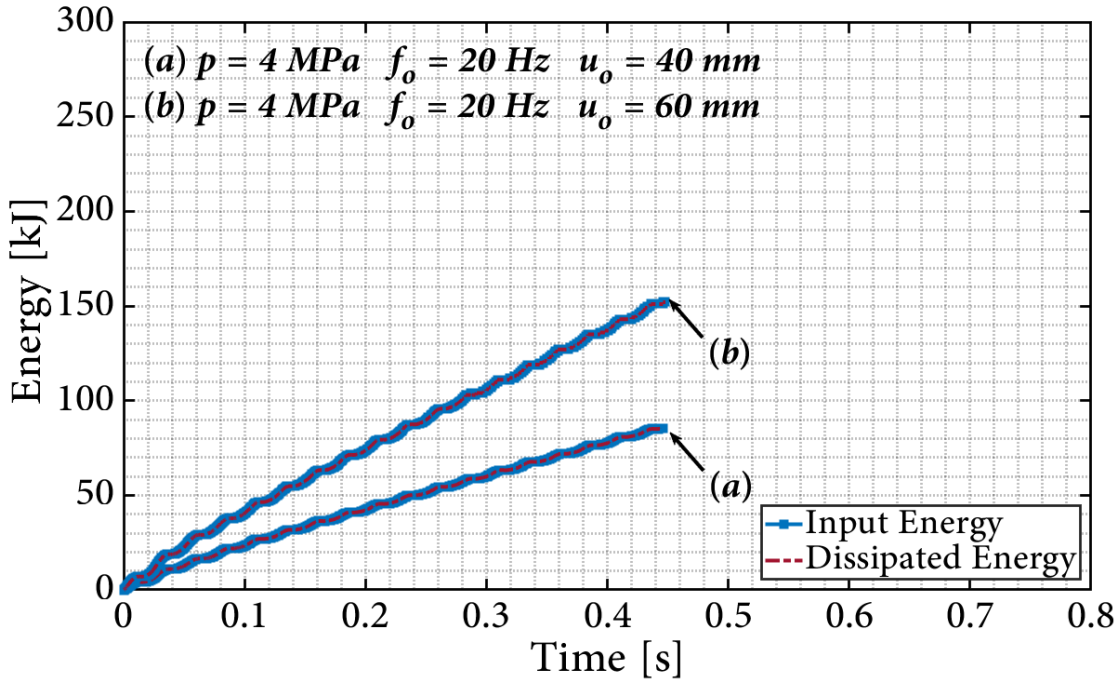

Figure 5.15. Time-history of the energy balance for two DEM simulations results by applying pressure level of p= 4 MPa and stroke amplitudes of u_o= 40 mm and u_o= 60 mm in case (a) and (b), respectively. The frequency of the cyclic loading is f_o= 20 Hz. The PSD is equipped with a single sphere-shaped configuration.

energy is the work done by the moving piston that accumulated over time at each piston-particle contact throughout the existence of that contact. At each timestep, the boundary work (input energy) is defined by Equation 3.37 (Itasca, 2018). The output is the dissipated energy due to strain, kinetic, friction, viscous damping energies. These energies are also accumulated over time at each contact throughout the existence of that contact.

Figure 5.16 shows the division of the sand damper particles into 9 zones with the intent of comparing each zone to better understand the variation of dissipated energy in the sand damper. Section 1 is located at the centerline of the piston at the origin. Section 2 is

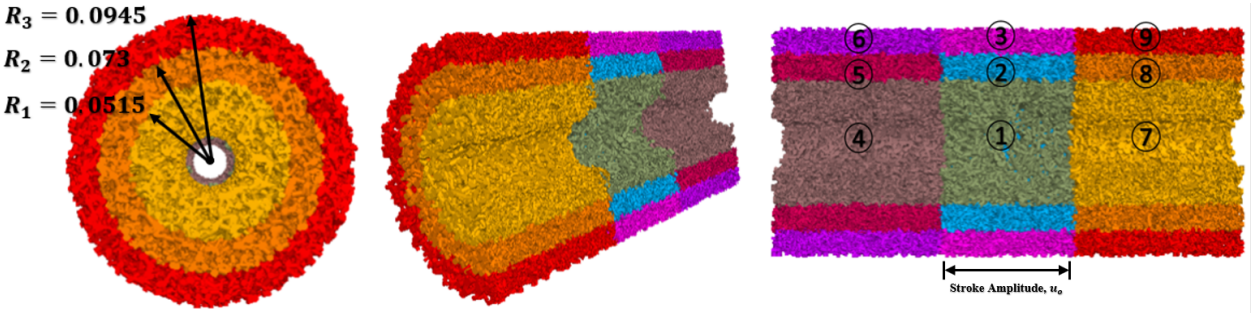

Figure 5.16. The nine groups of the pressurized sand damper used to locate the maximum magnitude of the dissipated energy.

located at the origin immediately surrounding Section 1. Section 3 is located around Section 2, touching the walls of the sand damper. Sections 4, 5, and 6, and Sections 7, 8, and 9 follow a similar pattern.

Figure 5.17 shows the dissipated energy due to frictional interactions between all the contacts inside the pressurized sand dampers in the corresponding zones. The maximum amount of the dissipated energy is located where around zone 1 as followed by zones 4 and 7. The rest of the zones in Figure 5.17 manifest a much lower dissipated energy as expected because they are not in direct contact with the piston.

Figure 5.18 shows the dissipated energy due to the dashpot. The magnitude of the dissipated energy in the dashpot is much smaller than that of the frictional losses, as seen in the difference in axis labels (kJ in 5.17 and J in 5.18). As mentioned in the 2, many studies have shown that frictional losses are the main mechanism of energy dissipation.

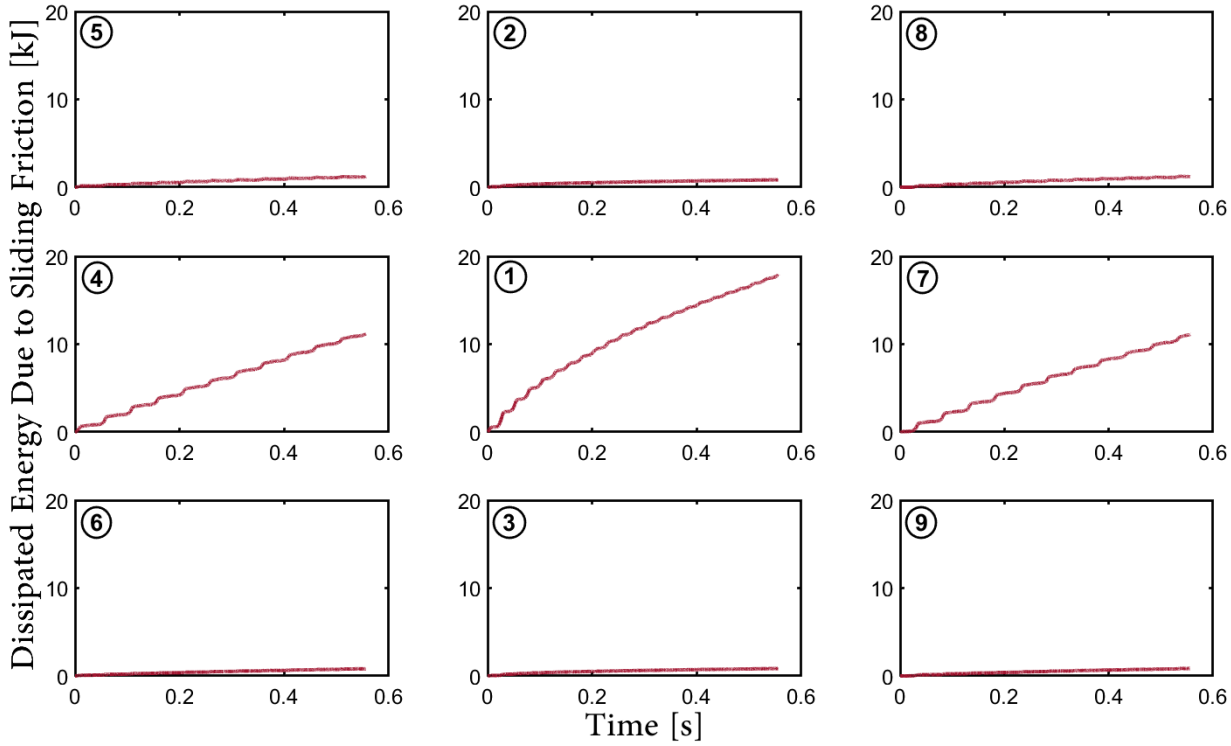

Figure 5.17. The particle contacts divided into nine groups to locate the maximum magnitude of the dissipated frictional energy in the pressurized sand damper.The applied pressure is p= 1 MPa and stroke amplitude of u_o= 60 mm. The frequency of the cyclic loading is f_o= 20 Hz.

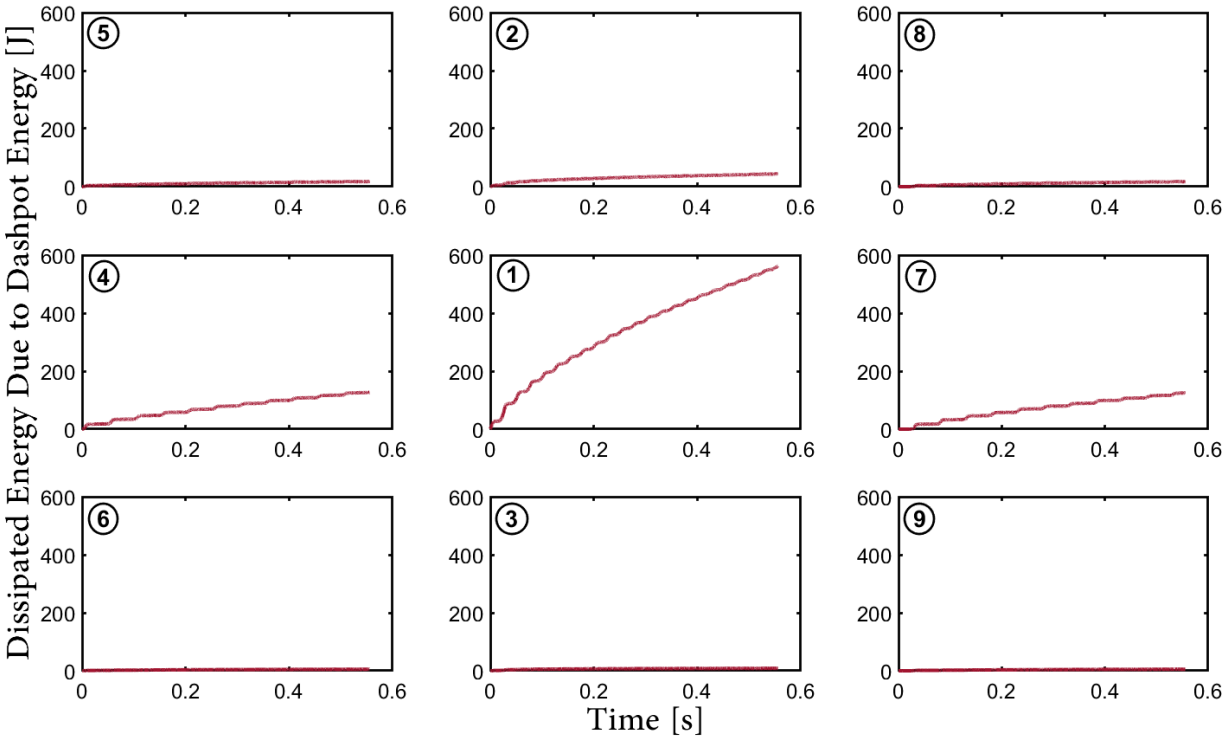

Figure 5.18. The particle contacts divided into nine groups to locate the maximum magnitude of the dissipated dashpot energy in the pressurized sand damper. The applied pressure is p= 1 MPa and stroke amplitude of u_o= 60 mm. The frequency of the cyclic loading is f_o= 20 Hz.

Figure 5.19 shows the dissipated energy due to strain deformation. As the sphere moves towards its maximum stroke amplitude, the particles experience more deformation at the Sections 4 and 7 as the particles are being pushed under shearing loading by the piston to the edges of the sand damper. The dissipated energy due to strain deformation is much lower than frictional losses, as the units in Figure 5.19 are in J, not kJ as in Figure 5.17. Also comparing the results in 5.19 to the dashpot energy results in 5.18, there is less strain energy dissipated than dashpot energy dissipated.

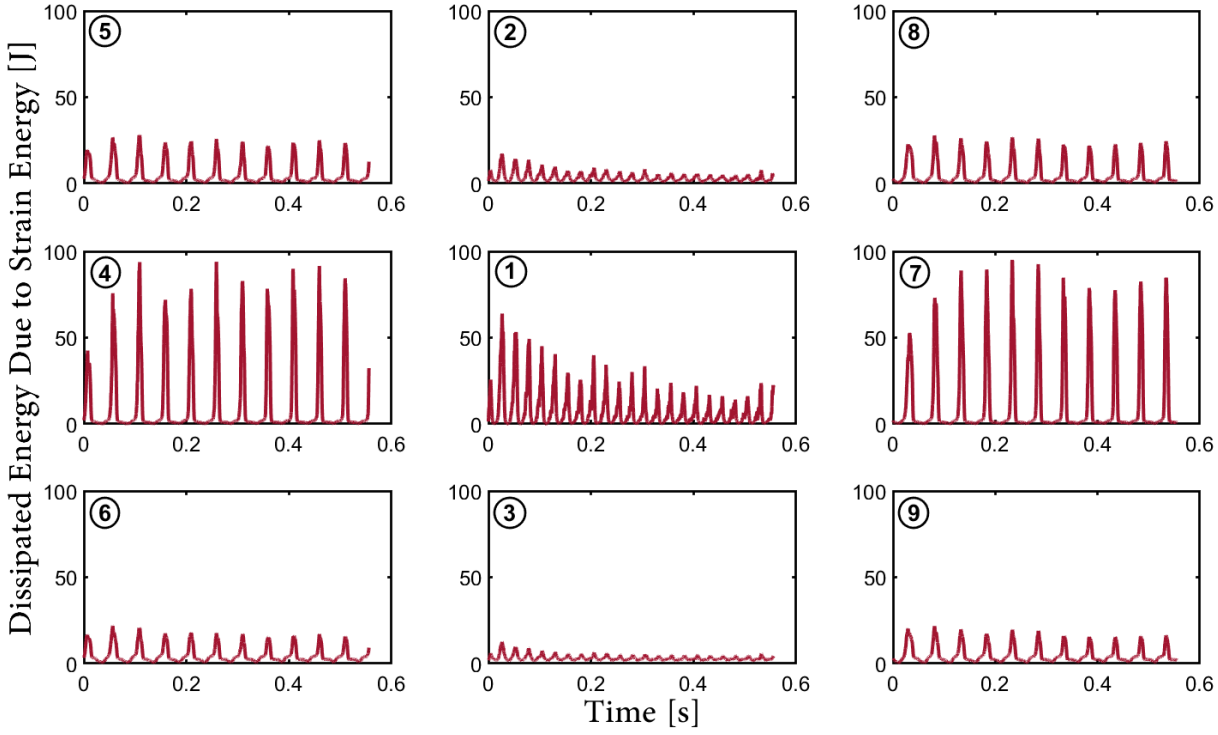

Figure 5.19. The particle contacts divided into nine groups to locate the maximum magnitude of the dissipated strain energy in the pressurized sand damper. The applied pressure is p= 1 MPa and stroke amplitude of u_o= 60 mm. The frequency of the cyclic loading is f_o= 20 Hz.

Figure 5.20 demonstrates that the particle-particle interactions yield a larger magnitude of dissipated energy compared to the piston-particle interactions. This is as expected from the larger value of the friction coefficient for the particles and the walls (piston).

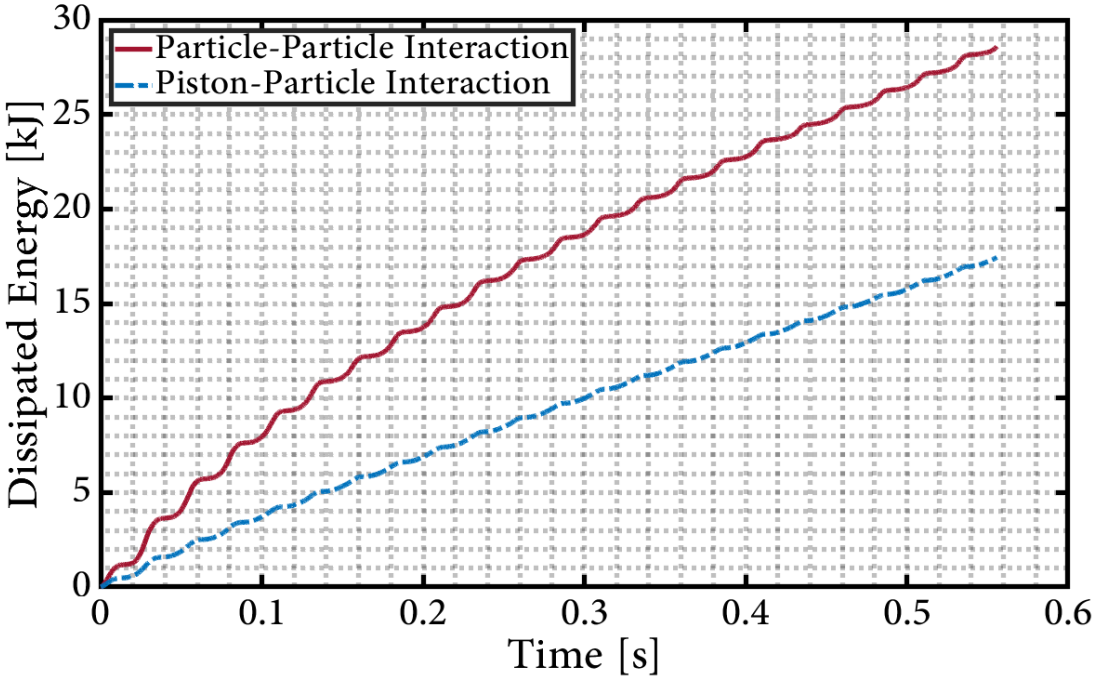

Figure 5.20. The magnitude of the dissipated energy due to particle-to-particle and particle-to-piston interactions in the pressurized sand damper. The applied pressure is p= 1 MPa and stroke amplitude of u_o= 60 mm. The frequency of the cyclic loading is f_o= 20 Hz.

5.1.1.1. Cyclic Shear Stress and Cyclic Shear Strain

The plots of the cyclic shear stress-strain loops at different locations inside the sand damper can be seen in Figure 5.21.

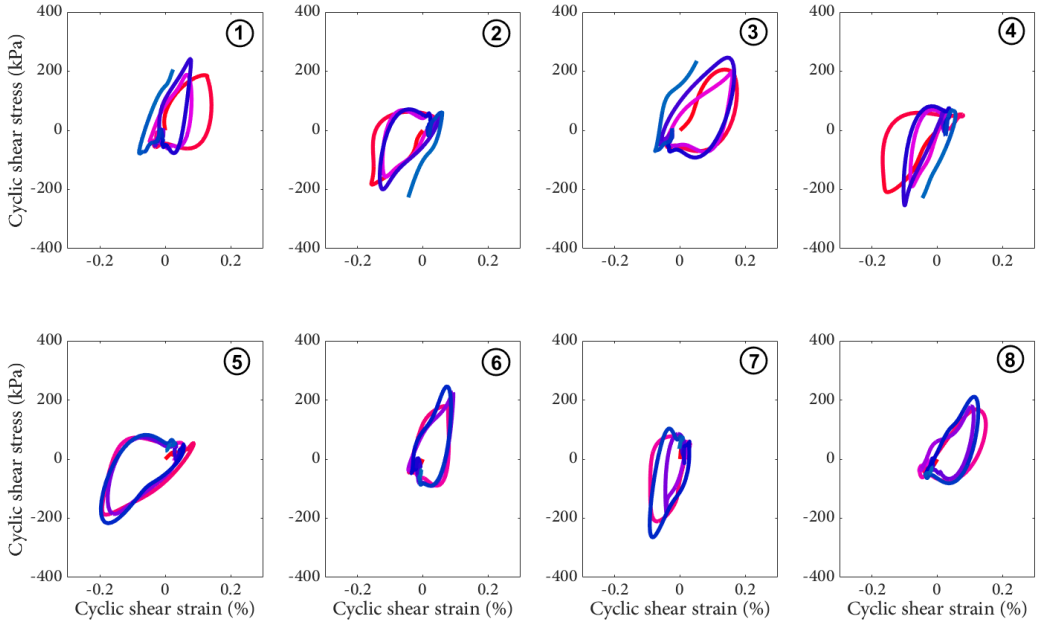

Figure 5.21. Cyclic shear stress-strain loops at different locations inside the sand damper. The sand damper is equipped with a single piston-shaped configuration. The applied pressure is p= 1 MPa, the amplitude u_o= 40 mm, and frequency of the cyclic tests f_o= 20 Hz.

The sand damper is equipped with a single piston-shaped configuration. The applied pressure is p= 1 MPa, the amplitude u_o=40 mm, and frequency of the cyclic tests is f_o= 20 Hz. As seen in Figure 5.21, a one-sided loop happened at measurement points, meaning that shear stress was significantly higher in the loading direction. The shear stress was maximum in the positive direction at points (1),(3),(6) and (8) while it was the opposite for points (2),(4),(5) and (7). The reason is that points (1),(3),(6) and (8) are located on the right side

of the sphere and when the sphere is moving in the positive direction, so the stresses at this locations will be much higher. The opposite side exhibited similar behavior in the negative direction which are located in the left side of the sphere. The maximum cyclic shear stress amplitude was approximately 200 kPa at all points.

Figure 5.22 shows cyclic shear stress-strain loops at different locations inside the sand damper. The sand damper is equipped with a single piston-shaped configuration. The applied pressure is p= 1 MPa, and the stroke amplitude is u_o= 60 mm, at the same motion frequency of f_o= 20 Hz.

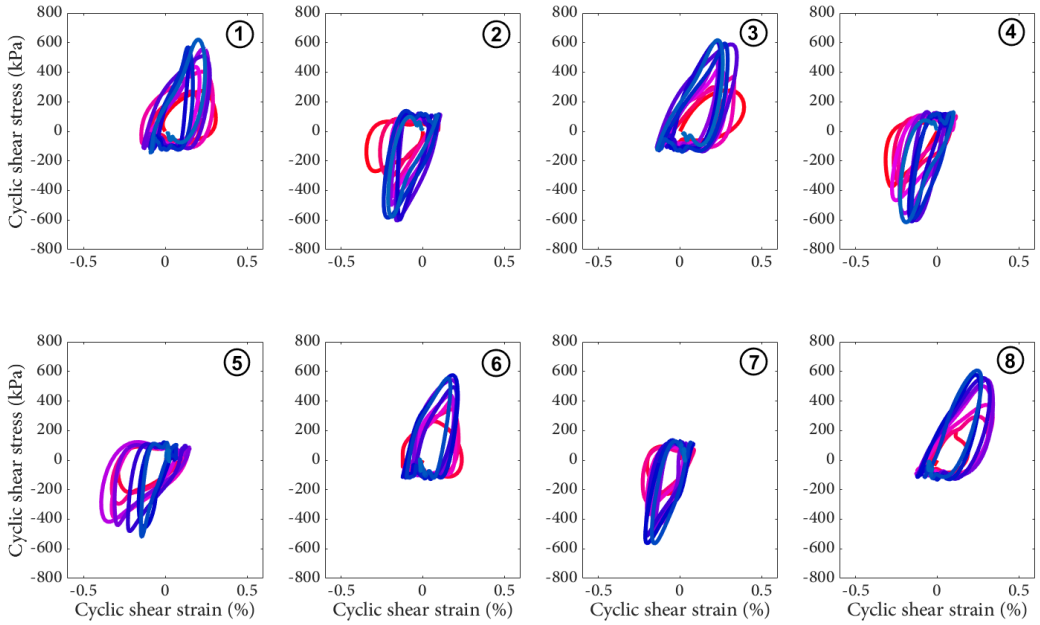

Figure 5.22. Cyclic shear stress-strain loops at different locations inside the sand damper. The sand damper is equipped with a single piston-shaped configuration. The applied pressure is p= 1 MPa, the amplitude u_o= 60 mm, and frequency of the cyclic tests f_o= 20 Hz.

A similar pattern of Figure 5.21 can be seen here, where locations on the right side of the piston-sphere experienced large positive shear stresses while the points that are located on the left side of the piston-sphere had larger negative shear stresses. However, the maximum magnitude of the cyclic shear stresses were significantly higher, 600 kPa compared to 200 kPa in this case. Figure 5.22 shows a gradual degradation of soil stiffness as the cyclic motion continues. This was not seen in Figure 5.21 where the motion amplitude was smaller (u_o= 40 mm).

Figure 5.23 shows similar loops for the cyclic stress-strain to Figure 5.21. However, the maximum shear stress amplitude has increased from 200 kPa to 500 kPa due to the increase of the applied pressure from p= 1 MPa to p= 2 MPa. From the area inside the loops it can be inferred that the amount of the energy dissipation here was noticeably higher that the case where the pressure was p= 1 MPa.

Another case for cyclic stress-strain loops is that the applied amplitude displacement has been increased from u_o= 40 mm as seen Figure 5.24 to u_o= 60 mm. The maximum shear stress has increased from approximately 500 kPa to 1000 kPa due to the stroke amplitude increase. As seen in Figures 5.21-5.24 the color mapping of the plots defines the number of cycles ranging from blue to red.

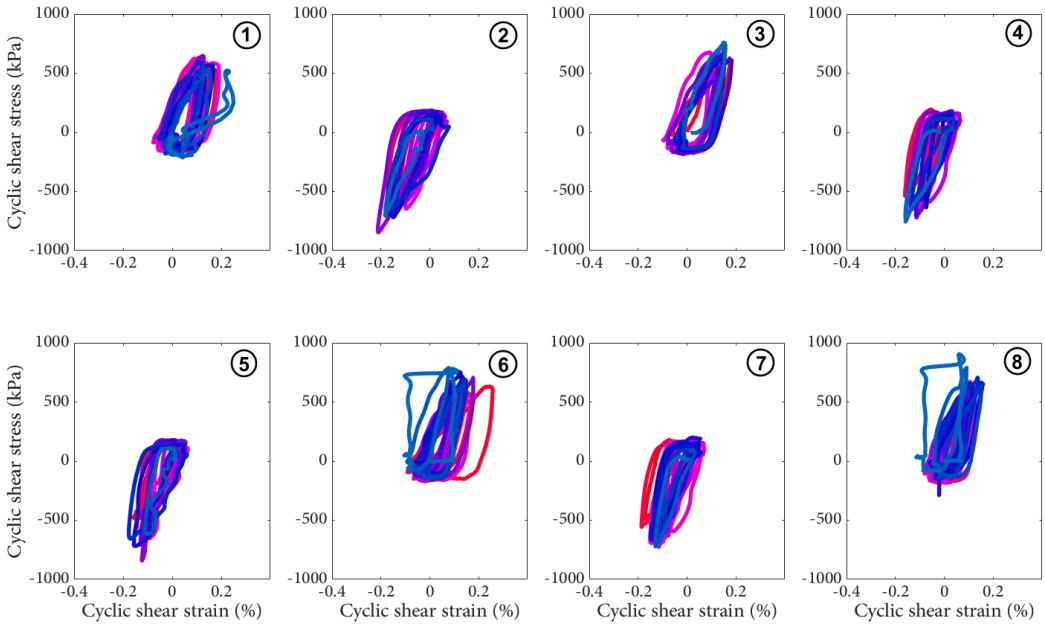

Figure 5.23. Cyclic shear stress-strain loops at different locations inside the sand damper. The sand damper is equipped with a single piston-shaped configuration. The applied pressure is p= 2 MPa; the amplitude u_o= 40 mm; and frequency of the cyclic tests f_o= 20 Hz.

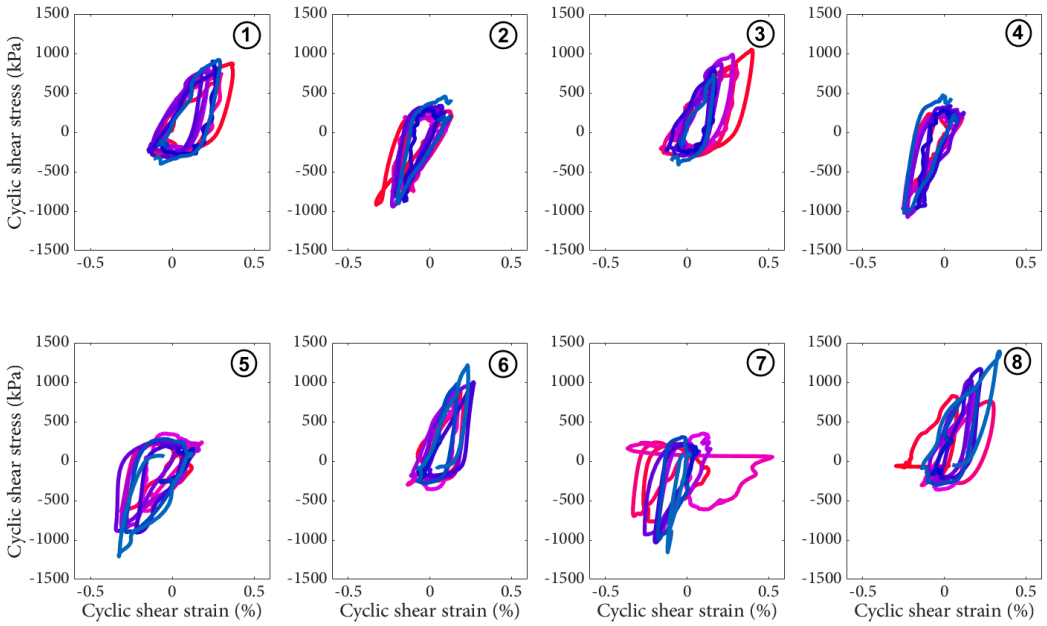

Figure 5.24. Cyclic shear stress-strain loops at different locations inside the sand damper. The sand damper is equipped with a single piston-shaped configuration. The applied pressure is p= 2 MPa; the amplitude u_o= 60 mm; and frequency of the cyclic tests f_o= 20 Hz.

5.1.2. PSD Response with the Different Configuration and Particle Sizes

5.1.2.1. Piston Ball Roughness

In this simulation, the coefficient of friction between sphere and particles was increased from 0.15 to 0.9 to enable study of the effect of roughness on energy dissipation. This case is conducted when the sand damper is equipped with a single sphere with the sphere size shown in Figure 3.6. The sand damper filled with irregular particles. It is important to mention that the inter-particles friction coefficient was kept 0.5. The applied pressure in these simulations is p= 1 MPa, the stroke amplitude is u_o= 60 mm, and the loading frequency of both cases are f_o= 20 Hz. Figure 5.25 shows a comparison between results obtained from DEM simulations for the relationship between the force and displacement of the PSD equipped with a single sphere-shaped configuration. By increasing the ball friction coefficient, the force output of the piston remains almost the same. A comparison between obtained DEM results for dissipated energy over loading can be seen in Figure 5.26. By increasing the friction coefficient of the piston sphere, the amount of dissipated energy increased just only by 7.05%.

5.1.2.2. Piston Enlarged Sphere-Size

Makris et al. (2021) defined the quadratic dependence of the drag force F_s on the radius of sphere R under exerted pressure p. Equation 5.1 shows the drag force as a function of the exerted pressure, p, along the direction of motion and the radius of the sphere, R.

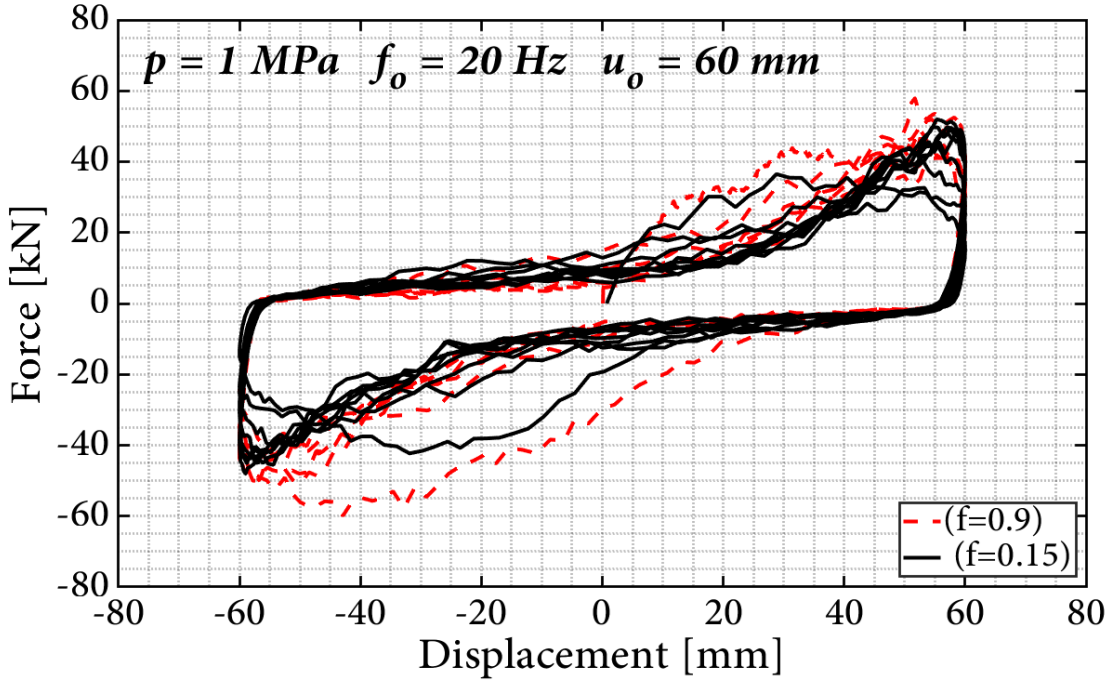

Figure 5.25. Comparison between obtained DEM results for the force versus displacement of PSD equipped with a single sphere-shaped configuration when the wall (sphere) friction is set to be 0.15 and 0.9. The applied pressure is p= 1 MPa; the amplitude u_o= 60 mm; and frequency of the cyclic loading is f_o= 20 Hz.

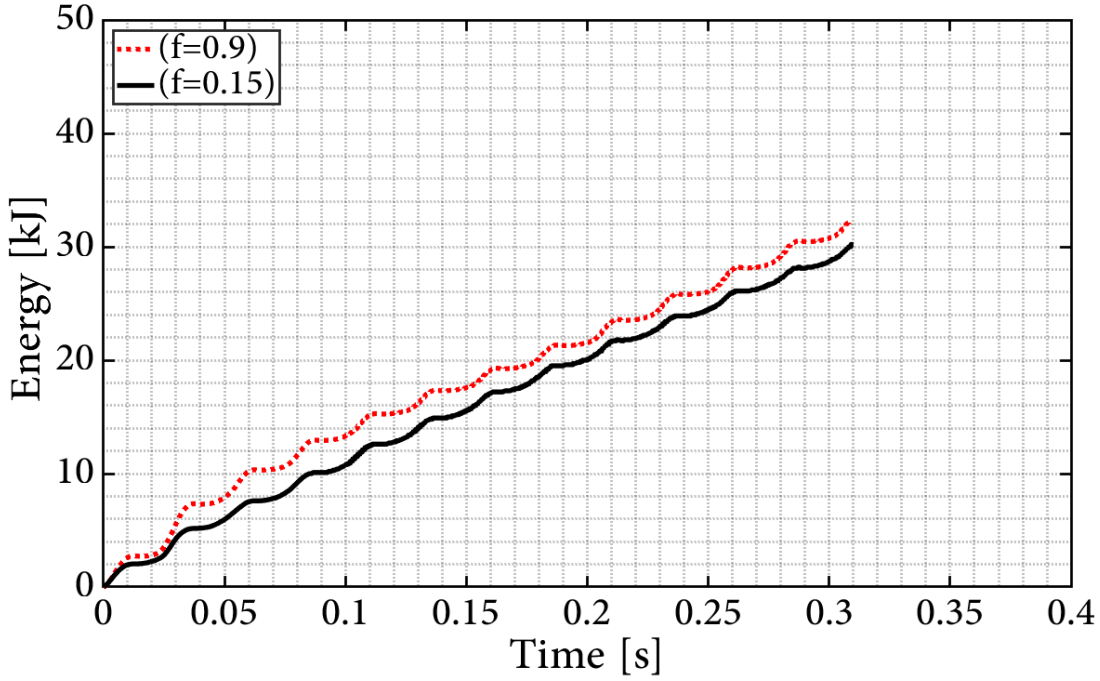

Figure 5.26. Comparison between obtained DEM results for dissipated energy over loading. The PSD is equipped with a single sphere-shaped configuration. The piston's sphere coefficient of friction is set to be 0.15 and 0.9. The applied pressure is p= 1 MPa; the amplitude u_o= 60 mm; and frequency of the cyclic loading is f_o= 20 Hz.

$$F_s = f(p, R) = \Pi_s p R^2 \tag{5.1}$$

where Π_s is a dimensionless coefficient that accounts for the spherical geometry, the Poisson effect that controls the level on normal stresses along the direction that the pressure p is exerted (against the direction of motion), and the developed mobilized normal and shear stresses from the projections on the sand-sphere interface along the direction of motion of the sphere. According to Equation 4.1, F_s is proportional to the exerted pressure p and quadratically related to the radius of the sphere, R. Dimensional analysis was employed for the quadratic dependency of the drag force, F_s, on the radius of the sphere, R, which, was proven in an experimental study by Albert et al. (2001). Accordingly, in this simulation the radius of the sphere increased by 10% in order to measure the dissipated energy of the system. The piston sphere size used in the simulations presented in the previous case 3.6 had a ratio of (D/R= 6.3) while the new piston sphere size had a ratio of (D/R= 5.696). Figure 5.27 shows the recorded piston force against displacement. By utilizing a larger sphere size by 10 %, the force capacity increases by about 24%, approximately confirming the quadratic dependence of the piston force on the radius of the piston sphere. Figure 5.28 shows the amount of dissipated energy for the two DEM simulation results where the applied pressure is p= 2 MPa; the amplitude is u_o= 60 mm; and frequency of the cyclic loading is f_o= 20 Hz. As shown in the figure the dissipated energy increased by 120% as the D/R ratios decreased by 10%.

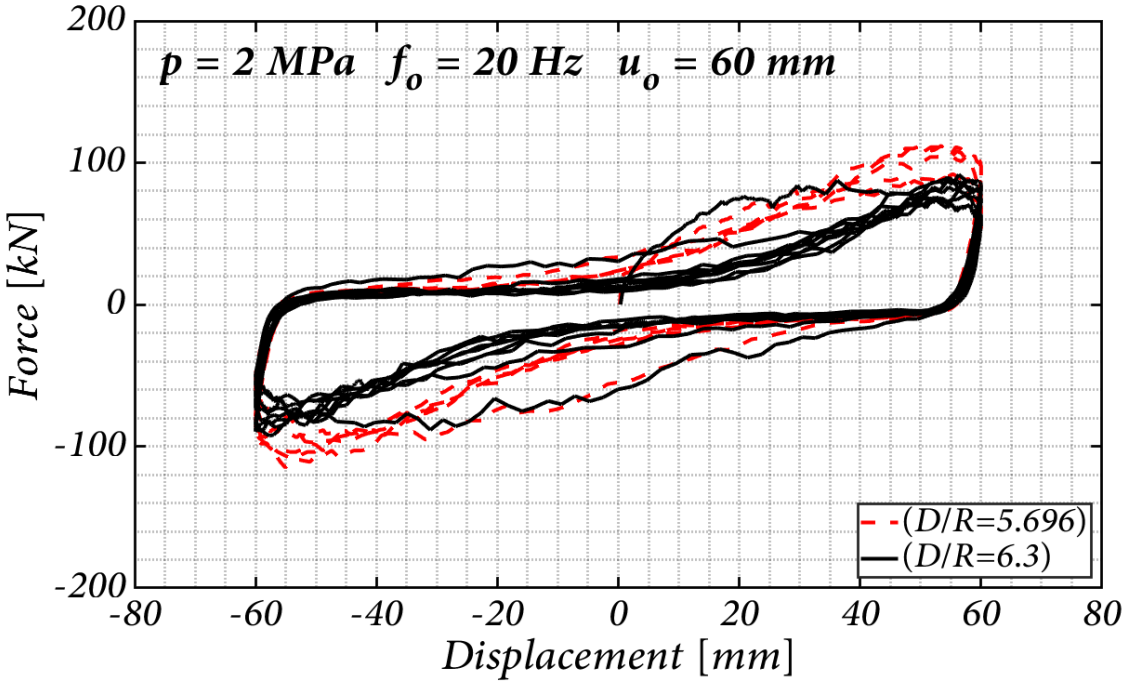

Figure 5.27. Comparison between obtained DEM results for the force versus displacement cyclic loops of PSD equipped with differing D/R ratios. The applied pressure is p= 2 MPa; the amplitude u_o= 60 mm; and frequency of the cyclic loading is f_o= 20 Hz.

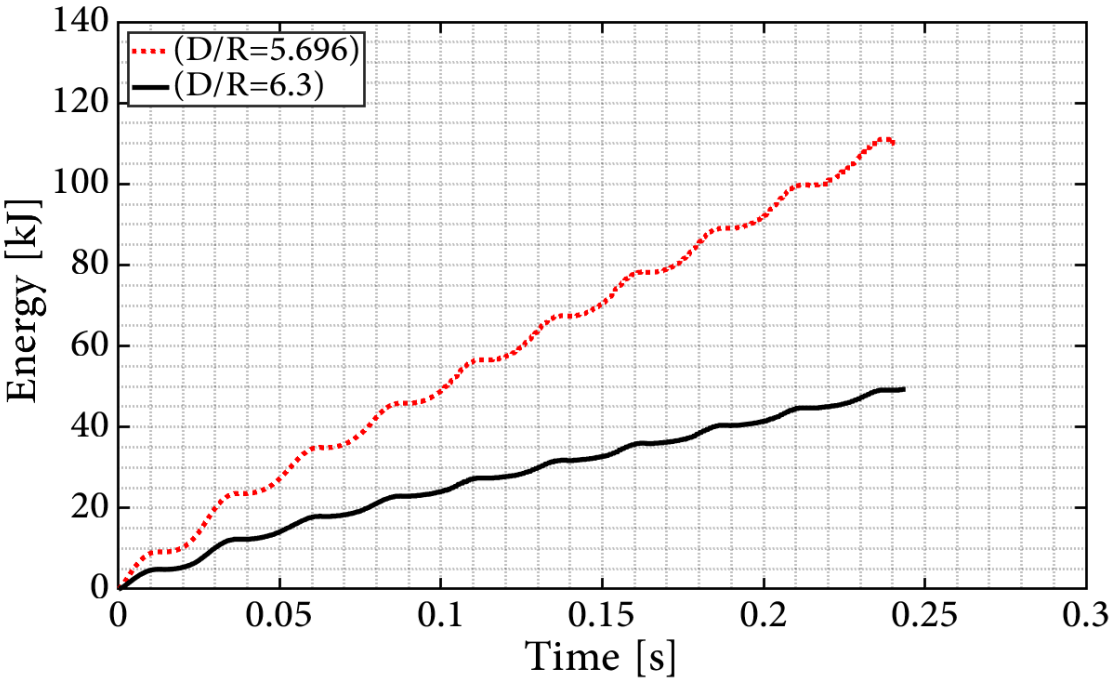

Figure 5.28. Comparison between obtained DEM results for dissipated energy over loading. The PSD is equipped with a single sphere-shaped configuration with differing D/R ratios. The applied pressure is p= 2 MPa; the amplitude is u_o= 60 mm; and frequency of the cyclic loading is f_o= 20 Hz.

5.1.3. Grain-Size Distribution

The effect of the grain size was studied to evaluate the response of the PSD under cyclic shearing by utilizing a wider range of particles (varying from 1-5 mm). These particle size variations are closer to the actual sand sizes. Figure 5.29 shows the piston force capacity for the two cases. In both DEM cases the exerted pressure is $p = 1$ MPa, the stroke amplitude is $u_o = 60$ mm, and the frequency of loading is f_o= 20 Hz. The use of a wider range of particles improved the performance of the PSD: the maximum force capacity has been increased by 19%. The dry sand exhibits a strain-hardening behavior when the piston reaches its maximum displacement. This is marked by the force-displacement curves' steeper slope, which shows soil dilation during cycling motion. In the first cycle, the same pattern is visible in both outcomes from the DEM simulations. It is important to note that the initial cyclic loop shows a more significant peak, which gradually falls during subsequent cycles. Similar observations have been reported by Makris et al. (2021). A comparison of the dissipated energy under cyclic loading is shown in Figure 5.30. It is a worthy mission that the dissipated energy increases by 187.5% when the grain size was varying from 1-5 mm as compared with 2-4 mm.

5.1.3.1. Multi-Sphere Configuration

Various sand damper configurations were considered and the behavior of the PSD was assessed using DEM simulations. The original PSD model was equipped with only a single-sphere piston configuration (Figure 3.6). Figures 5.31 and 5.32 show the schematic configu-

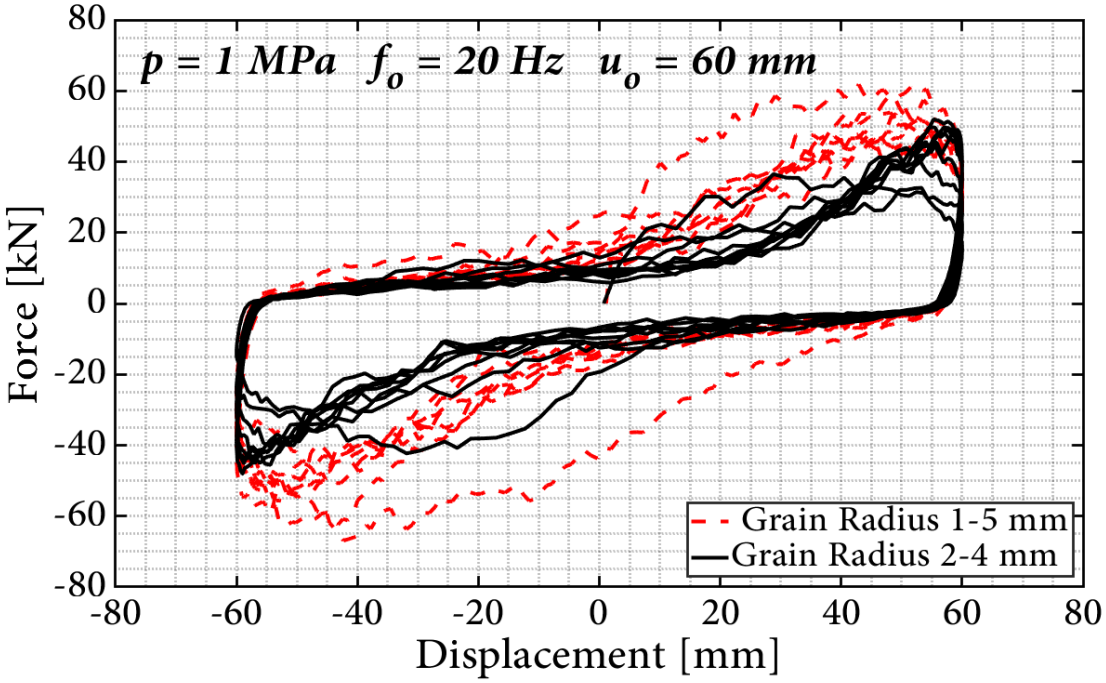

Figure 5.29. Comparison between obtained DEM results for the force versus displacement cyclic loops of PSD equipped with a single sphere-shaped configurations. The applied pressure is p= 1 MPa; the amplitude u_o= 60 mm; and frequency of the cyclic loading is f_o= 20 Hz.

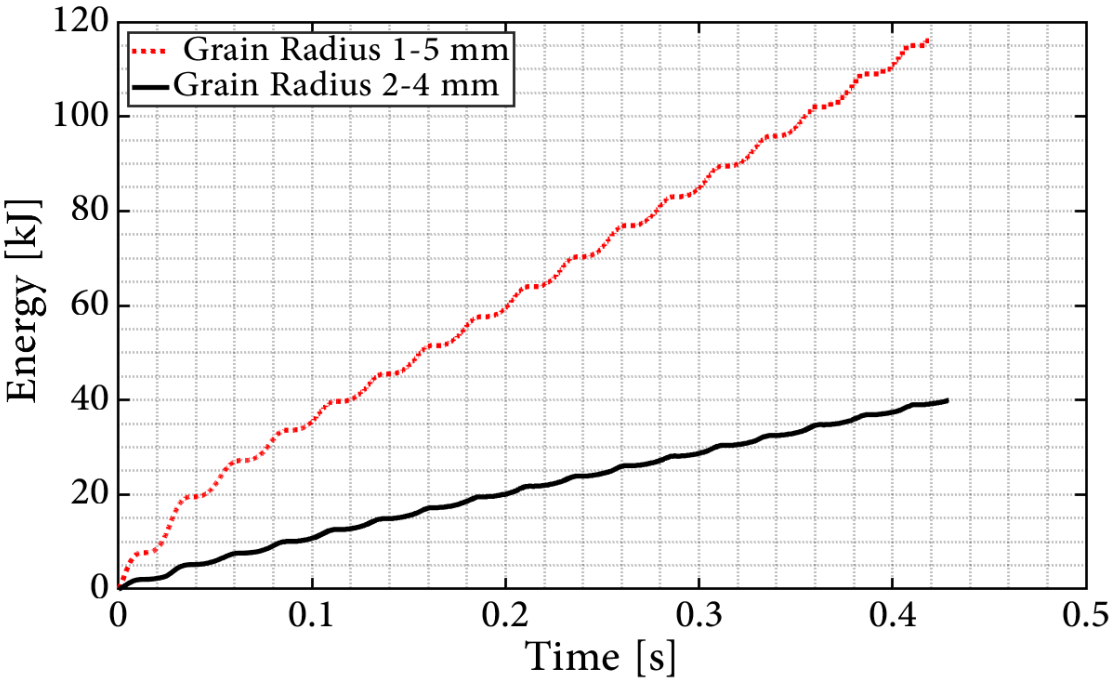

Figure 5.30. Comparison between obtained DEM results for dissipated energy over loading. The PSD is equipped with a single sphere-shaped configuration. The grain size is from 2-4 mm and 1-5 mm. The applied pressure is p= 1 MPa; the amplitude is u_o= 60 mm; and frequency of the cyclic loading is f_o= 20 Hz.

rations of the PSD utilizing the same dimensions as depicted in Figure 3.6.

In Figure 3.6, the sphere is placed in the middle of the metallic rod (origin). In the second model, the two spheres are located at distance of ± 120 mm from the origin as shown in Figure 5.31. The third model shown in Figure 5.32, one sphere is established in the origin of the sand damper and the other two spheres are at a distant of ± 120 mm. These three proposed models all have the same sphere diameter of 6 cm. The applied pressure here in all cases is p= 1 MPa and the stroke amplitude in all cases is u_o= 60 mm. Figure 5.33 shows the DEM models of configurations that included two and three spheres mounted on the piston rod.

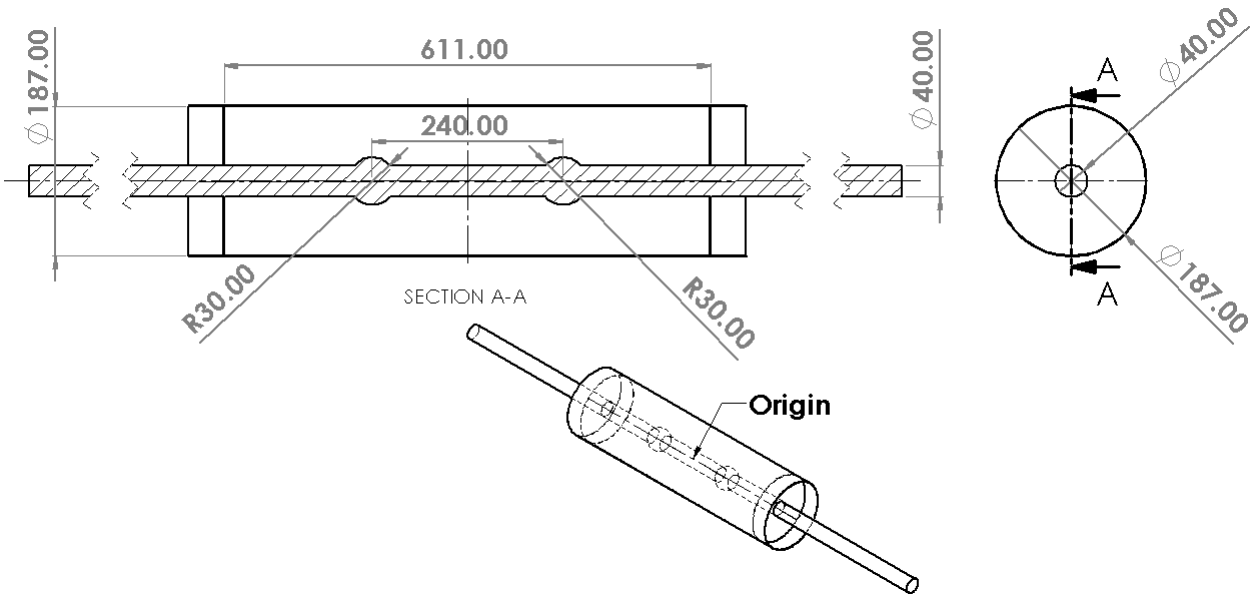

Figure 5.31. Schematic design of the pressurized sand damper model equipped with two spheres.

Figure 5.34 shows cyclic loops for the force and displacement during loading. All DEM simulation results exhibit the same pattern in the first cycle. The first cyclic loop has a

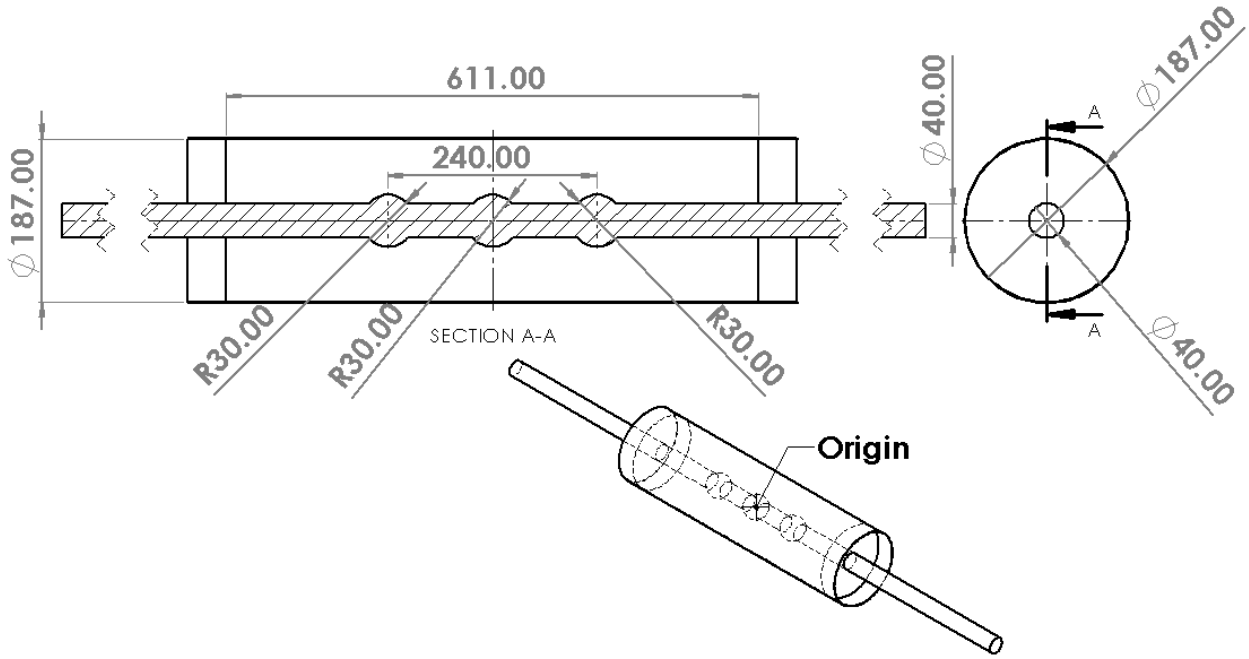

Figure 5.32. Schematic design of the pressurized sand damper model equipped with three spheres.

Figure 5.33. Different configurations of the sand damper tested numerically in DEM simulations: Left: Damper with two metal spheres appended on the piston rod; Right: Damper with three metal spheres.

higher peak which gradually decreases in the following cycles. The applied pressure here in all cases is p= 1 MPa and the stroke amplitude in all cases is u_o= 60 mm. It can be seen from Figure 5.34 when the piston is equipped with double spheres that the maximum force capacity increased by 80.6%, and with three spheres there is a 328.3% increase. The amount of the dissipated energy is the area inside the loops. The soil experiences similar behavior as in Figure 4.1 and 5.25 where a strain hardening behavior can also be noticed in both cases when the piston reaches its maximum displacement in the direction of motion. This is exhibited by the steeper slope of the force-displacement curves which indicates the soil dilative behavior during cycling motion. Figure 5.35 shows the dissipated energy of the PSD, when the piston is equipped with double spheres that the amount of dissipated energy increased by 75.91%, and with three spheres, there is a 265.27% increase.

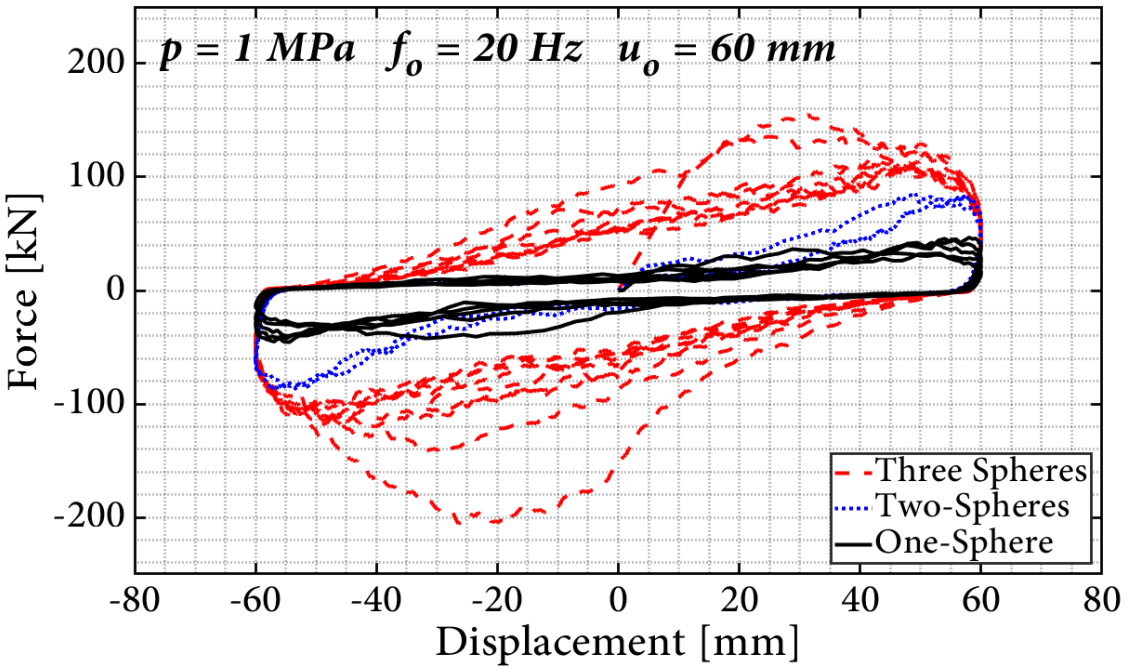

Figure 5.34. Comparison between obtained DEM results for the force versus displacement cyclic loops of PSD equipped with single, double, and triple sphere configurations. The applied pressure is p= 1 MPa; the amplitude is u_o= 60 mm; and frequency of the cyclic loading is f_o= 20 Hz.

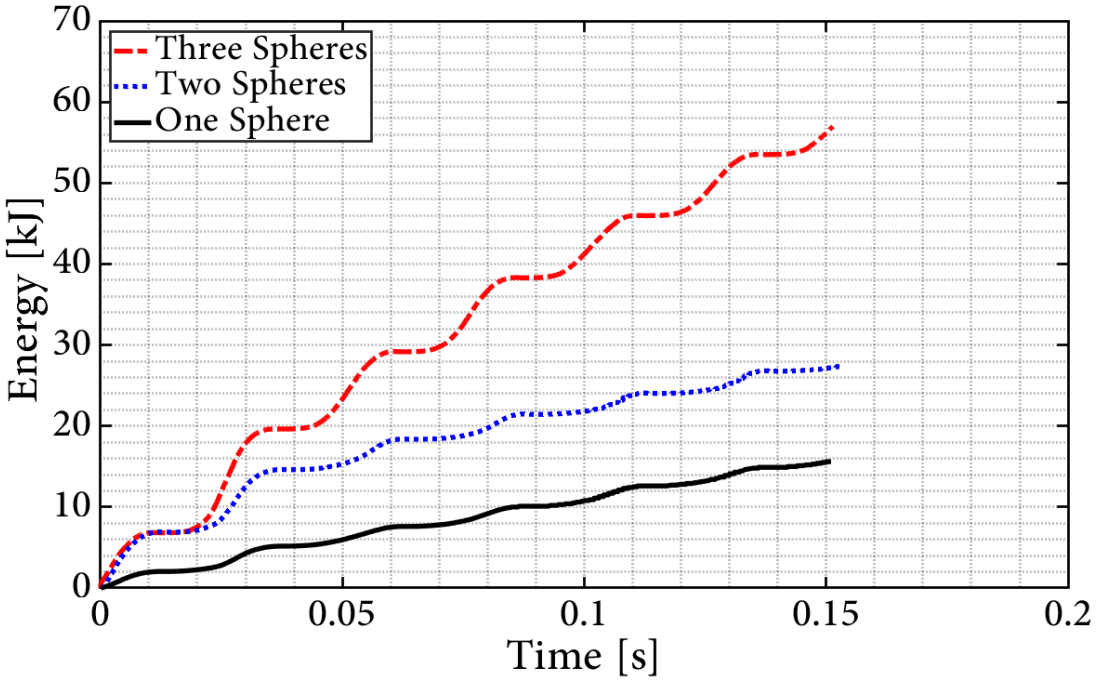

Figure 5.35. Comparison between obtained DEM results for the dissipated energy of PSD equipped with single, double, and triple sphere configurations. The applied pressure is p= 1 MPa; the amplitude is u_o= 60 mm; and frequency of the cyclic loading is f_o= 20 Hz.

5.1.4. Box-Shaped Configuration

Figure 5.36 shows the generated DEM model with a box replacing the sphere at the origin of the pressurized sand damper. Each side of the box has a length of L= 0.06 m in the first model while the second model has a length of L= 0.0484 m replacing an equivalent volume of the utilized sphere-shaped piston configuration.

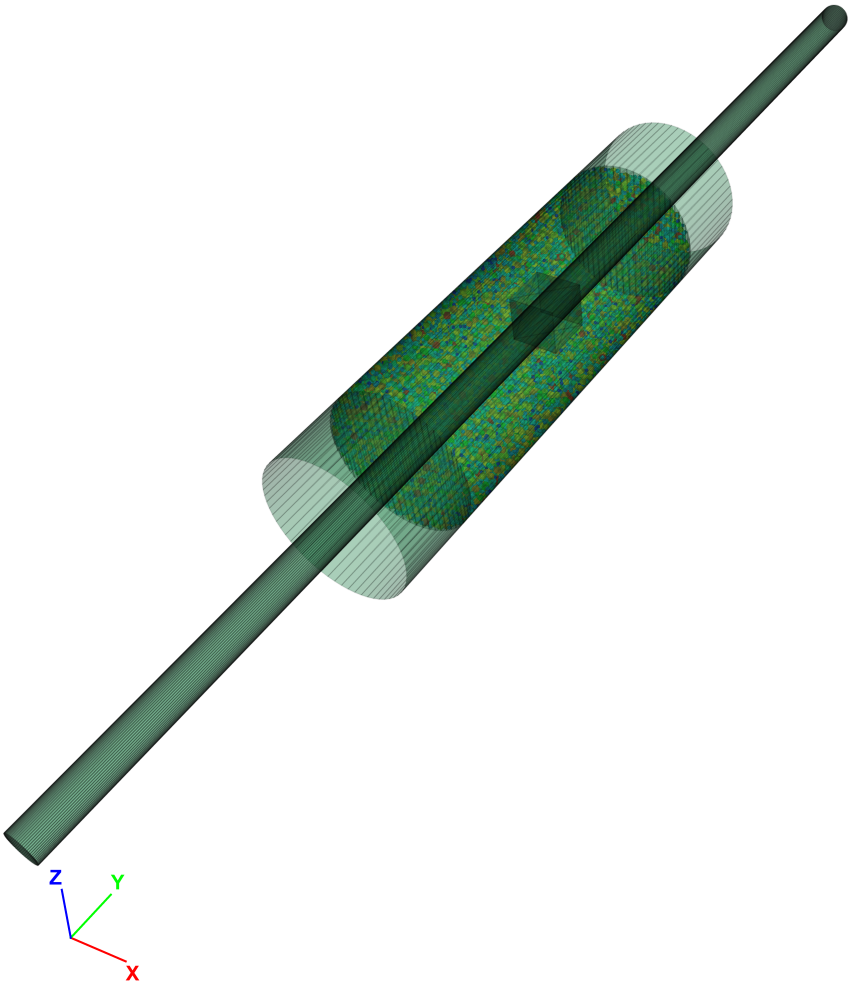

Figure 5.36. The generated DEM model of the PSD equipped with a single box-shaped configuration.

Figure 5.37 shows significant improvement of the force capacity of the pressurized sand damper compared to the sphere configuration at the same exerted pressure of p= 1 MPa and stroke amplitude of u_o= 60 mm. The magnitude of the force capacity has been increased by 189.5% when the the box length is L= 0.06 m. Another simulation was carried out when the PSD equipped with a single box to analysis the capacity of the system utilizing the equivalent volume of the a single sphere with a ratio of D/R= 6.3. The magnitude of the force capacity has been increased by 117.83%. Figure 5.38 shows a comparison for the amount of dissipated energy under cyclic loading for the conducted simulations. The amount of dissipated energy for these simulations that utilize length of the box is L= 0.06 m and L= 0.0484 m are increased by 131.48% and 111.08%, respectively over the sphere-shaped configuration with a ratio of D/R= 6.3 due to the larger surface area provided by the box-shaped configuration.

It is important to note that the projected surface area of the sphere is $A_s = \pi\ R^2$ =2827.43 mm^2, which is larger than the projected surface area of the cube, which is A_c= L $\times$ L =2342.56 mm^2 where R=30 mm and L= 48.4 mm. The amount of energy dissipated is influenced by the shape of the piston. In fact, when the PSD is equipped with a single cube, the dissipated energy increases despite the fact that the projected surface area of a single sphere is larger than the projected surface area of a single cube, as demonstrated in Figure 5.38.

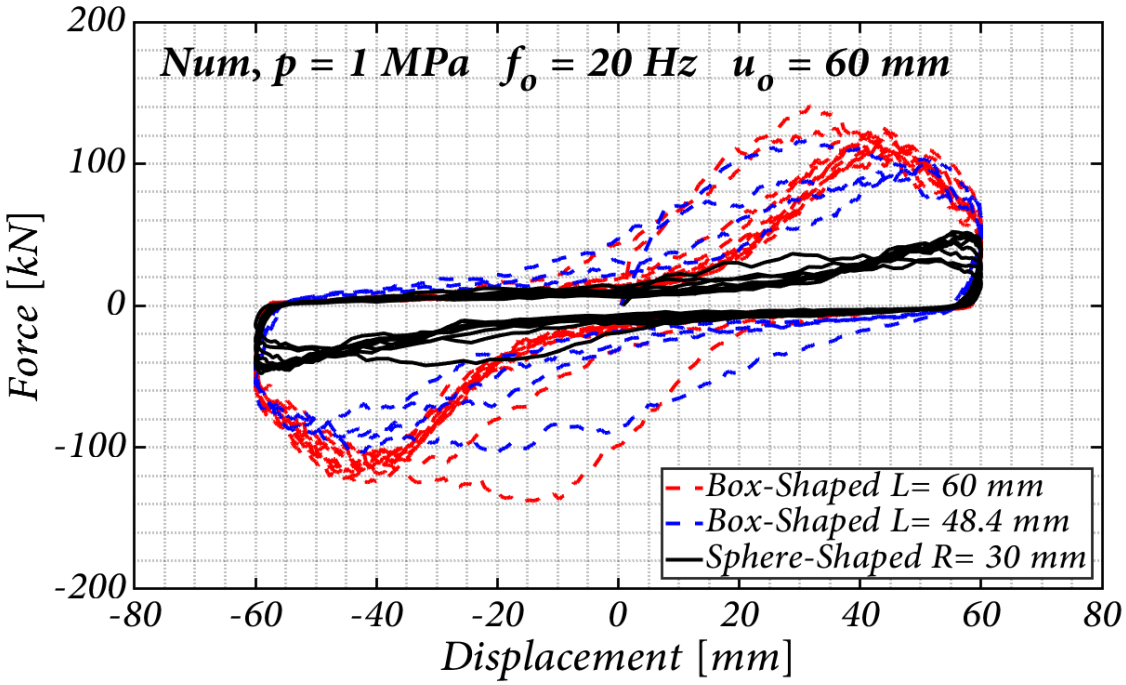

Figure 5.37. Comparison between obtained DEM results for the force versus displacement cyclic loops of PSD equipped with a single spherical-shaped and box-shaped configurations. The applied pressure is p= 1 MPa; the amplitude u_o= 60 mm; and frequency of the cyclic loading is f_o= 20 Hz.

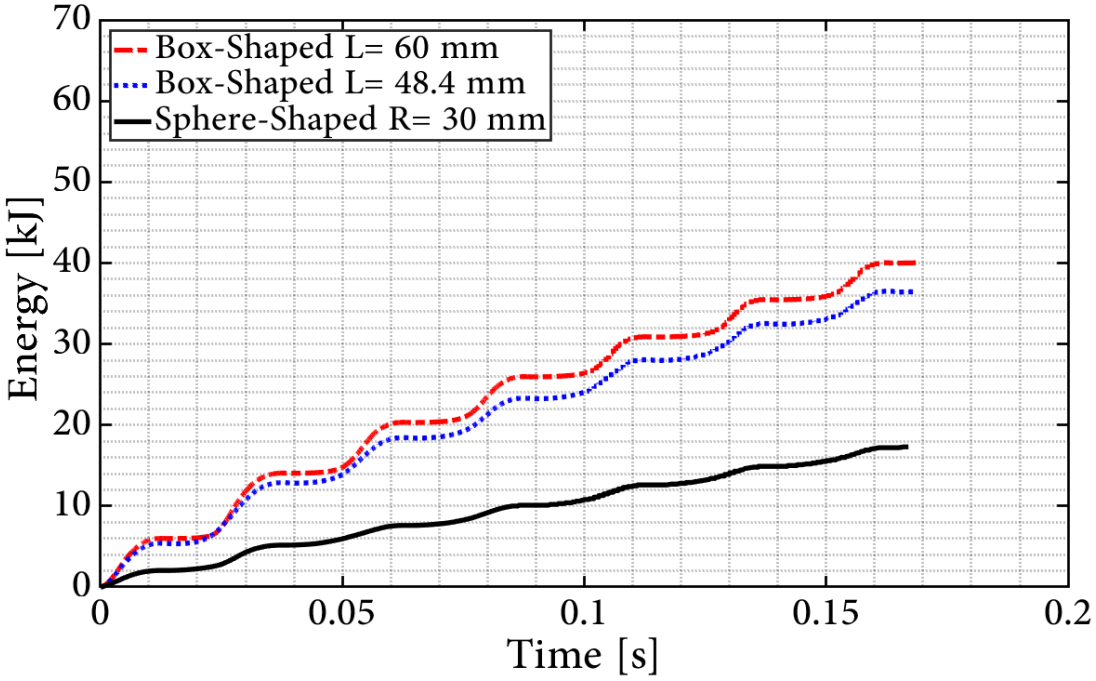

Figure 5.38. Comparison between obtained DEM results for dissipated energy over loading. The PSD is equipped with a single sphere-shaped and box-shaped configurations. The applied pressure is p= 1 MPa; the amplitude is u_o= 60 mm; and frequency of the cyclic loading is f_o= 20 Hz.

Chapter 6

CONCLUSIONS AND FUTURE RESEARCH

6.1. Conclusions

This study showed that the DEM-based approach produced results that agreed with other experiments about the impact of particle size, and particle shape. Some of the many benefits of using DEM is that the simulation technique allows the energy components to be traced easily and it helps ensure that variables can be studied in isolation by keeping all of the other features constant.

This research contained two approaches to cyclical shearing in DEM: the utilization of irregular particle shape, rather than spherical particles and the use of the linear contact model to dictate the particle interactions. These adjustments to DEM simulations of cyclical loading allow the process to be reflected more accurately, and the results of the experiment were analogous to other studies which mutually confirmed their results. This study involved performing DEM simulations of the proposed sand damper with multiple goals in mind. One of the main objectives was to produce a validated model that produces results in agreement with the experimentally measured behavior of the physical damper.

This study also aimed to perform a large number of simulations that strategically identify the effect of the parameters that were consider in these studies presented in chapter 3. In

addition, the simulations went beyond those parameters to investigate design configurations without the need to manufacture and test dampers of different scale. In this regard, the simulations present a cost-effective method compared to the manufacturing process. For instance, the configurations shown in Figure 3.7 and 3.8 were tested numerically for potential improved performance over the basic system shown in 3.6. These configurations yielded different and more efficient energy dissipation levels due do the higher friction surface areas. Furthermore, the use of multiple spheres produced a high force output; while the buckling length of the portion of the piston rod that has the highest axial force is reduced. In all simulations, the performance of the PSD is evaluated based on the amount of dissipated energy. This was quantified macroscopically through the classical force-displacement loops and by monitoring the energy dissipation mechanisms (inter-particle frictional sliding, strain energy stored at the contacts, kinetic energy, and contact viscous damping).

Upon satisfactory agreement of the analytical to the experimental results, extensive parametric studies were carried out for assessing the effect that the various parameters of the damper design have on its behavior. These simulations were performed using PFC3D Itasca (2018). Presented in this work are the results of a numerical study that utilizes discrete element method (DEM) simulations to assess the performance of pressurized sand dampers under cyclic loading. The damping effect in pressurized sand dampers originates from the sheering action of the sand and its stress-dependent shear strength. This allows for an increase in absorbed/dissipated energy in the pressurized sand during cyclic motion resulting in a reduction in excessive displacement. In the performed series of DEM simulations, stroke

amplitude, grain size distribution, the magnitude of pressure imposed on the sand, and different configurations of the pressurized sand damper were studied.

The results reveal that the main energy dissipation mechanism is generated through inter-particle frictional sliding in the sand. Additionally, the magnitude of cumulative dissipated energy increases with the pressure level applied to the sand damper, as well as with the stroke amplitude of the loading. The results suggest that when the piston was equipped with multi spheres , the maximum forces capacity has been increased significantly. The soil exhibits behavior similar to that of the case of one sphere in which a strain hardening behavior was noticed. A noticeable increase in the piston capacity was observed when the sphere size was increased by 10% and the rest of the response patterns remained unchanged. By increasing the sphere friction, the piston capacity remains nearly identical. When a wider range of particle sizes was employed, the maximum force capacity increased considerably and the amount of dissipated energy significantly increased. A significant improvement in the performance of the PSD was observed when it was equipped with a single box instead of a sphere. The capacity of the piston increased significantly as well as the dissipated energy. The results of the conducted simulations were quantitatively compared and fairly agreed with experimental data obtained from physical modeling of a similar pressurized sand damper. The proposed sand damper model is shown to be a promising device that mitigates vibrations in structural systems subject to seismic and wind loading.

6.2. Future Research

As the use of a single cubed-shaped mounted on the piston has shown higher energy dissipation compared to its spherical counterpoint, the use of multiple cubic-shaped configuration may produce a high force output; while the buckling length of the portion of the piston rod that has the highest axial force is reduced.

The performance of the pressurized sand damper needs to be examined in the case of having wet sand. A study conducted by Liefferink et al. (2020) investigated the effect of adding small amounts of water on the sliding friction on the sand and discovered that adding small amounts of water can reduce the friction coefficient by nearly a factor of two and increases the sand hardness. Adding more water to the sand reduces its hardness and increases friction. This inverse relationship between the hardness of a wetted granular material and its frictional response to sliding is attributed to sled plowing.

Particle crushing over the life of the damper is another important factor to study as contact forces in the bottleneck zone between the metal sphere and the enclosure might be extremely high. Two approaches could be considered. The first (and more popular) approach could be to model the sand particles as agglomerates created by joining smaller fundamental particles with strength-limiting bonding contacts. Once the inter-particles contact stress exceeds the bond strength, the fundamental particle breaks (Robertson and Bolton, 2001; McDowell and Harireche, 2002; Cheng et al., 2003; Bolton et al., 2008; Cil and Alshibli, 2012; Wang and Yan, 2013).

The second approach characterizes the fundamental particle itself and marks it a failed particle if a prescribed strength measure is exceeded (Hanley et al., 2015). Both approaches could be considered depending on the resulting computational time.

Bibliography

(2022). "Fluid Viscous Dampers Can Protect Your Structure taylordevices inc., <http://https://www.taylordevices.com/products/fluid-viscous-dampers/>.

Abbas, H., Hai, H., Rongong, J., and Xing, Y. (2014). "Damping performance of metal swarfs in a horizontal hollow structure." *Journal of Mechanical Science and Technology*, 28(1), 9–13.

Agency, F. E. M. (2006). *Techniques for the seismic rehabilitation of existing buildings*. FEMA.

Albert, I., Sample, J., Morss, A., Rajagopalan, S., Barabási, A.-L., and Schiffer, P. (2001). "Granular drag on a discrete object: Shape effects on jamming." *Physical Review E*, 64(6), 061303.

Asher, J. W., Young, R. P., and Ewing, R. D. (1996). "Seismic isolation design of the san bernardino county medical center replacement project." *The Structural Design of Tall Buildings*, 5(4), 265–279.

Bannerman, M. N., Kollmer, J. E., Sack, A., Heckel, M., Mueller, P., and Pöschel, T. (2011). "Movers and shakers: Granular damping in microgravity." *Physical Review E*, 84(1), 011301.

Bapat, C. (1998). "Periodic motions of an impact oscillator." *Journal of Sound and Vibration*, 209(1), 43–60.

Bapat, C. and Sankar, S. (1985a). "Multiunit impact damper—re-examined." *Journal of Sound and Vibration*, 103(4), 457–469.

Bapat, C. and Sankar, S. (1985b). "Single unit impact damper in free and forced vibration." *Journal of Sound and Vibration*, 99(1), 85–94.

Bardet, J. and Huang, Q. (1992). "Numerical modeling of micropolar effects in idealized granular materials." *Mechanics of Granular Materials and Powder Systems*, 37, 85–91.

Barenblatt, G. I., Barenblatt, G. I., and Isaakovich, B. G. (1996). *Scaling, self-similarity, and intermediate asymptotics: dimensional analysis and intermediate asymptotics*. Number 14. Cambridge University Press.

Bathurst, R. J. and Rothenburg, L. (1988). "Micromechanical aspects of isotropic granular assemblies with linear contact interactions.

Bergeot, B., Bellizzi, S., and Cochelin, B. (2017). "Passive suppression of helicopter ground resonance using nonlinear energy sinks attached on the helicopter blades." *Journal of Sound and Vibration*, 392, 41–55.

Black, C., Aiken, I. D., and Makris, N. (2002). *Component testing, stability analysis, and characterization of buckling-restrained unbonded braces (TM)*. Pacific Earthquake Engineering Research Center.

Black, C., Makris, N., and Aiken, I. (2018). "Component testing and modeling of buckling restrained "unbonded" braces." *Stessa 2003*, Routledge, 141–145.

Black, C. J., Makris, N., and Aiken, I. D. (2004). "Component testing, seismic evaluation and characterization of buckling-restrained braces." *Journal of Structural Engineering*, 130(6), 880–894.

Bolton, M., Nakata, Y., and Cheng, Y. (2008). "Micro-and macro-mechanical behaviour of dem crushable materials." *Géotechnique*, 58(6), 471–480.

BRIDGESTONESolutionsforyourjourney (2022). "Seismic isolation system, <http://https://www.bridgestone.com/products/diversified/antiseismic˙rubber/principle.html>.

Buckle, I. G. and Mayes, R. L. (1990). "Seismic isolation: history, application, and performance—a world view." *Earthquake spectra*, 6(2), 161–201.

Buckle Ian, G. and Ian, M. F. (1995). "Seismic retrofitting manual for highway bridges. federal highway administration, us department of transportation. publication no." *Report no.*, FHWA-RD-94-052, McLean, Virginia.

Buss, S. R. (2000). "Accurate and efficient simulation of rigid-body rotations." *Journal of Computational Physics*, 164(2), 377–406.

Bustamante, M., Gerges, S. N., Cordioli, J., Martin, O. P., Weisbeck, J., and Ott, M. (2013). "Experimental study on some parameters that affect the performance of an elastomer particle damper." *Proceedings of Meetings on Acoustics ICA2013*, Vol. 19, Acoustical Society of America, 065020.

Campbell, C. S. and Brennen, C. E. (1985). "Computer simulation of granular shear flows." *Journal of Fluid Mechanics*, 151, 167–188.

Cates, M., Wittmer, J., Bouchaud, J.-P., and Claudin, P. (1998). "Jamming, force chains, and fragile matter." *Physical Review Letters*, 81(9), 1841.

Chen, L. and Semercigil, S. (1993). "A beam-like damper for attenuating transient vibrations of light structures." *Journal of Sound and Vibration*, 164(1), 53–65.

Chen, T., Mao, K., Huang, X., and Wang, M. Y. (2001). "Dissipation mechanisms of nonobstructive particle damping using discrete element method." *Smart Structures and Materials 2001: Damping and Isolation*, Vol. 4331, International Society for Optics and Photonics, 294–301.

Cheng, Y., Nakata, Y., and Bolton, M. D. (2003). "Discrete element simulation of crushable soil." *Geotechnique*, 53(7), 633–641.

Cil, M. and Alshibli, K. (2012). "3d assessment of fracture of sand particles using discrete element method." *Géotechnique Letters*, 2(3), 161–166.

Constantinou, M. C., Soong, T. T., and Dargush, G. F. (1998). "Passive energy dissipation systems for structural design and retrofit.

Cundall, P. A. (1971). "A computer model for simulating progressive, large-scale movement in blocky rock system." *Proceedings of the International Symposium on Rock Mechanics, 1971.*

Cundall, P. A. (2001). "A discontinuous future for numerical modelling in geomechanics?." *Proceedings of the Institution of Civil Engineers-Geotechnical Engineering*, 149(1), 41–47.

Cundall, P. A. and Strack, O. D. (1979). "A discrete numerical model for granular assemblies." *Geotechnique*, 29(1), 47–65.

Darabi, B. and Rongong, J. (2012). "Polymeric particle dampers under steady-state vertical vibrations." *Journal of Sound and Vibration*, 331(14), 3304–3316.

Davenport, A. (1967). "The treatment of wind loading on tall buildings." *Tall Buildings*, Elsevier, 3–45.

Dobry, R. and NG, T.-T. (1992). "Discrete modelling of stress-strain behaviour of granular media at small and large strains." *Engineering Computations.*

Du, Y. and Wang, S. (2010). "Modeling the fine particle impact damper." *International Journal of Mechanical Sciences*, 52(7), 1015–1022.

Duncan, M., Wassgren, C., and Krousgrill, C. (2005). "The damping performance of a single particle impact damper." *Journal of Sound and Vibration*, 286(1-2), 123–144.

El Shamy, U. and Aydin, F. (2008). "Multiscale modeling of flood-induced piping in river levees." *Journal of Geotechnical and Geoenvironmental Engineering*, 134(9), 1385–1398.

El Shamy, U. and Zeghal, M. (2005). "Coupled continuum-discrete model for saturated granular soils." *Journal of Engineering Mechanics*, 131(4), 413–426.

Ema, S. and Marui, E. (1994). "A fundamental study on impact dampers." *International Journal of Machine Tools and Manufacture*, 34(3), 407–421.

Evans, T. M. and Frost, J. D. (2010). "Multiscale investigation of shear bands in sand: physical and numerical experiments." *International Journal for Numerical and Analytical Methods in Geomechanics*, 34(15), 1634–1650.

Fadel Miguel, L. F., Lopez, R. H., Miguel, L. F. F., and Torii, A. J. (2016). "A novel approach to the optimum design of mtmds under seismic excitations." *Structural Control and Health Monitoring*, 23(11), 1290–1313.

Fang, X. and Tang, J. (2006). "Granular damping in forced vibration: qualitative and quantitative analyses.

Fang, X., Tang, J., and Luo, H. (2007). "Granular damping analysis using an improved discrete element approach." *Journal of Sound and Vibration*, 308(1-2), 112–131.

FEMA, B. (2000). "Prestandard and commentary for the seismic rehabilitation of buildings.

Fiore, A., Marano, G. C., and Natale, M. G. (2016). "Theoretical prediction of the dynamic behavior of rolling-ball rubber-layer isolation systems." *Structural Control and Health Monitoring*, 23(9), 1150–1167.

Foti, D., Diaferio, M., and Nobile, R. (2013). "Dynamic behavior of new aluminum–steel energy dissipating devices." *Structural Control and Health Monitoring*, 20(7), 1106–1119.

Fowler, B. L., Flint, E. M., and Olson, S. E. (2000). "Effectiveness and predictability of particle damping." *Smart Structures and Materials 2000: Damping and Isolation*, Vol. 3989, International Society for Optics and Photonics, 356–367.

Friend, R. D. and Kinra, V. (2000). "Particle impact damping." *Journal of sound and vibration*, 233(1), 93–118.

Gates, M., Wittmer, J., Bouchaud, J.-P., and Claudin, P. (1999). "Jamming and stress propagation in particulate matter." *Physica A: Statistical Mechanics and its Applications*, 263(1-4), 354–361.

Gharib, M. and Ghani, S. (2013). "Free vibration analysis of linear particle chain impact damper." *Journal of Sound and Vibration*, 332(24), 6254–6264.

Goldhirsch, I. (2003). "Rapid granular flows." *Annual Review of Fluid Mechanics*, 35(1), 267–293.

Gourc, E., Seguy, S., Michon, G., Berlioz, A., and Mann, B. (2015). "Quenching chatter instability in turning process with a vibro-impact nonlinear energy sink." *Journal of Sound and Vibration*, 355, 392–406.

Grest, G. S., Dünweg, B., and Kremer, K. (1989). "Vectorized link cell fortran code for molecular dynamics simulations for a large number of particles." *Computer Physics Communications*, 55(3), 269–285.

Grubin, C. (1956). "On the theory of the acceleration damper.

Halperin, I., Ribakov, Y., and Agranovich, G. (2016). "Optimal viscous dampers gains for structures subjected to earthquakes." *Structural Control and Health Monitoring*, 23(3), 458–469.

Hanes, D. M. and Walton, O. R. (2000). "Simulations and physical measurements of glass spheres flowing down a bumpy incline." *Powder Technology*, 109(1-3), 133–144.

Hanley, K. J., O'Sullivan, C., and Huang, X. (2015). "Particle-scale mechanics of sand crushing in compression and shearing using dem." *Soils and Foundations*, 55(5), 1100–1112.

Hardin, B. O. and Drnevich, V. P. (1972). "Shear modulus and damping in soils: design equations and curves." *Journal of the Soil mechanics and Foundations Division*, 98(7), 667–692.

Heckel, M., Sack, A., Kollmer, J. E., and Pöschel, T. (2012). "Granular dampers for the reduction of vibrations of an oscillatory saw." *Physica A: Statistical Mechanics and its Applications*, 391(19), 4442–4447.

Hollkamp, J. J. and Gordon, R. W. (1998). "Experiments with particle damping." *Smart structures and materials 1998: Passive damping and isolation*, Vol. 3327, SPIE, 2–12.

Itasca (2018). "Pfc3d (particle flow code in 3 dimensions)." *version 6.0.*, Minneapolis: ICG.

Iwashita, K. and Oda, M. (1998). "Rolling resistance at contacts in simulation of shear band development by dem." *Journal of Engineering Mechanics*, 124(3), 285–292.

Izadi, E. and Bezuijen, A. (2015). "Simulation of granular soil behaviour using the bullet physics library." *3rd International Symposium on Geomechanics from Micro to Macro*, Vol. 2, Taylor and Francis Group-London, 1565–1570.

Izadi, E. and Bezuijen, A. (2018). "Simulating direct shear tests with the bullet physics library: A validation study." *PLOS one*, 13(4), e0195073.

Jiang, M., Yu, H.-S., and Harris, D. (2006). "Discrete element modelling of deep penetration in granular soils." *International Journal for Numerical and Analytical Methods in Geomechanics*, 30(4), 335–361.

Johnson, S. M., Williams, J. R., and Cook, B. K. (2008). "Quaternion-based rigid body rotation integration algorithms for use in particle methods." *International Journal for Numerical Methods in Engineering*, 74(8), 1303–1313.

Jop, P., Forterre, Y., and Pouliquen, O. (2006). "A constitutive law for dense granular flows." *Nature*, 441(7094), 727–730.

Kareem, A. and Gurley, K. (1996). "Damping in structures: its evaluation and treatment of uncertainty." *Journal of wind Engineering and Industrial Aerodynamics*, 59(2-3), 131–157.

Kareem, A., Kijewski, T., and Tamura, Y. (1999). "Mitigation of motions of tall buildings with specific examples of recent applications." *Wind and Structures*, 2(3), 201–251.

Kawamoto, R., Andò, E., Viggiani, G., and Andrade, J. E. (2018). "All you need is shape: predicting shear banding in sand with ls-dem." *Journal of the Mechanics and Physics of Solids*, 111, 375–392.

Kelly, J. M. (1986). "Aseismic base isolation: review and bibliography." *Soil Dynamics and Earthquake Engineering*, 5(4), 202–216.

Kelly, J. M. and Konstantinidis, D. (2011). *Mechanics of rubber bearings for seismic and vibration isolation*. John Wiley & Sons.

Kelly, J. M., Skinner, R., and Heine, A. (1972). "Mechanisms of energy absorption in special devices for use in earthquake resistant structures." *Bulletin of the New Zealand Society for Earthquake Engineering*, 5(3), 63–88.

Kerwin Jr, E. (1965). "Macromechanisms of damping in composite structure. internal friction, damping, and cyclic plasticity.

Konstantinidis, D., Makris, N., and Kelly, J. M. (2015). "In-situ condition assessment of seismic fluid dampers: experimental studies and challenges." *Meccanica*, 50(2), 323–340.

Kuhn, M. R. and Mitchell, J. K. (1992). "Modelling of soil creep with the discrete element method." *Engineering Computations*.

Lai, C. G. (1998). *Simultaneous inversion of Rayleigh phase velocity and attenuation for near-surface site characterization*. Georgia Institute of Technology.

Langhaar, H. L. (1962). "Dimensional analysis and theory of models." *Report no.*

Lee, S. J. and Hashash, Y. M. (2015). "idem: An impulse-based discrete element method for fast granular dynamics." *International Journal for Numerical Methods in Engineering*, 104(2), 79–103.

Lee, Y., Vakakis, A. F., Bergman, L., McFarland, D., Kerschen, G., Nucera, F., Tsakirtzis, S., and Panagopoulos, P. (2008). "Passive non-linear targeted energy transfer and its applications to vibration absorption: a review." *Proceedings of the Institution of Mechanical Engineers, Part K: Journal of Multi-body Dynamics*, 222(2), 77–134.

Lenzi, A. (1985). "The use of damping material in industrial machines." Ph.D. thesis, University of Southampton, University of Southampton.

Li, H., Zhang, P., Song, G., Patil, D., and Mo, Y. (2015). "Robustness study of the pounding tuned mass damper for vibration control of subsea jumpers." *Smart Materials and Structures*, 24(9), 095001.

Li, K. and Darby, A. P. (2008). "A buffered impact damper for multi-degree-of-freedom structural control." *Earthquake Engineering & Structural Dynamics*, 37(13), 1491–1510.

Lieber, P., Jensen, D., et al. (1945). "An acceleration damper: development, design and some applications." *Trans. ASME*, 67(10), 523–530.

Liefferink, R. W., Aliasgari, M., Maleki-Jirsaraei, N., Rouhani, S., and Bonn, D. (2020). "Sliding on wet sand." *Granular Matter*, 22(3), 1–6.

Lim, K.-W. and Andrade, J. E. (2014). "Granular element method for three-dimensional discrete element calculations." *International Journal for Numerical and Analytical Methods in Geomechanics*, 38(2), 167–188.

Liu, A. J. and Nagel, S. R. (1998). "Jamming is not just cool any more." *Nature*, 396(6706), 21–22.

Liu, W., Tomlinson, G., and Rongong, J. (2005). "The dynamic characterisation of disk geometry particle dampers." *Journal of Sound and Vibration*, 280(3-5), 849–861.

Lu, O. "design and experimental verification of track nonlinear energy sink for vibration control under seismic excitation, struct." *Control Health Monit*, (24).

Lu, Z., Chen, X., Li, X., and Li, P. (2017a). "Optimization and application of multiple tuned mass dampers in the vibration control of pedestrian bridges." *Structural Engineering and Mechanics: An international journal*, 62(1), 55–64.

Lu, Z., Chen, X., Zhang, D., and Dai, K. (2017b). "Experimental and analytical study on the performance of particle tuned mass dampers under seismic excitation." *Earthquake Engineering & Structural Dynamics*, 46(5), 697–714.

Lu, Z., Lu, X., and Masri, S. F. (2010). "Studies of the performance of particle dampers under dynamic loads." *Journal of Sound and Vibration*, 329(26), 5415–5433.

Lu, Z., Masri, S. F., and Lu, X. (2011a). "Parametric studies of the performance of particle dampers under harmonic excitation." *Structural Control and Health Monitoring*, 18(1), 79–98.

Lu, Z., Masri, S. F., and Lu, X. (2011b). "Studies of the performance of particle dampers attached to a two-degrees-of-freedom system under random excitation." *Journal of Vibration and Control*, 17(10), 1454–1471.

Lu, Z., Wang, D., Masri, S. F., and Lu, X. (2016). "An experimental study of vibration control of wind-excited high-rise buildings using particle tuned mass dampers." *Smart Struct. Syst*, 18(1), 93–115.

Lu, Z., Wang, Z., Masri, S. F., and Lu, X. (2018). "Particle impact dampers: Past, present, and future." *Structural Control and Health Monitoring*, 25(1), e2058.

Makris, N. (2019). "Seismic isolation: Early history." *Earthquake Engineering & Structural Dynamics*, 48(2), 269–283.

Makris, N. and Black, C. J. (2003). *Dimensional analysis of inelastic structures subjected to near fault ground motions*. Earthquake Engineering Research Center, University of California Berkeley ....

Makris, N. and Black, C. J. (2004). "Dimensional analysis of rigid-plastic and elastoplastic structures under pulse-type excitations." *Journal of Engineering Mechanics*, 130(9), 1006–1018.

Makris, N., Palios, X., Moghimi, G., and Bousias, S. (2021). "Pressurized sand damper for earthquake and wind engineering: Design, testing, and characterization." *Journal of Engineering Mechanics*, 147(4), 04021014.

Mao, K., Wang, M. Y., Xu, Z., and Chen, T. (2004). "Simulation and characterization of particle damping in transient vibrations." *J. Vib. Acoust.*, 126(2), 202–211.

Martin, T., Huntley, J., and Wildman, R. (2005). "Hydrodynamic model for a vibrofluidized granular bed." *Journal of Fluid Mechanics*, 535, 325–345.

Masmoudi, M., Job, S., Abbes, M. S., Tawfiq, I., and Haddar, M. (2016). "Experimental and numerical investigations of dissipation mechanisms in particle dampers." *Granular Matter*, 18(3), 1–11.

Masri, S. (1967a). "Effectiveness of two-particle impact dampers." *The Journal of the Acoustical Society of America*, 41(6), 1553–1554.

Masri, S. (1967b). "Motion and stability of two-particle, single-container impact dampers.

Masri, S. (1970). "General motion of impact dampers." *The Journal of the Acoustical Society of America*, 47(1B), 229–237.

Masri, S. (1972). "Theory of the dynamic vibration neutralizer with motion-limiting stops." *Journal of Applied Mechanics*, 39(2), 563–568.

Masri, S. and Kahyai, K. (1974). "Steady-state motion of a plate with a discontinuous mass." *International Journal of Non-Linear Mechanics*, 9(6), 451–462.

Masri, S. F. (1969). "Analytical and experimental studies of multiple-unit impact dampers." *The Journal of the Acoustical Society of America*, 45(5), 1111–1117.

Masri, S. F. (1973). "Forced vibration of class of nonlinear dissipative beams." *Journal of the Engineering Mechanics Division*, 99(4), 669–683.

Matier, P. and Ross, A. (2013). "Bay bridge shock absorbers spring leak." *San Francisco Chronicle*, 20.

McDowell, G. and Harireche, O. (2002). "Discrete element modelling of yielding and normal compression of sand." *Géotechnique*, 52(4), 299–304.

McNamara, R. J., Boggs, D. W., Lai, M.-L., Makris, N., Nielsen, E. J., and Cermak, J. E. (1997). "Tailoring of damping in structures: Design issues." *Building to Last*, ASCE, 1073–1077.

Michon, G., Almajid, A., and Aridon, G. (2013). "Soft hollow particle damping identification in honeycomb structures." *Journal of Sound and Vibration*, 332(3), 536–544.

Miguel, L. F. F., Miguel, L. F. F., and Lopez, R. H. (2014). "Robust design optimization of friction dampers for structural response control." *Structural Control and Health Monitoring*, 21(9), 1240–1251.

Miranda, J. C. (2016). "Discussion of system intrinsic parameters of tuned mass dampers used for seismic response reduction." *Structural Control and Health Monitoring*, 23(2), 349–368.

Mishra, B. and Murty, C. (2001). "On the determination of contact parameters for realistic dem simulations of ball mills." *Powder Technology*, 115(3), 290–297.

Misra, A. and Jiang, H. (1997). "Measured kinematic fields in the biaxial shear of granular materials." *Computers and Geotechnics*, 20(3-4), 267–285.

Miyamoto, H. and Scholl, R. E. (1997). "Design of steel pyramid using seismic dampers." *Building to Last*, ASCE, 1466–1470.

Moore, J. J., Palazzolo, A., Gadangi, R., Nale, T., Klusman, S., Brown, G., and Kascak, A. (1995). "A forced response analysis and application of impact dampers to rotordynamic vibration suppression in a cryogenic environment.

Naeim, F., Lew, M., Carpenter, L. D., Youssef, N. F., Rojas, F., Saragoni, G. R., and Adaros, M. S. (2011). "Performance of tall buildings in santiago, chile during the 27 february 2010 offshore maule, chile earthquake." *The Structural Design of Tall and Special Buildings*, 20(1), 1–16.

Nedderman, R. M. et al. (1992). *Statics and kinematics of granular materials*, Vol. 352. Cambridge University Press Cambridge.

Ng, T.-T. (2004). "Macro-and micro-behaviors of granular materials under different sample preparation methods and stress paths." *International Journal of Solids and Structures*, 41(21), 5871–5884.

Ogawa, K., Ide, T., and Saitou, T. (1997). "Application of impact mass damper to a cable-stayed bridge pylon." *Journal of Wind Engineering and Industrial Aerodynamics*, 72, 301–312.

Ohtsuki, T. and Ohsawa, T. (2003). "Hydrodynamics for convection in vibrating beds of cohesionless granular materials." *Journal of the Physical Society of Japan*, 72(8), 1963–1967.

Ong, C. J. and Gilbert, E. G. (1997). "The gilbert-johnson-keerthi distance algorithm: A fast version for incremental motions." *Proceedings of International Conference on Robotics and Automation*, Vol. 2, IEEE, 1183–1189.

O'Sullivan, C. (2011). "Particle-based discrete element modeling: geomechanics perspective." *International Journal of Geomechanics*, 11(6), 449–464.

O'Sullivan, C. and Bray, J. D. (2003). "Modified shear spring formulation for discontinuous deformation analysis of particulate media." *Journal of Engineering Mechanics*, 129(7), 830–834.

Paget, A. (1937). "Vibration in steam turbine buckets and damping by impacts." *Engineering*, 143, 305–307.

Panossian, H. (1992). "Structural damping enhancement via non-obstructive particle damping technique.

Papalou, A. and Masri, S. (1996a). "Performance of particle dampers under random excitation.

Papalou, A. and Masri, S. (1996b). "Response of impact dampers with granular materials under random excitation." *Earthquake Engineering & Structural Dynamics*, 25(3), 253–267.

Papalou, A. and Masri, S. (1998). "An experimental investigation of particle dampers under harmonic excitation." *Journal of Vibration and Control*, 4(4), 361–379.

Popplewell, N. and Semercigil, S. (1989). "Performance of the bean bag impact damper for a sinusoidal external force." *Journal of Sound and Vibration*, 133(2), 193–223.

Pytlos, M., Gilbert, M., and Smith, C. (2015a). "Modelling granular soil behaviour using a physics engine." *Géotechnique Letters*, 5(4), 243–249.

Pytlos, M., Gilbert, M., and Smith, C. (2015b). "Simulation of granular soil behaviour using physics engines." *Geomechanics from Micro to Macro*, 163–168.

Rajamani, R., Mishra, B., Venugopal, R., and Datta, A. (2000). "Discrete element analysis of tumbling mills." *Powder Technology*, 109(1-3), 105–112.

Rathi, A. K. and Chakraborty, A. (2017). "Reliability-based performance optimization of tmd for vibration control of structures with uncertainty in parameters and excitation." *Structural Control and Health Monitoring*, 24(1), e1857.

Roberson, R. E. (1952). "Synthesis of a nonlinear dynamic vibration absorber." *Journal of the Franklin Institute*, 254(3), 205–220.

Robertson, D. and Bolton, M. (2001). "Discrete element simulation of crushable grains and soils." *Cambridge University Engineering Department, Cambridge*.

Robinson, W. and Greenbank, L. (1976). "An extrusion energy absorber suitable for the protection of structures during an earthquake." *Earthquake Engineering & Structural Dynamics*, 4(3), 251–259.

Romdhane, M. B., Bouhaddi, N., Trigui, M., Foltête, E., and Haddar, M. (2013). "The loss factor experimental characterisation of the non-obstructive particles damping approach." *Mechanical Systems and Signal Processing*, 38(2), 585–600.

Rozas, L., Boroschek, R. L., Tamburrino, A., and Rojas, M. (2016). "A bidirectional tuned liquid column damper for reducing the seismic response of buildings." *Structural Control and Health Monitoring*, 23(4), 621–640.

Sack, A., Heckel, M., Kollmer, J. E., Zimber, F., and Pöschel, T. (2013). "Energy dissipation in driven granular matter in the absence of gravity." *Physical Review Letters*, 111(1), 018001.

Saeki, M. (2002). "Impact damping with granular materials in a horizontally vibrating system." *Journal of Sound and Vibration*, 251(1), 153–161.

Saeki, M. (2005). "Analytical study of multi-particle damping." *Journal of Sound and Vibration*, 281(3-5), 1133–1144.

Salueña, C., Pöschel, T., and Esipov, S. E. (1999). "Dissipative properties of vibrated granular materials." *Physical Review E*, 59(4), 4422.

Sánchez, M. and Carlevaro, C. M. (2013). "Nonlinear dynamic analysis of an optimal particle damper." *Journal of Sound and Vibration*, 332(8), 2070–2080.

Sánchez, M., Rosenthal, G., and Pugnaloni, L. A. (2012). "Universal response of optimal granular damping devices." *Journal of Sound and Vibration*, 331(20), 4389–4394.

Seed, H. B., Wong, R. T., Idriss, I., and Tokimatsu, K. (1986). "Moduli and damping factors for dynamic analyses of cohesionless soils." *Journal of Geotechnical Engineering*, 112(11), 1016–1032.

SEMINAR, C. (1997). "Nehrp guidelines for the seismic rehabilitation of buildings (fema 273).

Shah, B. M., Nudell, J. J., Kao, K. R., Keer, L. M., Wang, Q. J., and Zhou, K. (2011). "Semi-active particle-based damping systems controlled by magnetic fields." *Journal of Sound and vibration*, 330(2), 182–193.

Shah, B. M., Pillet, D., Bai, X.-M., Keer, L. M., Wang, Q. J., and Snurr, R. Q. (2009). "Construction and characterization of a particle-based thrust damping system." *Journal of Sound and Vibration*, 326(3-5), 489–502.

Shamos, M. I. and Hoey, D. (1976). "Geometric intersection problems." *17th Annual Symposium on Foundations of Computer Science (sfcs 1976)*, IEEE, 208–215.

Shoemake, K. (1985). "Animating rotation with quaternion curves." *Proceedings of the 12th annual conference on Computer graphics and interactive techniques*, 245–254.

Simonian, S. S. (1995). "Particle beam damper." *Smart Structures and Materials 1995: Passive Damping*, Vol. 2445, International Society for Optics and Photonics, 149–160.

Skinner, R. I., Kelly, J. M., and Heine, A. (1974). "Hysteretic dampers for earthquake-resistant structures." *Earthquake Engineering & Structural Dynamics*, 3(3), 287–296.

Soong, T. T. and Dargush, G. F. (1997). ** Passive Energy Dissipation Systems in Structural Engineering*. Wiley.

Sun, J., Sun, H., Chow, L., and Richards, E. (1986). "Predictions of total loss factors of structures, part ii: Loss factors of sand-filled structure." *Journal of Sound and Vibration*, 104(2), 243–257.

Symans, M., Charney, F., Whittaker, A., Constantinou, M., Kircher, C., Johnson, M., and McNamara, R. (2008). "Energy dissipation systems for seismic applications: current practice and recent developments." *Journal of Structural Engineering*, 134(1), 3–21.

Thevanayagam, S., Kanagalingam, T., and Shenthan, T. (2003). "Intergrain friction, contact density, and cyclic resistance of sands." *Proc. of 2003 Pacific Conference on Earthquake Engineering, Christchurch, New Zealand*.

Thornton, C. (2000). "Numerical simulations of deviatoric shear deformation of granular media." *Géotechnique*, 50(1), 43–53.

Tijskens, E., Ramon, H., and De Baerdemaeker, J. (2003). "Discrete element modelling for process simulation in agriculture." *Journal of Sound and Vibration*, 266(3), 493–514.

Tong, L. and Wang, Y. H. (2015). "Dem simulations of shear modulus and damping ratio of sand with emphasis on the effects of particle number, particle shape, and aging." *Acta Geotechnica*, 10(1), 117–130.

Tsuji, Y., Kawaguchi, T., and Tanaka, T. (1993). "Discrete particle simulation of two-dimensional fluidized bed." *Powder Technology*, 77(1), 79–87.

Tsuji, Y., Tanaka, T., and Ishida, T. (1992). "Lagrangian numerical simulation of plug flow of cohesionless particles in a horizontal pipe." *Powder technology*, 71(3), 239–250.

Tubaldi, E. (2015). "Dynamic behavior of adjacent buildings connected by linear viscous/viscoelastic dampers." *Structural Control and Health Monitoring*, 22(8), 1086–1102.

Vakakis, A. F. (2001). "Inducing passive nonlinear energy sinks in vibrating systems." *J. Vib. Acoust.*, 123(3), 324–332.

Vemuri, B. C., Chen, L., Vu-Quoc, L., Zhang, X., and Walton, O. (1998). "Efficient and accurate collision detection for granular flow simulation." *Graphical Models and Image Processing*, 60(6), 403–422.

Verlet, L. (1967). "Computer" experiments" on classical fluids. i. thermodynamical properties of lennard-jones molecules." *Physical review*, 159(1), 98.

Vlahinić, I., Kawamoto, R., Andò, E., Viggiani, G., and Andrade, J. E. (2017). "From computed tomography to mechanics of granular materials via level set bridge." *Acta Geotechnica*, 12(1), 85–95.

Vu-Quoc, L., Zhang, X., and Walton, O. (2000). "A 3-d discrete-element method for dry granular flows of ellipsoidal particles." *Computer Methods in Applied Mechanics and Engineering*, 187(3-4), 483–528.

Vucetic, M. and Dobry, R. (1991). "Effect of soil plasticity on cyclic response." *Journal of Geotechnical Engineering*, 117(1), 89–107.

Wada, A., Saeki, E., Takeuchi, T., and Watanabe, A. (1989). "Development of unbonded brace." *Column (A Nippon Steel Publication)*, (115), 12.

Walton, O. R. and Braun, R. L. (1986). "Viscosity, granular-temperature, and stress calculations for shearing assemblies of inelastic, frictional disks." *Journal of Rheology*, 30(5), 949–980.

Wang, J. and Yan, H. (2013). "On the role of particle breakage in the shear failure behavior of granular soils by dem." *International Journal for Numerical and Analytical Methods in Geomechanics*, 37(8), 832–854.

Wang, J.-T., Gui, Y., Zhu, F., Jin, F., and Zhou, M.-X. (2016). "Real-time hybrid simulation of multi-story structures installed with tuned liquid damper." *Structural Control and Health Monitoring*, 23(7), 1015–1031.

Wang, Y.-H., Xu, D., and Tsui, K. Y. (2008). "Discrete element modeling of contact creep and aging in sand." *Journal of Geotechnical and Geoenvironmental Engineering*, 134(9), 1407–1411.

Watanabe, A., Hitomi, Y., Saeki, E., Wada, A., and Fujimoto, M. (1988). "Properties of brace encased in buckling-restraining concrete and steel tube." *Proceedings of ninth world conference on earthquake engineering*, Vol. 4, 719–724.

Wong, C., Daniel, M., and Rongong, J. (2009). "Energy dissipation prediction of particle dampers." *Journal of Sound and Vibration*, 319(1-2), 91–118.

Wong, C. and Rongong, J. (2009). "Control of particle damper nonlinearity." *AIAA Journal*, 47(4), 953–960.

Wu, C., Liao, W.-H., and Wang, M. Y. (2004). "Modeling of granular particle damping using multiphase flow theory of gas-particle." *J. Vib. Acoust.*, 126(2), 196–201.

Xiong, W., Zhang, S.-J., Jiang, L.-Z., and Li, Y.-Z. (2017). "Introduction of the convex friction system (cfs) for seismic isolation." *Structural Control and Health Monitoring*, 24(1), e1861.

Xu, Z. W., Chan, K., and Liao, W. (2004). "An empirical method for particle damping design." *Shock and Vibration*, 11(5-6), 647–664.

Yan, W., Xu, W., Wang, J., and Chen, Y. (2014). "Experimental research on the effects of a tuned particle damper on a viaduct system under seismic loads." *Journal of Bridge Engineering*, 19(3), 04013004.

Yang, M. Y. (2003). *Development of master design curves for particle impact dampers*. The Pennsylvania State University.

Yao, B., Chen, Q., Xiang, H., and Gao, X. (2014). "Experimental and theoretical investigation on dynamic properties of tuned particle damper." *International Journal of Mechanical Sciences*, 80, 122–130.

Youssef, N., Nuttall, B., Rahman, A., and Tahtakran, O. (1995). "The role of reinforced concrete in the stiffening and strengthening above base isolation for a tall historic landmark: Los angeles city hall." *Proceedings of third national concrete and masonry engineering conference, San Francisco, CA*, Vol. 2, 729–735.

Zhang, D. and Whiten, W. (1996). "The calculation of contact forces between particles using spring and damping models." *Powder technology*, 88(1), 59–64.

Zhang, K., Chen, T., Wang, X., and Fang, J. (2016). "Rheology behavior and optimal damping effect of granular particles in a non-obstructive particle damper." *Journal of Sound and Vibration*, 364, 30–43.

Zhang, P., Li, L., Patil, D., Singla, M., Li, H., Mo, Y., and Song, G. (2015). "Parametric study of pounding tuned mass damper for subsea jumpers." *Smart Materials and Structures*, 25(1), 015028.

Zhang, P., Song, G., Li, H.-N., and Lin, Y.-X. (2013). "Seismic control of power transmission tower using pounding tmd." *Journal of Engineering Mechanics*, 139(10), 1395–1406.